Accelerated Star-Forming Activity before the Peak Epoch as Revealed by Galaxies Emitting Strong Lines of Doubly Ionized Oxygen

SUZUKI TOMOKO

Doctor of Philosophy

Department of Astronomical Science
School of Physical Sciences
SOKENDAI (The Graduate University for Advanced Studies)

Doctoral thesis

Accelerated Star-Forming Activity before the Peak Epoch as Revealed by Galaxies Emitting Strong Lines of Doubly Ionized Oxygen

Department of Astronomical Science

School of Physical Sciences

The Graduate University for Advanced Studies

(SOKENDAI)

20140902

Tomoko Suzuki

Supervisor: Tadayuki Kodama

June 21, 2017

Abstract

The star-forming activity of galaxies in the Universe comes to its peak about ten billion years ago from the present-day Universe (redshift $z \sim 2$). This epoch is called the "cosmic high noon". In order to understand how the star-forming activity of galaxies is peaked towards the cosmic noon, we go further back in time to $z \sim 3$–3.6 which is 1–2 Gyr prior to $z \sim 2$. We aim to reveal what physical processes are involved in such a rapid increase of star formation rates (SFRs). So far, the ultraviolet (UV)-selected galaxies, such as Lyman Break Galaxies (LBGs), have been commonly used to probe the pre-peak epoch at $z > 3$. However, the UV-selected galaxies tend to be biased to bluer, less dusty star-forming galaxies due to strong dust extinction in the rest-frame UV regime. On the other hand, the rest-frame optical emission lines are less affected by dust extinction, and thus the optical emission line selected galaxies are more representing the star-forming galaxies including dusty ones. We focus on the [OIII]λ5007 emission line instead of Hα to trace star-forming galaxies at $z = 3$–3.6 because Hα is no longer accessible at $z > 2.6$ from the ground. Recent studies have reported that high redshift *normal* star-forming galaxies tend to show strong [OIII] emission as compared to the local counterparts. It is expected that we can use the [OIII] emission line as a good tracer of star-forming galaxies at $z > 3$.

Imaging observation with a narrow-band (NB) filter, which can capture the redshifted strong emission lines from galaxies, is a powerful method to construct a sample of star-forming galaxies in a particular redshift slice. It provides us with a clean sample of star-forming galaxies down to a certain flux and equivalent-width (EW) limits. In this *Thesis*, we use the samples of NB-selected [OIII] emission line galaxies at $z > 3$ obtained by the two systematic NB imaging surveys, namely Mahalo-Subaru and HiZELS.

In the first place, we want to confirm that the [OIII] emitters actually trace star-forming galaxies at high redshifts with little bias. For this purpose, we compare [OIII] emitters with Hα emitters at the same epoch ($z = 2.23$) selected NB filters at H and K-band, respectively. We find no significant difference on the global physical quantities between the two samples. This indicates that the [OIII] emitters are not biased towards a particular population with respect to the Hα emitters at $z = 2.23$. We have thus confirmed that the [OIII] emission line can be a useful tracer of star-forming galaxies at high redshifts.

With the [OIII] emitters at $z > 3$ in the general fields, we investigate the star-forming

activity of galaxies before the peak epoch. Stellar masses and SFRs of the [OIII] emitters show a positive correlation, which is known as the "main sequence" of star-forming galaxies. By comparing the M_*–SFR relation of the [OIII] emitters with that of the NB-selected galaxies at $z \sim 2$, we find that there is little evolution in the normalization of the main sequence between the two epochs, but that there is an offset along the constant main sequence towards the lower stellar masses with respect to the $z \sim 2$ star-forming galaxies. Based on the assumption that the galaxies evolve along the constant sequence, we can estimate the stellar mass growth of star-forming galaxies from $z = 3.2$ to 2.2. As a result, a significant mass growth of galaxies during just 1 Gyr interval is suggested. Moreover, by dividing the samples at $z = 3.2$ and 2.2 into three stellar mass bins, we find that, from $z = 3.2$ to 2.2, the fraction of massive galaxies with relatively high sSFRs and high dust extinctions increases in the highest stellar mass bin. This suggests that the dusty star formation phase becomes more common among massive galaxies since $z = 3.2$ towards the peak epoch.

We also carried out the NIR spectroscopic observations of the [OIII] emitters at $z \sim 3.24$ with Keck/MOSFIRE. Comparing the excitation/ionization states and gaseous metallicities of the [OIII] emitters at $z \sim 3.24$ with those of other samples at the same epoch, we find that the [OIII] emitters have similar ISM conditions to those of the UV continuum-selected galaxies, which are different from those of LAEs. We also compare the gaseous metallicities of the [OIII] emitters with those of the star-forming galaxies at $z \sim 2$ from the literature. Their gaseous metallicities are almost the same at a fixed stellar mass, and the mass–metallicity relation does not show a strong evolution between the two epochs.

In this *Thesis*, based on our unique NB-selected [OIII] emitters, we investigate the physical properties of star-forming galaxies at $z > 3$. Our results infer that SFRs and gaseous metallicities are increased as their stellar masses grow along the constant scaling relations since $z > 3$. We also find that the fraction of massive galaxies in a dusty star formation phase is increased since $z \sim 3.2$ to $z \sim 2.2$, indicating a transition of the mode of star formation of some massive galaxies from a secular evolution phase to a dusty star formation phase. It is suggested that the star-forming activity of galaxies is accelerated since $z > 3$ towards the peak epoch. In order to reveal the physical mechanisms behind such a rapid galaxy growth, it is required to investigate their internal structures, kinematics, and molecular gas components with high resolution observations.

Acknowledgements

I am deeply grateful to my supervisor, Prof. Tadayuki Kodama for his continuous supports, encouragements, and comments/advices throughout the three years of my Ph.D. course. Without his guidance and invaluable helps, the completion of this thesis would not have been possible. I am also grateful to team members of Mahalo-Subaru and Ganba-Subaru project, Dr. Masao Hayashi, Dr. Yusei Koyama, Dr. Ken-ichi Tadaki, Dr. Ichi Tanaka, Dr. Yosuke Minowa, Rhythm Shimakawa and Moegi Yamamoto. They told me the basics of the optical/NIR observations, data reduction and analyses, and they always give me advices, comments, and helps.

I would like to thank collaborators from HiZELS team. I have received lots of helps and supports from Dr. David Sobral. Prof. Ian Smail, Prof. Phillip Best, and A. Khostovan gave me constructive comments and suggestions to complete my second paper.

I would like to thank Prof. Lisa Kewley for hosting me at the Mt. Stromlo Observatory for three months from October to December in 2015. I also want to thank her team members and the Faulkner court residents in Mt. Stromlo who helped me a lot during my stay. I had a great experience at Mt. Stromlo, and this experience leads me to think about going abroad as a researcher in the future.

I am grateful to Prof. Yoshiki Matsuoka, who recommended me for starting my Ph.D. course in NAOJ. Without his supports, I could not have made a decision to go into a new environment. I would like to thank Prof. Tsutomu Takeuchi, who supervised me when I was in the master course in Nagoya University, for his understanding.

I would like to acknowledge the financial support from SOKENDAI. It gave me opportunities to stay Australia for three months, and to attend the international conferences many times.

I am really grateful to my friends in NAOJ, who have spent a lot of time together. Their encouragement always helps me. At last, I would like to show my heartfelt gratitude to my family for their continuous materially and mentally supports since I left my hometown.

Contents

List of figures

List of tables

1 Introduction

1.1 Star formation history in the Universe

A galaxy is an astronomical object, which consists of a large collection of stars, interstellar gas, dust, and dark matter. From the cosmological context, galaxies are the fundamental units or "building blocks" that construct the large scale structures of the Universe. When we see the individual galaxies in the local Universe, however, galaxies themselves have different physical properties one another. They have different morphologies, colors, sizes, luminosities, stellar masses, star-forming activities, and so on. Investigating how the global properties of galaxies are changing with time and also how their great diversities are developing, will eventually lead us to understand how the galaxies are formed and evolved and how the galactic Universe is build-up with cosmic time down to the present-day.

The star-forming activity in the Universe are shown to have changed with cosmic time as in Figure 1.1 from Madau & Dickinson (2014). Going back in time from the present-day, the star formation rate (SFR) density increases monotonically up to 10 billion years ago or so. It reached to the peak activity at around 10–11 billion years ago corresponding to the redshift range of $z \sim 2$–2.5. At higher redshifts, $z \gtrsim 2.5$, the SFR density turns over and starts decreasing towards the dawn of the Universe (e.g. Hopkins & Beacom, 2006; Madau & Dickinson, 2014). At $z \sim 1$–3, the activities of active galactic nuclei (AGNs) are also known to be very high (Fan et al., 2004), indicating that the growth of the black-holes is also peaked in this redshift range. Such peak epoch of galaxy/AGN formation and evolution at $z \sim 1$–3 is called the "cosmic noon". Due to the very high star-forming activity of galaxies at the peak epoch, their physical properties are expected to be largely different from those of star-forming galaxies in the local Universe.

For investigations of high redshift galaxies, observations at the near-infrared (NIR)

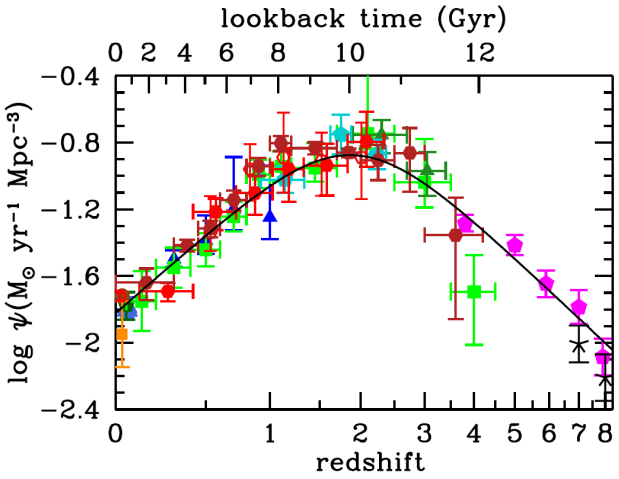

Figure 1.1: The redshift evolution of star formation rate density from Madau & Dickinson (2014). SFR densities are estimated from the rest-frame far-ultraviolet and infrared measurements. The star-forming activity in the Universe is $\sim$ 10 times higher at $z \sim$ 1–3 ($\sim$ 8–10 Gyr in lookback time) than $z = 0$.

wavelengths is very important as they can trace the light from stellar components of galaxies and can catch the important emission lines in the rest-frame optical (Section 1.4). There have been great progresses of the NIR instruments of the ground-based telescopes and *the Hubble Space Telescope* (*HST*), and studies of high redshift galaxies have advanced substantially in recent years by the NIR photometric and spectroscopic observations. Our knowledge of physical states of those galaxies has been expanded significantly by many studies (e.g. Erb et al. 2006a; van Dokkum et al. 2008; Förster Schreiber et al. 2009; Kriek et al. 2009a; Wuyts et al. 2011; Genzel et al. 2014; Steidel et al. 2016).

1.2 Stellar mass–SFR relation of star-forming galaxies : the "main sequence" of star-forming galaxies

One of the characteristic properties of star-forming galaxies at both low and high redshifts is a tight correlation between their stellar masses and SFRs (e.g. Brinchmann et al., 2004; Daddi et al., 2007; Elbaz et al., 2007; Noeske et al., 2007; Kashino et al., 2013). The positive correlation between the two quantities of star-forming galaxies is called the "main sequence" of star-forming galaxies (Figure 1.2 from Tomczak et al. (2016)).

A typical scatter of the observed sequence is ~ 0.3 dex. Such a small scatter around the main sequence suggests that most of star-forming galaxies are forming stars via secular processes rather than violent processes, such as major mergers. Cosmological simulations propose a cold gas accretion from the outside of galaxies (e.g. Kereš et al., 2005; Kereš et al. , 2009; Dekel et al., 2009). Such a molecular gas inflow from outside would lead to a normal, secular star formation within galaxies. A scatter around the main sequence would reflect a difference of the gas accretion history among the individual galaxies, although there might be some observational uncertainties. On the other hand, galaxies in a starburst phase, which are usually very bright in the far-infrared (FIR), are distributed well above the main sequence (Elbaz et al., 2007; Daddi et al., 2007; Rodighiero et al., 2011).

While the scatter around the main sequence does not strongly evolve with redshift, the zero point of the relation strongly evolves with redshift to $z \sim 2$ (e.g. Whitaker et al. 2012; Koyama et al. 2013; Tasca et al. 2015; Speagle et al. 2014; Tomczak et al. 2016). SFR increases monotonically with redshift at a given stellar mass (Figure 1.2), and SFRs of $z \sim 2$ star-forming galaxies becomes ~ 20 times higher than those of $z \sim 0$ counterparts at a fixed stellar mass. From the observations of molecular gas components with CO emission lines, it has been revealed that higher SFRs of high redshift galaxies are primarily driven by their higher molecular gas fraction (e.g. Tacconi et al., 2010, 2013; Schinnerer et al., 2016). The star-forming activities of high redshift galaxies are thus expected to be higher according to the Schmidt-Kennicutt relation (Kennicutt, 1998a). The depletion time scales (inverse of the star formation efficiencies) are likely to change more slowly with redshift.

A redshift evolution of the star-forming main sequence has now been investigated even up to $z \sim 4$ at least for massive galaxies ($\log(M_*/M_\odot) > 10.0$, e.g. Tasca et al. 2015; Speagle et al. 2014; Tomczak et al. 2016). At higher redshifts, it becomes more difficult to obtain a representative sample of star-forming galaxies down to a lower stellar mass regime. How SFRs at a fixed stellar mass (equivalent to specific star formation rates) evolve at $z > 3$ is still unclear mainly due to the incompleteness of samples of star-forming galaxies and the selection bias that it causes.

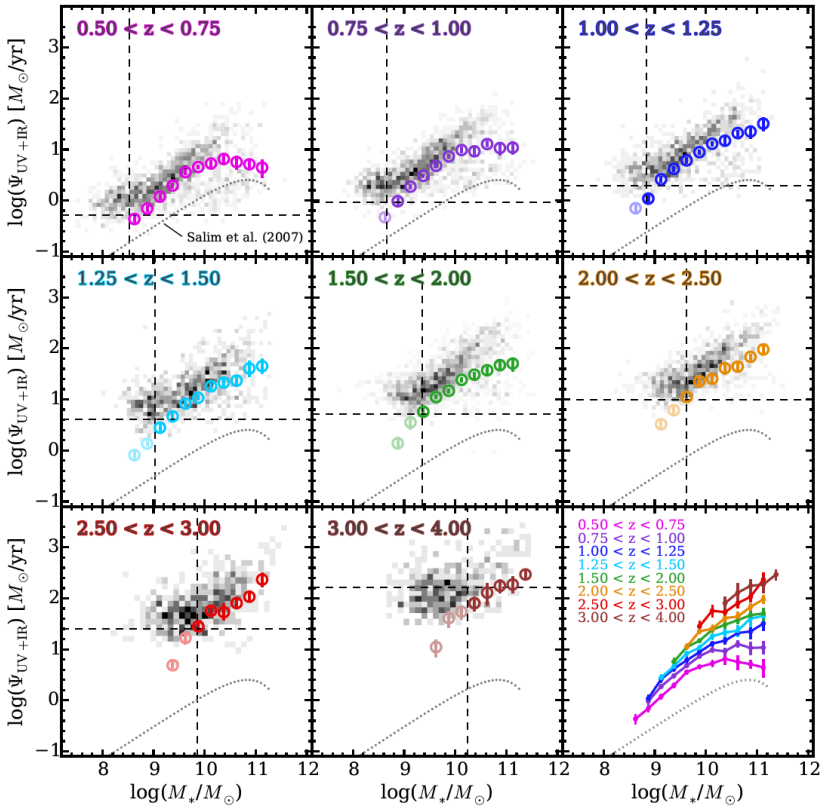

Figure 1.2: Stellar mass versus SFR diagrams for each redshift bin from $z = 0.5$ to $z = 4.0$ from Tomczak et al. (2016). In each redshift bin, a correlation between stellar masses and SFRs (the star-forming main sequence) is observed. Moreover, the bottom right panel shows a redshift evolution of the star-forming main sequence. Samples of star-forming galaxies are selected from the catalogs obtained by the ZFOURGE survey (Straatman et al., 2016). SFRs are estimated from a combination of the UV and IR luminosities.

1.3 Galaxy size and its dependence on stellar mass

The structural properties of galaxies, such as sizes and morphology, and the redshift evolution of such physical quantities are expected to reflect the mass assembly history of galaxies.

Galaxy sizes correlate with their stellar masses in the sense that massive galaxies have larger sizes than less massive galaxies at a particular redshift (left panel of Figure 1.3). It has been found that different galaxy populations, namely late-type (star-forming) galaxies and early-type (passive) galaxies, follow different mass–size relations. The sizes of early-type galaxies more strongly depend on their stellar masses as compared to those

of late-type galaxies (e.g. Shen et al., 2003; van der Wel et al., 2014; Allen et al., 2016a).

The mass–size relation also changes with redshift as shown in Figure 1.3 from van der Wel et al. (2014). At a given stellar mass, galaxies are more compact at higher redshifts for both galaxy populations. Moreover, the average size evolution since $z = 3$ of early-type galaxies is more rapid than that of late-type galaxies. Such different size growth histories between the two populations suggests that some different physical mechanisms are involved in the mass assembly processes of early-type and late-type galaxies. The slow evolution of late-type galaxies may suggest a secular evolution of their sizes via internal star formation.

The redshift evolution of the sizes of star-forming galaxies has been investigated up to $z \sim 7$ or even higher redshifts using the LBGs or mass-selected samples (e.g. Mosleh et al., 2012; Shibuya et al., 2015; Allen et al., 2016b). These results all suggest that the sizes decreases with redshifts, however, the slopes of the size evolution are slightly different among the different studies probably due to the different methods of size measurements and different sample selections. We here note again that, in particular at $z > 3$, it is critical to obtain a representative sample of star-forming galaxies in a narrow redshift range.

At higher redshifts, it is more difficult to measure the accurate sizes of galaxies because their sizes become smaller with redshifts and the wavelength range that can neatly trace the underlying stellar components in mass becomes redder and redder with redshift. Therefore we need to obtain higher angular resolution images of high redshift galaxies at the NIR wavebands (or even longer wavelengths if possible). The Wide Field Camera 3 (WFC3) on the *HST* is a powerful instrument for this purpose. The WFC3/H-band can capture the rest-frame optical light from high redshift galaxies at least up to $z \sim 3$ or so.

On the mass–size relation especially for high redshift galaxies, massive and compact early-type galaxies are often found. Such compact quiescent galaxies are one of the most characteristic objects at high redshift Universe, and they are called "red nuggets" (e.g. Daddi et al. 2005; Damjanov et al. 2009; van Dokkum et al. 2010). Recently, their likely progenitors, namely, compact and massive star-forming galaxies, are also commonly observed at high redshifts (e.g. Barro et al. 2013). The compact star-forming galaxies are though to be formed by gas-rich processes such as mergers or disk instabilities that invoke starbursts in the central compact regions. They would then become compact, quiescent

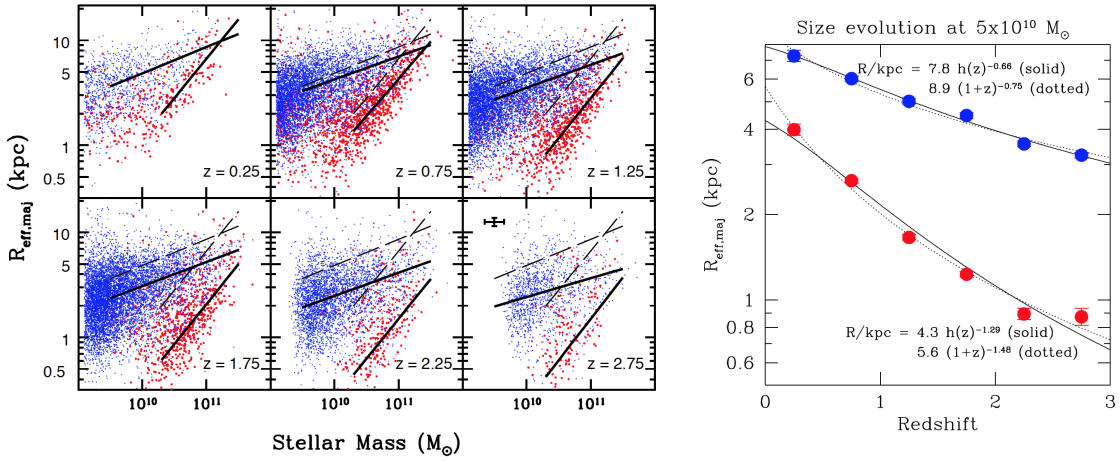

Figure 1.3: Two figures related to the galaxy size evolution from van der Wel et al. (2014). **(Left)** : Mass–size relation of the late-type (blue dots) and early-type (red dots) galaxies in each redshift bin. The solid lines represent the model fits to the early-type and late-type galaxies of each redshift bin, and the dashed lines represent the model fits to the galaxies at $0 < z < 0.5$. The relations between stellar masses and sizes are totally different between the two galaxy populations in any redshift bins. **(Right)** : The redshift evolution of the size at the fixed stellar mass of $5 \times 10^{10} M_{\odot}$. Blue and red dots show late-type and early-type galaxies, respectively. The size evolution of the late-type galaxies since $z = 3$ is relatively slow as compared to that of the early-type galaxies.

galaxies when their star formation is quenched (Barro et al., 2013). The cosmic noon and the epoch *before* the cosmic noon are critical for us to study and reveal the evolutionary path from the compact star-forming galaxies to the compact quiescent galaxies.

1.4 Interstellar medium conditions of star-forming galaxies

1.4.1 Emission lines from the ionized gas

In a star-forming region within a galaxy, hot, young, and massive stars (OB-type stars) are embedded. By strong ionizing fluxes from the OB stars, the hydrogen atoms and metals are ionized and a HII region is formed around massive stars. Various emission lines are observed in the spectra emitted from HII regions. There are emission lines from various atoms in different ionization states, and their relative strengths depend on the physical

conditions of the surrounding region, such as metallicities, electron densities, hardness of ionizing photons, and so on (e.g. Kewley & Dopita, 2002; Kewley et al., 2013; Steidel et al., 2016).

The strength of emission lines from ionized gas is basically correlated with SFR, and therefore the emission lines (not all of the emission lines) from HII regions are used as indicators of star-forming galaxies (e.g. Bunker et al. 1995; Malkan, Teplitz & McLean 1996; Sobral et al. 2013; Hagen et al. 2015). Among the various emission lines across a wide wavelength range, the emission lines in the rest-frame optical have been commonly used to trace star-forming galaxies and estimate their physical quantities. For example, the Hα emission line at 6563 Å is one of the best indicators of star-forming galaxies because it is strong and less affected to dust extinction than the UV light, and the relation between SFRs and Hα luminosities has been well calibrated in the local Universe (e.g. Hopkins et al. 2003). Moreover, the ratio of Hα and Hβ (4861 Å) or Hβ and Hγ (4340 Å) is frequently used to determine the amount of dust extinction (Osterbrock & Ferland, 2006).

Oxygen is a relatively common metal in the Universe. The forbidden lines of doubly ionized oxygen ([OIII]) and singly ionized oxygen ([OII]) are observed in the spectra of HII regions. In the rest-frame optical spectra, there are strong emission lines of oxygen, namely, [OIII]$\lambda\lambda$5007,4959 and [OII]λ3726,3729. These emission lines are collisional excitation lines, and therefore, the strengths of [OIII] and [OII] largely depends on the conditions of ISM in contrast to the Balmer lines, such as Hα and Hβ.

For example, when the ionization parameters, the ratio of the number density of ionizing photos to that of hydrogen atoms (see Section 1.4.2 for the definition), are high, the ionization of O^+ to O^{++} is facilitated. As a result, the [OIII] emission becomes stronger with respect to the [OII] emission. Lower gaseous metallicities make gaseous temperature high due to the lack of gas coolants. High gaseous temperatures enhance the collisional excitation lines with respect to a recombination line of hydrogen. Additionally, when the ionizing spectra become harder, the enhancement of the collisional excitation is seen because the kinematic energy of ionized spectra becomes larger (Kewley & Dopita, 2002; Strom et al., 2016).

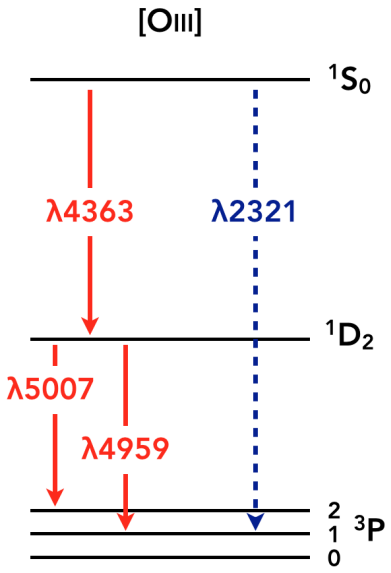

Figure 1.4: Schematic view of the energy–level diagram for lowest terms of [OIII]. The emission lines in the optical wavelength are represented as the solid lines. Those in the UV wavelength are represented as the dashed lines. In our study, we focus on the [OIII]λ5007 emission line.

1.4.2 Different physical conditions of high redshift star-forming galaxies

The ISM conditions of galaxies are described by gaseous metallicities, ionization parameters, electron densities, ionizing spectra, and so on (Kewley et al., 2013; Masters et al., 2014; Nakajima & Ouchi, 2014; Onodera et al., 2016). An (effective mean) ionization parameter q is defined as follows:

$$q \equiv \frac{Q_{\mathrm{H}^0}}{4\pi R_s^2 n}, \tag{1.1}$$

where Q_{H^0} is the flux of the ionizing photons produced by the existing stars above the Lyman limit, R_s is the Strömgren radius, and n is the local number density of hydrogen atoms (Kewley & Dopita, 2002). Simply stated, the ionization parameter is the ratio of a density of ionizing photons to that of hydrogen atoms at the surface of a HII region.

For example, gaseous metallicities is determined by the contributions from star formation and gas inflow/outflow processes. Ionization parameters are determined by the compactness of star-forming regions and/or the strength of the ionizing source. Spectrum shapes (hardness) of ionizing photons depend on the stellar populations in a star-forming

region. The ISM conditions of galaxies are thus closely related to their star-forming activity, and it is expected that at higher redshifts, where galaxies are forming stars more actively, galaxies are expected to have different ISM conditions from local star-forming galaxies.

Recently, some large NIR spectroscopic observations have been carried out, such as KBSS-MOSFIRE (Steidel et al., 2014) and MOSDEF (Kriek et al., 2015). From NIR spectra of high redshift star-forming galaxies, the extreme ISM conditions of star-forming galaxies are suggested (e.g. Masters et al. 2014; Steidel et al. 2014; Shapley et al. 2015; Holden et al. 2016). One is an offset on the Baldwin-Phillips-Terlevich (BPT) diagram (Baldwin, Phillips & Terlevich, 1981). High redshift galaxies show a high [OIII]/Hβ ratio at a fixed [NII]/Hα ratio with respect to the sequence of local star-forming galaxies (e.g. Masters et al., 2014; Steidel et al., 2014; Shapley et al., 2015; Kashino et al., 2016). Another is the higher [OIII]/Hβ ratios of high redshift galaxies than the local galaxies at a fixed stellar mass as shown in Figure 1.5 (e.g. Shimakawa et al., 2015; Holden et al., 2016; Strom et al., 2016).

Figure 1.6 shows the R_{23}-index versus [OIII]/[OII] ratio diagram. R_{23}-index represents the ratio of $([\mathrm{OIII}]\lambda\lambda5007, 4959 + [\mathrm{OII}]\lambda3727)/\mathrm{H}\beta$. Although the R_{23}-index and [OIII]/[OII] ratio depend on both metallicity and ionization parameter, R_{23}-index is more sensitive to the metallicity, while the [OIII]/[OII] ratio is more sensitive to the ionization parameter (Kewley & Dopita, 2002). Using the two line ratios, Nakajima & Ouchi (2014) discussed the metallicity and ionization parameter simultaneously for high redshift LBGs and LAEs (Figure 1.6). On the R_{23}-index versus [OIII]/[OII] ratio diagram, high redshift star-forming galaxies are distributed on the region of higher R_{23}-index and higher [OIII]/[OII] ratio (e.g. Nakajima & Ouchi 2014; Shapley et al. 2015; Onodera et al. 2016; Strom et al. 2016), where metal-poor galaxies at $z = 0$ are distributed. High redshift galaxies tend to show higher ionization parameters and lower gaseous metallicities systematically. Higher R_{23}-indices of high redshift star-forming galaxies are also explained by the harder ionizing radiation fields (Steidel et al., 2016; Strom et al., 2016).

We note that there might be a kind of selection effect to the results that the high redshift star-forming galaxies have extreme ISM conditions. Juneau et al. (2014) showed that the local galaxies that are selected with a certain detection limit of emission line at high redshifts tend to show higher [OIII]/Hβ ratios on the BPT or Mass–Excitation

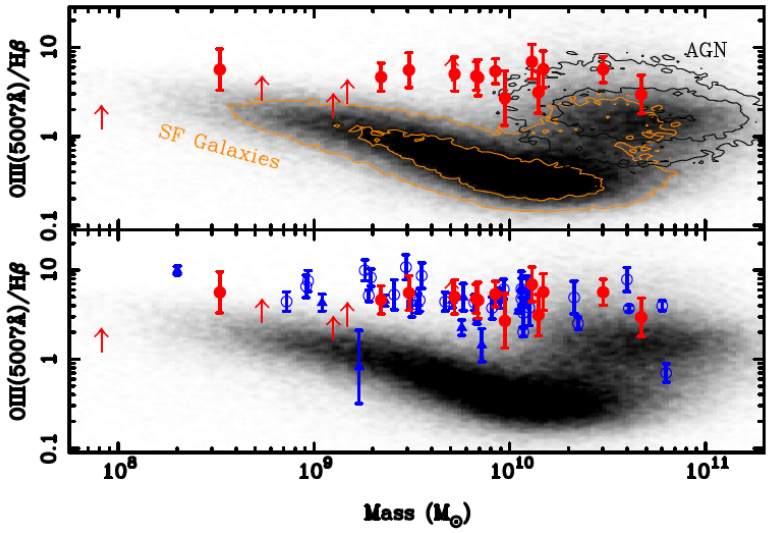

Figure 1.5: Relation between stellar mass and [OIII]/Hβ ratio (Mass–Excitation diagram, Juneau et al. 2011) of $z > 3$ Lyman Break Galaxies (LBGs) from Holden et al. (2016). Filled circles show their LBG sample, and the filled triangles and open circles represent the LBG samples at $z > 3$ from the literature. The local galaxies from SDSS are shown in the grayscale. In the top panel, the contours show the two branches of the star-forming galaxies and AGNs.

diagram as observed for the star-forming galaxies at $z \sim 1.5$. If fainter emission line galaxies at high redshifts below the limits were included, the ISM conditions of star-forming galaxies would not strongly evolve with redshift (e.g. Juneau et al., 2014; Dickey et al., 2016).

1.4.3 Mass–metallicity relation across cosmic time

As mentioned above, a gaseous metallicity [1] is an important physical quantity of galaxies. There are some calibration methods to measure the gaseous metallicity of galaxies.

One is called a "direct electron-temperature (T_e) method" (e.g. Izotov et al. 2006; Andrew & Martini 2013; Kojima et al. 2016; Sanders et al. 2016b). The ratios of the strong line and auroral line of the same ions, for example, [OIII]$\lambda\lambda$5007,4959 and [OIII]λ4363 (Figure 1.4), are sensitive to the electron temperature of the ionized gas. Since metals in gas phase are major coolants of HII regions, electron temperatures correlate with gaseous metallicities (abundance of a particular ion), and therefore, we can measure gaseous metal-

[1] Throughout this *Thesis*, a "gaseous metallicity" usually means a gaseous oxygen abundance, 12+log(O/H).

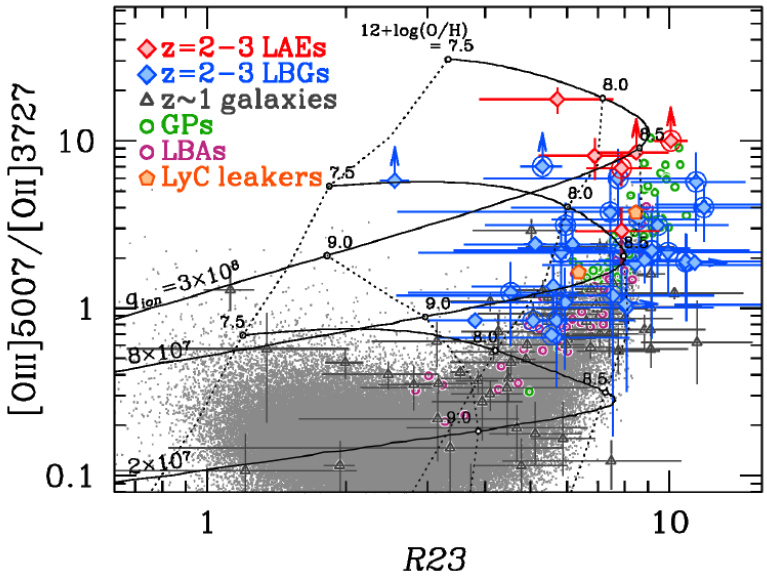

Figure 1.6: The relation between R_{23}-index and [OIII]/[OII] ratio from Nakajima & Ouchi (2014). The LBGs and LAEs at $z = 2$–3 are represented with the blue symbols and the red symbols, respectively. The gray scale represents the local SDSS galaxies.

licities by obtaining electron temperatures and electron densities. However, since the auroral lines are very weak, it is difficult to detect the auroral lines for individual galaxies especially for metal-rich galaxies and at high redshifts.

To date, various metallicity calibration methods using relatively strong emission lines, which are easier to observe, are proposed by many studies. Some studies empirically calibrate relations between the line ratios and metallicities, which are estimated from the direct T_e method (e.g. Pettini & Pagel 2004; Maiolino et al. 2008; Jones et al. 2015; Curti et al. 2016). These relations are calibrated with the star-forming galaxies at $z = 0$. Some studies calibrate relations between the line ratios and metallicities based on the photoionization models of HII regions (e.g. Kewley & Dopita, 2002; Kobulnicky & Kewley, 2004; Dopita et al., 2016). Kewley & Ellison (2008) showed that gaseous metallicities which are estimated with different calibrations tend to show systematic offsets one another. Therefore, we have to keep it mind when we compare the gaseous metallicities estimated with different methods.

The correlation between stellar masses and gaseous metallicities of star-forming galaxies is called the mass–metallicity relation. Mass–metallicity relations have been investigated from $z = 0$ to $z > 3$ (e.g. Tremonti et al. 2004; Erb et al. 2006a; Maiolino et al.

2008; Zahid et al. 2014; Steidel et al. 2014). Gaseous metallicities of star-forming galaxies at a fixed stellar mass decrease with redshift, which is more prominent for less massive galaxies (Zahid et al., 2014). However, due to the discrepancy between metallicity calibration methods and the low signal-to-noise ratios of spectra of high redshift galaxies, the redshift evolution of the mass–metallicity relation is still under debate especially at higher redshifts ($z > 2$).

The scatter of the mass–metallicity relation is large in contrast to that of the stellar mass–SFR relation. Mannucci et al. (2010) showed that there is a correlation between the metallicities and SFRs. Star-forming galaxies with lower SFRs tend to have lower metallicities at a given mass, and the local SDSS galaxies are distributed on a surface in the three-dimensional space of stellar mass, SFR, and metallicity. This is called the fundamental metallicity relation (FMR). In Mannucci et al. (2010), they introduced μ_α, which is defied as $\mu_\alpha = \log(\mathrm{M}_*) - \alpha \times \log(\mathrm{SFR})$. The α value is chosen to be 0.32 so that the scatter around the projected FMR on the 12+log(O/H) versus μ_α plane can be minimized. Not only the local galaxies, but also the star-forming galaxies up to $z \sim 2.5$ are claimed to follow the same FMR, while there are some other studies which show weak correlations between gaseous metallicities and SFRs at $z \sim 2$ (e.g. Wuyts et al., 2014; Cullen et al., 2014; Strom et al., 2016).

1.5 Going back in time before the peak epoch with the [OIII] emission line

In order to understand how and why the star-forming activity increases towards the peak epoch at $z \sim 1$–3, it is necessary to go further back in time before the peak epoch, i.e. $z > 3$. The epoch of $z = 3$–3.6 corresponds to just 1–2 Gyr before the highest peak.

To date, samples of galaxies at $z > 3$ are mainly constructed by tracing the UV light from hot, young, and massive stars in star-forming regions. Since the UV light is strongly affected by the dust extinction, the UV-selected galaxies tend to be biased towards younger and bluer star-forming galaxies (Cowie et al., 2011). In terms of the insensitivity to the dust extinction, the rest-frame optical emission lines are useful as mentioned in Section 1.4.1. Emission lines at shorter wavelengths than Hα are accessible at $z > 3$ from the ground.

In this *Thesis*, we will focus on the [OIII]λ5007 emission line instead of Hα to trace the star-forming galaxies at $z \sim 3$–3.6. As mentioned in Section 1.4.2, it is has been revealed that the high redshift star-forming galaxies tend to show higher [OIII]/Hβ ratios compared to the local counterparts (Steidel et al., 2014; Shapley et al., 2015; Holden et al., 2016). It is easier to observe [OIII] emission lines from galaxies even at $z > 3$ than Hβ or [OII], for example. We expect that [OIII]λ5007 emission line can be a useful tracer of star-forming galaxies at $z > 3$.

On the other hand, there are possible biases emerging by using [OIII] as an indicator of star-forming galaxies. One is related to the contribution of AGNs. The [OIII] emission line originates from the gas ionized not only by hot, young massive stars in the star-forming regions but also by central AGNs (Zakamska et al., 2004). At least in the local Universe, strong [OIII] emission is often regarded as an evidence for the presence of AGN. Galaxies traced by their strong [OIII] emission are likely to be more contributed by AGNs compared to the galaxies traced by other emission lines.

Because of the slightly shorter wavelength of the [OIII] line (5007Å) with respect to the Hα line (6563Å), the samples of [OIII]-selected galaxies may be inherently biased against dusty systems in comparison to the Hα-selected samples, although the dust extinction at the wavelength of the [OIII] emission line is only ~ 1.3 times larger than that at the wavelength of the Hα emission line based on the extinction curve of Calzetti et al. (2000). Moreover, the strength of [OIII] emission line is sensitive to the physical conditions of the ISM as mentioned in Section 1.4.1. Galaxies traced by [OIII] emission might be biased towards galaxies with lower stellar masses given the well-known mass–metallicity relation of star-forming galaxies.

Therefore, before we carry out a systematic survey of star-forming galaxies at $z \sim$ 3–3.6 with [OIII] emission lines, it is necessary for us to confirm the usefulness of the [OIII] emission line as an indicator of star-forming galaxies at high redshifts.

1.6 This *Thesis*

In this *Thesis*, we focus on the galaxy formation before the peak epoch, and construct the samples of star-forming galaxies at $z > 3$ by capturing their [OIII] emission lines by narrow-band (NB) filters. We here use the NB imaging data obtained by the two NB

surveys, namely Mahalo-Subaru and HiZELS. In Chapter 2, we introduce the selection method of star-forming galaxies from the NB imaging data.

In Chapter 3, in the first place, we investigate the usefulness of the [OIII] emission line as a tracer of star-forming galaxies at high redshifts. We compare the physical quantities of the [OIII]-selected galaxies at $z = 2.23$ with those of the Hα-selected galaxies at the same redshift in the COSMOS field obtained by HiZELS.

In Chapter 4, we investigate the star-forming activity of the [OIII] emitters at $z > 3$. We use the two samples of [OIII] emitters in the general fields at $z = 3.18,\ 3.63$ and $z = 3.24$ obtained by Mahalo-Subaru and HiZELS, respectively. We estimate SFRs from the UV luminosities and investigate the relation between the stellar mass and SFR of the [OIII] emitters at $z > 3$. Then, we compare the stellar mass–SFR relation at $z > 3$ with that of the NB-selected galaxies at $z \sim 2$. For the [OIII] emitters obtained by Mahalo-Subaru, we measure the sizes of galaxies using their H-band images taken with the *HST*/WFC3. We investigate the relations between the stellar mass and size of the star-forming galaxies at $z > 3$. For the [OIII] emitters obtained in HiZELS, taking an advantage of the large number of available sources, we divide the samples at $z = 3.24$ and $z = 2.23$ into three stellar mass bins. We compare the specific SFR and dust extinction of the star-forming galaxies with comparable stellar masses between the two epochs.

In order to investigate more detailed physical conditions, we carry out a NIR spectroscopic observation for the [OIII] emitters at $z = 3.24$ with Keck/MOSFIRE. In Chapter 5, we show the observational results of the NIR spectroscopy and discuss the ISM conditions of the [OIII] emitters by comparing them with other galaxy populations at the same epoch. We measure gaseous metallicities of the [OIII] emitters using three calibration methods, and investigate the relation between their stellar masses and metallicities, and the correlation between the metallicities and SFRs.

In Chapter 6, we discuss the galaxy growth from $z > 3$ towards the peak epoch at $z \sim 2$ based on our results obtained in Chapter 4. Moreover, we discuss the redshift evolution of the ISM conditions of star-forming galaxies. We compare our [OIII] emitters at $z \sim 3.24$ with the sample of star-forming galaxies at $z \sim 2.2$ in the literature on the R_{23}-index versus [OIII]/[OII] ratio diagram and on the mass–metallicity diagram.

In Chapter 7, we summarize our study, and in Chapter 8, we address future observational plans using the [OIII] emitters at $z \sim 3$–3.6.

Throughout this *Thesis* we assume the cosmological parameters of $\Omega_{\rm m} = 0.3$, $\Omega_\Lambda = 0.7$, and $H_0 = 70$ kms^{-1}Mpc^{-1}, unless otherwise noted. All the magnitudes are given in AB system (Oke & Gunn, 1983).

2 Selection methods of star-forming galaxies based on NB imaging

2.1 Imaging observation with NB filters and its advantages

As mentioned in Section 1.4.1, the ionized regions by hot, young, and massive stars emit various emission lines, such as Hα, [OIII], Hβ, [OII], Paα, and so on. We can catch the redshifted emission lines by imaging observations with a NB filter. This is one of the most powerful methods to construct a sample of star-forming galaxies at a particular redshift slice (e.g. Bunker et al. 1995; Malkan, Teplitz & McLean 1996; Moorwood et al. 2000; Geach et al. 2008). By taking the images not only with a NB filter, but also with a broad-band (BB) filter corresponding to the wavelength of the NB filter, we can pick up the NB excess sources, which are brighter in NB than BB. We can also estimate fluxes of an emission line for the NB emitters from the NB and BB data as explained in Section 2.2.

NB excess sources consist of different emission line galaxies at different redshifts. Once we identify redshifts of NB emitters by using their colors or photometric redshifts (see Section 2.2 for more details), we can obtain a sample of emission line galaxies at a particular redshift range. A redshift range of galaxies picked up by a NB imaging is much narrower than that of galaxies obtained by BB color selections, such as the BzK selection (e.g. Daddi et al. 2005) or the Lyman break selection (e.g. Steidel & Hamilton 1997). Moreover, since the NB selection is based on the emission line fluxes and EWs, we can obtain a nearly SFR-limited sample of star-forming galaxies within a narrow redshift range. This is also one of the advantages of the NB imaging observation.

We also note that the high efficiency of follow-up observations for the NB-selected galaxies. As mentioned above, since the redshifts and emission line fluxes are already

known from the NB imaging observations, the feasibility of observations, such as line diagnostic spectroscopy and integral field unit (IFU) spectroscopy, becomes very high.

The star-forming galaxies used in this *Thesis* is selected based on the NB technique. In the following, we briefly introduce an example to show how the emission line galaxies are selected from the obtained NB data, and how we can estimate the line fluxes of the emitters.

2.2 Selection methods of NB emitters and flux measurement

The observational data introduced in this Section as an example are obtained by the NB imaging observations with the Multi Object InfraRed Camera and Spectrograph (MOIRCS; Suzuki et al. 2008) on the Subaru telescope. The target field is the Subaru/*XMM-Newton* Deep survey Field (SXDF; Furusawa et al. 2008). The two NB filters, namely NB2095 ($\lambda_c = 2.093$ μm, FWHM = 0.026 μm) and NB2315 ($\lambda_c = 2.317$ μm, FWHM = 0.026 μm), are used (Tadaki et al., 2013). Figure 2.1 shows the transmission curves of the two NB filters. We introduce the case of NB2095 below, and the details of the observations and the data reduction are described in Tadaki et al. (2013).

First of all, we extract sources from the NB images taken with MOIRCS and the BB (H and K bands) images taken with the Wide Field Camera (WFCAM; Casali et al. 2007) on the United Kingdom Infrared Telescope (UKIRT), using the public software `SExtractor` (Bertin & Arnouts, 1996). The pixel scales and PSF sizes of the BB images are matched to those of the NB images. We perform aperture photometries on the NB and BB images with a $1''.6$ diameter aperture. Source extraction and photometries are carried out with the double image mode of `SExtractor`. Those aperture photometry data are used to select line emitters based on the color–magnitude diagram as shown in Figure 2.2.

The sources which are much brighter in NB as compared to BB are selected as the line emitters. Since the effective wavelengths of the NB filter and the K-band are slightly different (Figure 2.1), we estimate the BB fluxes at the exact effective wavelengths of the NB2095 filter by interpolating fluxes between H and K bands as follows (Tadaki et al., 2013):

$$HK(\lambda = 2.09\ \mu\mathrm{m}) = 0.8\ K + 0.2\ H - 0.015. \tag{2.1}$$

We select NB excess sources using $HK-$NB2095 color versus NB 2095 magnitude diagram (Figure 2.2). Here we set the three selection criteria. The first criterion is that the NB magnitude is brighter than the 5σ limiting magnitude ($m_{\mathrm{NB},5\sigma} = 23.6$mag; the vertical dashed line in Figure 2.2).

The second criterion is based on the selection using a parameter Σ, which determines the significance of an NB excess relative to a 1σ photometric error (Bunker et al., 1995). The relation between Σ and the color of $m_{\mathrm{BB}} - m_{\mathrm{NB}}$ is obtained from

$$m_{\mathrm{BB}} - m_{\mathrm{NB}} = -2.5\ \log_{10}\left[1 - \frac{\Sigma\sqrt{\sigma_{\mathrm{BB}}^2 + \sigma_{\mathrm{NB}}^2}}{f_{\mathrm{NB}}}\right], \tag{2.2}$$

where f_{NB} is a NB flux density, σ_{BB}^2 and σ_{NB}^2 are the sky noises in the BB and NB images measured within an aperture, respectively (Tadaki et al., 2013). We set the criterion of $\Sigma = 3$ to sample secure emitters, and it is represented as the solid curve in Figure 2.2. This selection criterion corresponds to the limit of the emission line flux. For this observation with NB2095, the line flux limit at the 3σ significance level is $F_{\mathrm{line}} = 1.5 \times 10^{-17}$erg s^{-1}cm^{-2}.

The third one is $HK - \mathrm{NB} > 0.4$ mag, which determines the NB magnitude excess with respect to the HK magnitude (the horizontal solid line in Figure 2.2). This selection criterion corresponds to the limit of the EW of $\mathrm{EW_{rest}} > 30$ Å for the [OIII] emitters at z=3.18.

The NB and BB flux densities are defined as

$$f_{\mathrm{NB}} = f_c + F_{\mathrm{line}}/\Delta_{\mathrm{NB}}, \tag{2.3}$$

$$f_{\mathrm{BB}} = f_c + F_{\mathrm{line}}/\Delta_{\mathrm{BB}}, \tag{2.4}$$

where f_c is a continuum flux density, F_{line} is a line flux intensity, and Δ_{NB} and Δ_{BB} are FWHMs of the NB and BB filters (Tadaki et al., 2013). The continuum flux density, the line flux intensity, and the EW in the rest-frame are given by the following equations, respectively;

$$f_c = \frac{f_{\rm BB} - f_{\rm NB}(\Delta_{\rm NB}/\Delta_{\rm BB})}{1 - \Delta_{\rm NB}/\Delta_{\rm BB}}, \tag{2.5}$$

$$F_{\rm line} = \Delta_{\rm NB} \frac{f_{\rm NB} - f_{\rm BB}}{1 - \Delta_{\rm NB}/\Delta_{\rm BB}}, \tag{2.6}$$

$$\mathrm{EW}_{\rm rest} = \frac{F_{\rm line}}{f_c}(1+z)^{-1}. \tag{2.7}$$

The NB excess sources selected by the color–magnitude diagram consist of different emission line galaxies at different redshifts. In the case of NB2095, Paα emitters at $z = 0.12$, Hα emitters at $z = 2.19$, [OIII] emitters at $z = 3.18$, and [OII] emitters at z=4.61 are possibly included in the emitter sample. When separating their redshifts, the multi-wavelength photometry is required. The color–color diagrams or photometric redshifts are often used to identify the redshifts of the NB emitters (e.g. Hayashi et al. 2012; Sobral et al. 2013). When we try to separate the redshifts of galaxies with the color–color diagram, for example, the conspicuous spectral features such as the Balmer and/or 4000Å breaks or the Lyman break can be used. Since the break feature is redshifted to a different wavelength in the observed frame according to the redshifts of galaxies, by choosing an appropriate combination of passbands that can neatly straddle the spectral break feature, we are able to disentangle the various possible solutions for different line emitters at different redshifts.

We do not require a high accuracy for these selection methods because the possible emitters have largely different redshift ranges with each other.

2.3 Mahalo-Subaru

"Mahalo-Subaru" (MApping HAlpha and Lines of Oxygen with Subaru; Kodama et al. 2013) is a systematic NB imaging survey with the Subaru Prime Focus Camera (Suprime-Cam; Miyazaki et al. 2002) and MOIRCS on the Subaru Telescope. This project aims to reveal the emergence of the environmental dependence of galaxy properties in the history of the Universe by targeting high density regions, such as galaxy clusters/proto-clusters, as well as the lower-density blank fields, and constructing a coherent sample of NB-selected star-forming galaxies across various environments and cosmic time (Figure 2.3).

So far, this project focuses on star-forming galaxies mainly at $z \sim 1$–2.5. For example, in Hayashi et al. (2012) and Koyama et al. (2013), they targeted Hα emitters residing

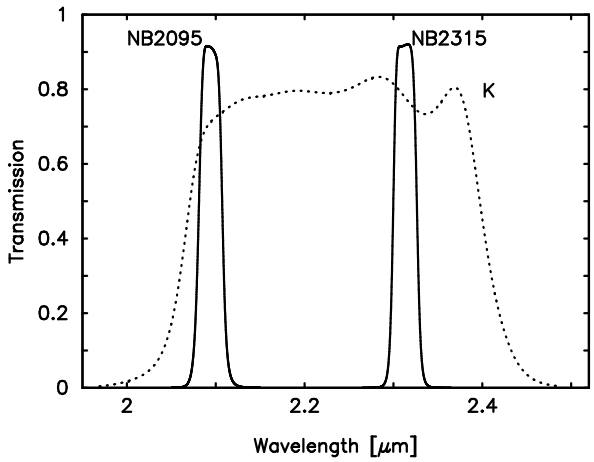

Figure 2.1: Transmission curves of the K-band filter on UKIRT/WFCAM (dotted line), and the two NB filters on MOIRCS, namely NB2095 and NB2315, used in the NB imaging observation at the SXDF (solid lines). With the NB filters, we capture the emission lines from the distant galaxies. K-band data are used to estimate the stellar continuum (Section 2.2).

in proto-cluter environments at $z \sim 2.5$ and 2.2, respectively. Their results suggest the presence of the active star-forming galaxies in rich environments as contrasted to galaxy clusters at lower redshifts. Tadaki et al. (2013, 2014) carried out $z \sim 2$ Hα emitter survey with MOIRCS in the SXDF. They constructed a sample of star-forming galaxies at $z =$ 2.2 and 2.4 using the two NB filters, namely NB2095 and NB2315. The *HST* images are available for all the Hα emitters. They found the clumpy structures of the Hα emitters at $z \sim 2$, and that the redder star-forming clumps tend to be near the center of galaxies, indicating the bulge formation accompanied by dusty star formation in the central region of normal star-forming galaxies.

Now, we are expanding our survey to more distant Universe, i.e. $z > 3$, in order to investigate the galaxy formation and its environmental dependence before the peak epoch. So far, as a field sample, we have constructed a sample of [OIII] emitters at $z = 3.18$ and 3.62 in the SXDF. These [OIII] emitters are obtained from the same observational data shown in Tadaki et al. (2013, 2014). We will explain the details of this sample in Chapter 4.

Also, we have already carried out the [OIII] imaging observation in a proto-cluster environment at $z = 3.13$, namely MRC0316-257 (Venemans et al., 2007), with MOIRCS

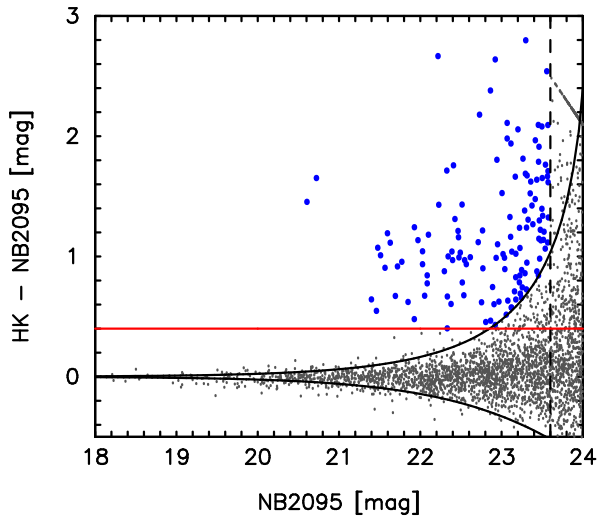

Figure 2.2: Color–magnitude diagram for NB2095. Gray dots represent all the sources detected in the NB images, and blue filled circles are the sources selected as the NB emitters with our selection criteria. The solid curve correspond to $\pm$ 3σ photometric errors, and the horizontal red line corresponds to $HK - \mathrm{NB} = 0.4$ [mag]. The vertical dashed line corresponds to the 5σ limiting magnitude of the NB2095 data.

and NB2071 filter. [OIII] imaging observations in proto-cluster fields at $z > 3$ are one of the future prospects of this *Thesis*. We will touch on this again in Chapter 8.

2.4 HiZELS

HiZELS, the High-Z Emission Line Survey (Best et al., 2013; Sobral et al., 2013), is a panoramic NB imaging survey using NB filters in the J, H, and K bands of WFCAM on UKIRT, and the NB921 filter of the Suprime-Cam on the Subaru telescope (Figure 2.4). Their main survey fields are the general fields, such as the Cosmological Evolution Survey (COSMOS) field (Scoville et al., 2007) and the UKIDSS Ultra Deep Survey (UDS) field (Lawrence et al., 2007).

HiZELS covers a wide field-of-view, for example, $\sim$ 1.6 deg^2 in the COSMOS field. With the large number of emitters ([OII], [OIII], and Hα emitters) at various redshifts, the clustering properties of emitters, the redshift evolution of the emission line and luminosity function, stellar mass function, and SFR function has been investigated (e.g. Geach et al.

environ-ment	target	z	line	λ (μm)	camera	NB-filter	conti-nuum	status (as of Apr 2015)
Low-z clusters	CL0024+1652	0.395	Hα	0.916	Suprime-Cam	NB912	z'	Kodama+'04
	CL0939+4713	0.407	Hα	0.923	Suprime-Cam	NB921	z'	Koyama+'11
	CL0016+1609	0.541	Hα	1.011	Suprime-Cam	NB1006	z'	not yet
	RXJ1716.4+6708	0.813	Hα	1.190	MOIRCS	NB1190	J	Koyama+'10
			[OII]	0.676	Suprime-Cam	NA671	R	observed
	RXJ0152.7–1357	0.837	[OIII]	0.920	Suprime-Cam	NB921	z'	not yet
High-z clusters	XCSJ2215–1738	1.457	[OII]	0.916	Suprime-Cam	NB912, NB921	z'	Hayashi+'10, '12
	4C65.22	1.516	Hα	1.651	MOIRCS	NB1657	H	Koyama+'14
	CL0332–2742	1.61	[OII]	0.973	Suprime-Cam	NB973	y	observed
	ClGJ0218.3–0510	1.62	[OII]	0.977	Suprime-Cam	NB973	y	Tadaki+'12
Proto-clusters	PKS1138–262	2.156	Hα	2.071	MOIRCS	NB2071	K_s	Koyama+'12
	HS1700+64	2.30	Hα	2.156	MOIRCS	BrG	K_s	observed
			[OIII]	1.652	MOIRCS	[Fe II]	H	not yet
	4C23.56	2.483	Hα	2.286	MOIRCS	CO	K_s	Tanaka+'11
	USS1558–003	2.527	Hα	2.315	MOIRCS	NB2315	K_s	Hayashi+'12
	MRC0316–257	3.130	[OII]	2.539	MOIRCS	NB1550	H	not yet
			[OIII]	2.068	MOIRCS	NB2071	K_s	observed
General fields	SXDF-CANDELS	2.16	Hα	2.071	MOIRCS	NB2071	K_s	observed
	(90 arcmin^2)	2.19	Hα	2.094	MOIRCS	NB2095	K_s	Tadaki+'13
		2.53	Hα	2.315	MOIRCS	NB2315	K_s	Tadaki+'13
		3.17	[OIII]	2.093	MOIRCS	NB2095	K_s	Suzuki+'14
		3.63	[OIII]	2.317	MOIRCS	NB2315	K_s	Suzuki+'14
	COSMOS-CANDELS	2.16	Hα	2.071	MOIRCS	NB2071	K_s	partly observed
	(90 arcmin^2)	2.19	Hα	2.094	MOIRCS	NB2095	K_s	partly observed
	GOODS-N	2.19	Hα	2.094	MOIRCS	NB2095	K_s	Tadaki+'11
	(70 arcmin^2)		[OII]	1.189	MOIRCS	NB1190	J	observed

Figure 2.3: The current status of Mahalo-Subaru project (*Credit: Tadayuki Kodama*).

2008; Sobral et al. 2013, 2014; Khostovan et al. 2015, 2016).

The catalogs of the emitters obtained by their four NB filters are now publicly available (Sobral et al., 2013), and they have constructed samples of [OIII] emitters at $z = 0.84$, 1.42, 2.23, and 3.24 (Khostovan et al., 2015). In this *Thesis*, we use the NB emitter catalogs from HiZELS as well as those of our own project, Mahalo-Subaru.

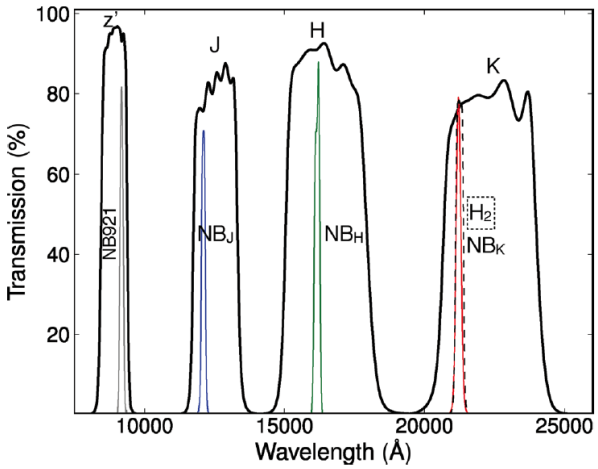

Figure 2.4: The transmission curves of the BB and NB filters used in HiZELS (Sobral et al., 2013). The NB filters in the z' (Subaru/Suprime-Cam), J, H, and K-bands (UKIRT/WFCAM) catch the redshifted Hα line at $z = 0.40$, 0.85, 1.47, and 2.23, and [OIII]λ5007 line at $z = 0.84$, 1.42, 2.23, and 3.24, respectively, for example (Sobral et al., 2013; Khostovan et al., 2015).

3 [OIII] EMISSION LINE AS A USEFUL TRACER OF STAR-FORMING GALAXIES AT HIGH REDSHIFTS

The Hα emission line is one of the best tracers of star formation because it is less affected to dust extinction than the UV light and the relation between SFRs and Hα luminosities has been well calibrated in the local Universe (e.g. Hopkins et al. 2003). In this chapter we compare the galaxies traced by the [OIII] emission line with those traced by the Hα emission line at $z = 2.23$ using the NB imaging data obtained by HiZELS. We investigate a usefulness of the [OIII] emission line as a tracer of star-forming galaxies at high redshifts.

At $z \sim 0$ and ~ 1.5, the selection biases between Hα and [OIII] have been investigated using the Sloan Digital Sky Survey (SDSS) and Fiber Multi-Object Spectrograph(FMOS)-Cosmological Evolution Survey (COSMOS) galaxies (Silverman et al., 2015) by Juneau et al. (in preparation). Their sample is selected based on Hα and [OIII] luminosities. Mehta et al. (2015) investigated the relation between Hα and [OIII] luminosity for galaxies at $z \sim 1.5$ in *HST*/WFC3 Infrared Spectroscopic Parallel (WISP) Survey (Atek et al., 2010), and derived the Hα–[OIII] bivariate luminosity function at $z \sim 1.5$. At $z \gtrsim 2$, on the other hand, a comparison between Hα-selected and [OIII]-selected galaxies has not been done yet. In order to accurately interpret results from [OIII] emitter survey at $z > 3$, it is required to understand what galaxy population is traced by the [OIII] emission line selection at $z \gtrsim 2$.

*This chapter is based on Suzuki et al. (2016).

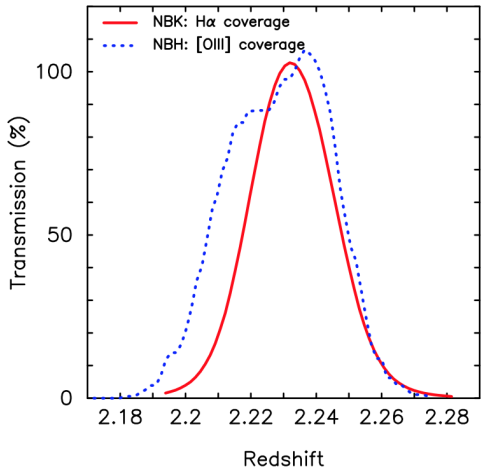

Figure 3.1: A comparison between the NB_H redshift coverage for the [OIII]λ5007 emission line (dotted line) and the NB_K redshift coverage for the Hα emission line (solid line). We can obtain two samples of the [OIII] emitters and Hα emitters at z=2.23 with the two NB filters. The redshift coverage of of [OIII]λ5007 is slightly wider than that of the Hα. The y axis is shown in an arbitrary scale.

3.1 Data and analysis

In this study, we use the two samples of emitters at z=2.23 obtained by HiZELS. An advantage in the design of the NB filters of HiZELS is the symmetry in respect to their wavelength centers, such that an [OIII] emission line can be detected in NB_H and Hα in NB_K with both detections occurring at z=2.23 (Figure 3.1 and Table 3.1).

The catalogues of Hα emitters and [OIII] emitters at z=2.23 used in this study are taken from Sobral et al. (2013) and Khostovan et al. (2015), respectively. We use the catalogues in the COSMOS field. The selection criteria of these emitters are described in detail in the two papers. Here we briefly summarize the selection methods in the following subsections.

3.1.1 Selection of Hα and [OIII] emitters at z=2.23

The NB excess sources are selected with the selection criteria of $\Sigma > 3$ and $EW_{rest} = 25$ Å for both NB_H and NB_K (Sobral et al., 2013; Khostovan et al., 2015). In the HiZELS, the redshift identification of the NB emitters for NB_H and NB_K is performed based on the photometric redshifts, broad-band colors (color–color selections) and the spectroscopic

Table 3.1: The central wavelength, FWHM, and redshift coverage (for [OIII]λ5007 or Hα) of NB filters in the H and K-band used in HiZELS (Sobral et al., 2013).

Filter	λ_c [μm]	FWHM [Å]	Redshift coverage
NB_H	1.617	211	2.23 ± 0.021 for [OIII]λ5007
NB_K	2.121	210	2.23 ± 0.016 for Hα

redshifts. Here we give the priorities in the following order (from higher to lower): (1) spectroscopic redshifts, (2) photometric redshifts, and (3) color–color selections (Sobral et al., 2013; Khostovan et al., 2015). If the sources are spectroscopically confirmed to be the targeted line emitters, they are firmly identified as the Hα or [OIII] emitters. The numbers of such Hα and [OIII] emitters which are confirmed with the spectroscopic redshifts are only three and one, respectively (Sobral et al., 2013; Khostovan et al., 2015). Secondly, if the sources have the photometric redshifts within $1.7 < z_{\rm phot} < 2.8$, they are robustly identified as the Hα or [OIII] emitters at $z \sim 2.23$. Here, the photometric redshifts are taken from the catalog of Ilbert et al. (2009).

Color–color diagrams are also applied for the redshift separation of the emitters. For the NB_K emitters, the $(z - K)$ versus $(B - z)$ color–color diagram is used to sample additional faint Hα emitters at $z \sim 2$, which lack reliable photometric redshifts. In addition to the BzK selection, the photometric redshift criteria of $z_{\rm photo} < 3.0$ or the color–color diagram of $(B - R)$ versus $(U - B)$ are applied to remove higher-redshift sources (Sobral et al., 2013). For the NB_H emitters, the BzK color–color diagram is used to remove the foreground sources at $z < 1.5$, and additionally, the $(z - K)$ vs $(i - z)$ diagram is applied to separate the potential $z = 1.47$ Hα emitters. In order to remove the higher redshift sources, the $(V - z)$ versus $(U - V)$ diagram is used (Khostovan et al., 2015).

Note that Sobral et al. (2013) and Khostovan et al. (2015) applied slightly different color–color diagrams because the other strong emission lines that could contaminate the samples (and hence the redshifts of the foreground and background galaxies that need to be excluded) are different for the two NB filters. We confirm that there is no systematic difference in the distributions of the Hα and [OIII] emitters at $z \sim 2.23$ on any of the color–color diagrams mentioned above. We consider that the color–color selection for the

NB_K and NB_H emitters are consistent with each other. In this study, we follow the color–color selection criteria for each NB filter. This difference does not cause any systematic differences between the two emitter samples.

The number of the redshift-identified Hα and [OIII] emitters at $z = 2.23$ is 513 and 172, respectively.

3.1.2 AGN contribution of the two emitter samples

We use the X-ray observations and *Spitzer*/IRAC colors to investigate the contribution of AGNs to our Hα emitter and [OIII] emitter samples at $z = 2.23$.

The redshift-identified Hα and [OIII] emitters are matched with the X-ray point source catalog from the *Chandra* COSMOS Legacy survey (Civano et al., 2016) in order to identify obvious AGNs. The fraction of the X-ray-detected sources is only 2.3% and 3.5% for the Hα emitters and [OIII] emitters, respectively. We remove these X-ray-detected sources from the two emitter samples.

We also estimate the fractions of obscured AGN candidates in the Hα and [OIII] emitters. The colors in *Spitzer*/IRAC four channels are commonly used to identify obscured AGNs (e.g. Lacy et al. 2007; Stern et al. 2005; Donley et al. 2008). We here use only the sources detected at more than the 2σ level in all four channels of IRAC, which limited our Hα and [OIII] emitter samples to only 15% and 17% (76 and 29 sources), respectively. When we use the $S_{5.8}/S_{3.6}$–$S_{8.0}/S_{4.5}$ diagram with the selection criteria of Donley et al. (2012), the fraction of the emitters which can be classified as AGNs is $\sim$14% for both the Hα and [OIII] emitter samples. This fraction must be an over estimation of the true fraction. Given the fact that the bright Hα emitters are more likely to be AGNs (Sobral et al., 2016), using only the emitters that are bright enough in all four IRAC channels might cause a higher AGN fraction than the true fraction.

We note that the fractions of the X-ray-detected sources or IRAC-color-selected AGNs are not different between the Hα emitters and [OIII] emitters at $z = 2.23$, indicating that the [OIII] emitters do not necessarily show the higher fraction of AGNs as compared to the Hα emitters.

3.1.3 Final samples of the two emitters

The HiZELS NB survey in the COSMOS field covers a very wide area of 1.6 deg^2, but the survey depth is different among the WFCAM pointings and among different NB filters (see Sobral et al. 2013). In this study, in order to ensure the same flux limit for both NB-selected samples, we use the sources in the deepest pointings only. The minimum exposure times are 107 ks and 62.5 ks for NB_H and NB_K, respectively. The survey area is then limited to the central $\sim$ 0.2 deg^2. The 3σ limiting fluxes for NB_H and NB_K are 3.60×10^{-17} erg s^{-1}cm^{-2} and 2.96×10^{-17} erg s^{-1}cm^{-2}, respectively. In this study, we apply the same flux limit of 3.6×10^{-17} erg s^{-1}cm^{-2} ([OIII] flux for NB_H and Hα+[NII] flux for NB_K). As a result, 49 [OIII] emitters and 44 Hα emitters remain in our final samples.

In Section 3.2.3, we focus on the galaxies detected with both [OIII] and Hα emission lines (hereafter, dual emitters). When we search for the counterpart line, we lower the line detection threshold, as we can trust more the existence of a line at the expected wavelength in the other NB filter. We thus use the lower NB_H (NB_K) excess criteria, namely, EW $\gtrsim$ 15 Å and/or $\Sigma \gtrsim 2$. We find 23 dual emitters in total. Among them, ten sources satisfy the original NB excess criteria of both NB_H and NB_K, indicating that they have the strong [OIII] and Hα emission lines. Eleven (two) sources are the Hα ([OIII]) emitters with the relatively weak [OIII] (Hα) emission lines. The number of sources in each sample used here is summarized in Table 3.2.

We note that the transmission curves of NB_H and NB_K filters are not completely matched (Figure 3.1). The wavelength coverages of the two filters are transformed to the redshift space for each line in Figure 3.1 and Table 3.1. It turns out that $\sim$10% of the NB_H redshift coverage ([OIII]λ5007) is completely out of the NB_K redshift coverage (Hα). In terms of FWHM ranges of the two NB filters, 24% of the NB_H coverage is out of the NB_K coverage in redshift space. This mismatch of the redshift coverage is not critical when we compare the Hα emitters and [OIII] emitters in Section 3.2.2. On the other hand, when we consider the sample of galaxies detected only by the [OIII] emission line, the impact of this difference could be larger. The redshift mismatch might cause the loss of Hα flux from the galaxies which actually have the strong enough Hα emission line, and thus the observed [OIII]/Hα ratio would become different from the intrinsic ratio. In such a case, the Hα flux would seem much lower with respect to [OIII], and in the extreme case, the

Table 3.2: Summary of samples and subsamples used in this study.

Name	Number of sources	Notes
Hα emitters	44	–
[OIII] emitters	49	–
Hα-single-emitters	23	Hα emitters with no [OIII] emitter counterpart
[OIII]-single-emitters	37 [i)]	[OIII] emitters with no Hα emitter counterpart
Dual emitters	23	Hα + [OIII] emitters (dual emitters)

i) We note that the number of the [OIII] emitters with no Hα emitter counterpart is larger than that of the Hα emitters with no [OIII] emitter counterpart. Some [OIII] emitters might be [OIII]λ4959 or Hβ emitters as discussed in Section 3.1.4, and thus they do not have Hα emitter counterparts.

emitter would appear as an [OIII] emitter with no Hα emitter counterpart. Therefore, "[OIII]-single-emitters" (see Table 3.2 for the definition) may include some dual emitters, and one should use caution when comparing the properties of this subsample with others.

3.1.4 Contribution of Hβ and [OIII]λ4959 emitters

There are the two lines which are close to our target line ([OIII]λ5007), namely, [OIII]λ4959 and Hβ at $\lambda = 4861$ Å. The wavelength coverage of NB_H is too narrow to include both the Hβ and [OIII] lines simultaneously. The [OIII] doublet lines can be detected at the same time at the the opposite edges of NB_H for some galaxies in a narrow redshift range of $\Delta z \sim 0.01$. The fraction of such emitters is expected to be small ($\sim$7% of the [OIII]+Hβ emitters at $z = 1.47$; see the full analysis from spectroscopy in Sobral et al. 2015).

We note that Hβ or [OIII]λ4959 at slightly different redshifts can not be actually distinguished from our target [OIII]λ5007 emitters at $z = 2.23$ by photometric redshifts and broad-band color selections because their redshifts are too close to separate only with photometric data (Khostovan et al., 2015). We estimate the fraction of such Hβ and [OIII]λ4959 emitters included in the NB_H emitters by considering the luminosity functions of Hβ and [OIII]λ4959.

The luminosity functions of the Hβ and [OIII]λ4959 line are determined by converting the luminosity functions of the Hα (Sobral et al., 2013) and [OIII] line (Colbert et al., 2013)

assuming the line ratios of Hα/H$\beta \sim 5$ incorporating the effects of dust based on the observations of Hayashi et al. (2011) and Shimakawa et al. (2015), and [OIII]λ5007/[OIII]λ4959 = 3 (the theoretical ratio; Storey & Zeippen 2000), respectively. With our 3σ detection limit of 3.6×10^{-17} erg s^{-1}cm^{-2}, the contribution of the Hβ emitters is estimated to be $\sim$3%. Similarly, the contribution of the [OIII]λ4959 emitters is estimated to be 25%.

We note that the fraction of [OIII]λ4959 is not negligible. However, since the galaxies with strong [OIII]λ4959 should have even stronger [OIII]λ5007 emission given the line ratio, the [OIII]λ4959 emitters and the emitters which are detected with both the [OIII] doublet lines can also be regarded as the [OIII]λ5007 emitters. Spectroscopic follow-up observations are necessary to accurately quantify the contribution of the Hβ and [OIII]λ4959 emitters at $z \sim 2$.

In summary, taking into account the relative strength of [OIII]λ5007 as compared to [OIII]λ4959 and Hβ, we consider that the majority of the NB$_H$ emitters are the [OIII]λ5007 emitters once we apply the redshift identification in Section 3.1.1. Moreover, our [OIII]λ5007 line flux is not contaminated by [OIII]λ4959 or Hβ at the same redshift for most of the emitters.

3.1.5 Estimation of physical quantities

Stellar masses are estimated from SED fitting with a stellar population synthesis model based on the public code `EAZY` (Brammer, van Dokkum & Coppi, 2008) and `FAST` (Kriek et al., 2009b). We use 16 photometric band data, FUV, NUV, u, B, V, g, r, i, $I_{\rm c}$, z, J, K, 3.6, 4.5, 5.8, and 8.0 μm obtained from the photometric catalog of Ilbert et al. (2009). For the sources detected with NB$_K$, Hα+[NII] line fluxes are subtracted from the K-band fluxes before performing the SED fitting. The contribution of Hα+[NII] fluxes corresponds to $\sim$ 20% of the K-band fluxes on average. The redshift of the galaxies is fixed to $z = 2.23$. We use the stellar population synthesis model of Bruzual & Charlot (2003) with the Salpeter initial mass function (IMF; Salpeter 1955) and the dust extinction law of Calzetti et al. (2000). We assume exponentially declining star formation history (SFH) in the form of SFR $\sim \exp(-t/\tau)$, with $\log(\tau/{\rm yr})$= 8.5–10.0 in steps of 0.1, and the metallicities of 0.004, 0.008, 0.02 (solar) and 0.05, similar to the analysis of Sobral et al. (2014).

We estimate the rest-frame 1600 Å luminosity at $z = 2.23$ using the V-band photometry

from Ilbert et al. (2009), and convert $L(1600\ \text{Å})$ to the UV star formation rates (SFR_{UV}) as mentioned below. Dust extinction is corrected for using the slope of the rest-frame UV continuum spectrum (e.g. Meurer, Heckman & Calzetti 1999; Heinis et al. 2013). The UV slope β is defined as $f_\lambda \propto \lambda^\beta$. We estimate β by fitting a linear function to the five broad-band photometries from the B to i-band. The slope β is converted to the dust extinction A_{FUV} with the following equation from Heinis et al. (2013):

$$A_{\text{FUV}} = 3.4 + 1.6\beta. \tag{3.1}$$

Then, the intrinsic flux density $f_{\nu,\text{int}}$ is obtained from

$$f_{\nu,\text{int}} = f_{\nu,\text{obs}}\ 10^{0.4 A_{\text{FUV}}}. \tag{3.2}$$

SFRs are estimated from UV luminosities adopting the equation from Madau, Pozzetti & Dickinson (1998):

$$\begin{aligned} \text{SFR}\ (\text{M}_\odot \text{yr}^{-1}) &= \frac{4\pi D_L^2 f_{\nu,\text{int}}}{(1+z) \times 8 \times 10^{27}\ (\text{erg s}^{-1}\text{cm}^{-2}\text{Hz}^{-1})} \\ &= \frac{L(1600\text{Å})}{8 \times 10^{27}\ (\text{erg s}^{-1}\text{Hz}^{-1})}, \end{aligned} \tag{3.3}$$

where D_L is the luminosity distance. Here, the Salpter IMF is adopted.

For the sources with Hα detections, we also derive $\text{SFR}_{\text{H}\alpha}$. Since we obtain H$\alpha$+[NII] fluxes from the NB_K imaging observations, [NII] line fluxes should be removed from the total NB fluxes. The contribution of the [NII] flux is estimated from the EW of Hα+[NII] as shown in Sobral et al. (2013). We then estimate $\text{SFR}_{\text{H}\alpha}$ using the relation between SFRs and Hα luminosities of Kennicutt (1998b):

$$\text{SFR}_{\text{H}\alpha}(\text{M}_\odot \text{yr}^{-1}) = 7.9 \times 10^{-42} \frac{L_{\text{H}\alpha}}{\text{ergs}^{-1}}. \tag{3.4}$$

The dust extinction for Hα emission is estimated from A_{FUV} by assuming the Calzetti extinction law (Calzetti et al., 2000):

$$E(B-V)_{\text{stellar}} = A'_V / R'_V, \tag{3.5}$$

$$A'(\lambda) = k'(\lambda) E(B-V)_{\text{stellar}}, \tag{3.6}$$

and

$$k'(\lambda) = \begin{cases} 2.659(-2.156 + 1.509/\lambda - 0.198/\lambda^2 + 0.011/\lambda^3) + R'_V & (0.12\mu\mathrm{m} \leqslant \lambda \leqslant 0.63\mu\mathrm{m}), \\ 2.659(-1.857 + 1.040/\lambda) + R'_V & (0.63\mu\mathrm{m} \leqslant \lambda \leqslant 2.20\mu\mathrm{m}). \end{cases} \tag{3.7}$$

$E(B-V)_{\mathrm{stellar}}$ indicates the amount of reddening in the stellar continuum, and $R'_V = 4.05$ for starburst galaxies (Calzetti et al., 2000).

We assume that there is no extra extinction for the nebular emissions compared to the stellar extinction, i.e. $E(B-V)_{\mathrm{stellar}} = E(B-V)_{\mathrm{nebula}}$ (e.g. Erb et al. 2006b; Reddy et al. 2010, 2015), although this is still under the debate. We compare the SFRs derived from two different indicators, UV luminosities and Hα luminosities, in Figure 3.2. We find that the $\mathrm{SFR_{UV}}$ and $\mathrm{SFR_{H\alpha}}$ are broadly consistent with each other within a factor of 2, indicating that we can estimate SFRs reasonably well with UV luminosities with dust correction based on the UV slope. For the three sources with the highest $\mathrm{SFR_{UV}}$, their SFRs derived from Hα are apparently smaller than those from UV luminosities. The difference between the dust extinction to the ionized gas and stellar continuum might be involved in such an inconsistency, because previous studies targeting the galaxies with relatively higher SFRs or higher stellar masses on average have indicated that the ionized gas are more strongly affected by dust extinction than the stellar continuum (e.g. Förster Schreiber et al. 2009; Kashino et al. 2013). In the following analysis, SFRs of all the sources are represented by $\mathrm{SFR_{UV}}$. This allows us to compare SFRs between the Hα emitters and [OIII] emitters with the same SFR indicator.

3.2 Results and discussion

3.2.1 Stellar mass–SFR relation

We investigate the relation between stellar masses and UV-derived SFRs ($\mathrm{SFR_{UV}}$) for the NB-selected galaxies at $z = 2.23$. In Figure 3.3, we see a positive correlation for both our Hα emitters and [OIII] emitters. Importantly, the distributions of the two samples on the stellar mass–SFR diagram are not significantly different from each other. The dual emitters are also shown on the plot, and we discuss this population in Section 3.2.3. Each symbol is color coded according to the dust extinction A_{FUV}. We can see the trend

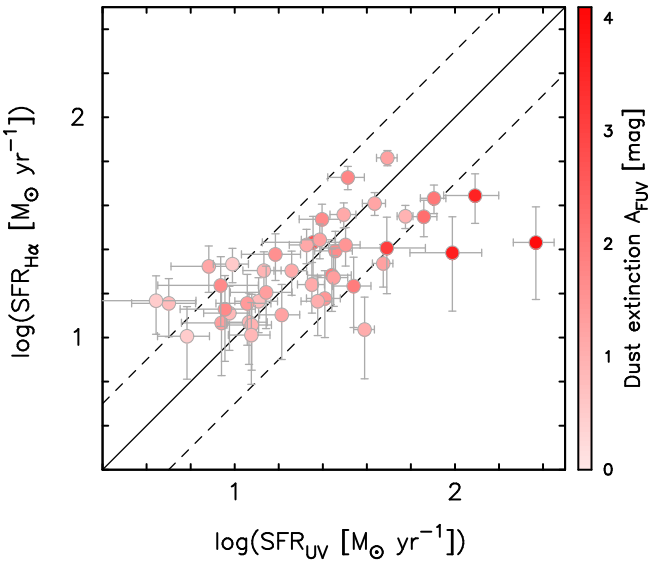

Figure 3.2: Comparison of SFRs derived from UV luminosities and Hα luminosities for the Hα emitters at $z = 2.23$. Dust extinction correction is based on the UV slope β. We assume that there is no extra extinction to emission lines as compared to the extinction to the stellar continuum. The strength of colors are corresponding to the dust extinction $A_{\rm FUV}$. The solid line represents the case where the two SFRs are identical, and the dashed lines represents the case where a difference between the two is a factor of 2.

that the galaxies with higher stellar mass and/or higher SFR typically show higher dust extinction.

3.2.2 Comparison of physical quantities between the Hα and [OIII] emitters

In this section, we compare the two samples, the Hα emitters and [OIII] emitters at $z = 2.23$, regardless of whether they are the dual emitters or not. We compare the distribution of the integrated physical quantities, such as a stellar mass, dust extinction, SFR$_{\rm UV}$, and specific SFR$_{\rm UV}$ (sSFR = SFR/M_*[yr^{-1}]) in Figure 3.4.

In order to investigate whether there are any systematic differences between the two samples, we use a Kolmogorov-Smirnov (KS) test. The p-values from the KS-test are summarized in Table 3.3. The p-values for all the physical quantities are larger than 0.05,

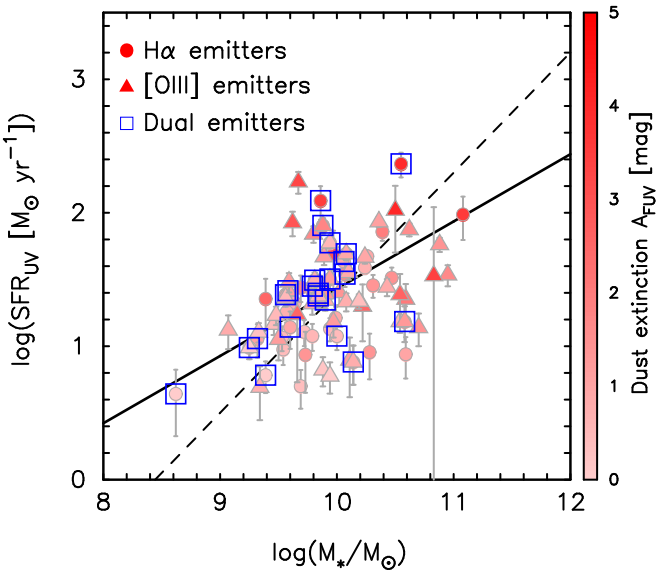

Figure 3.3: Stellar mass and SFR relation of the NB-selected galaxies at $z = 2.23$. SFRs are derived from UV luminosities and corrected for the dust extinction using the UV slope β. The strength of the colors corresponds to $A_{\rm FUV}$. The dashed line shows the stellar mass–$\rm SFR_{UV}$ relation of the UV-selected galaxies at $z \sim 2$ from Daddi et al. (2007). The solid line represents the relation derived from the Hα emitters at $z = 2.2$ with $M_* \geq 10^{10} M_\odot$ from HiZELS (Koyama et al., 2013), although SFRs are derived based on Hα luminosities rather than UV luminosities.

meaning that the Hα emitters and [OIII] emitters are consistent with being drawn from the same population. As shown in Figure 3.4, the galaxies selected by [OIII] emission at $z = 2.23$ occupy almost the same ranges in their integrated properties with those of the galaxies selected by Hα. This suggests that the [OIII]-selected galaxies trace the same general population as the Hα-selected galaxies.

3.2.3 Hα+[OIII] dual emitters at $z = 2.23$

We divide the whole emitter sample into three subsamples according to the detections of the Hα and [OIII] emission lines as defied in Section 3.1.3, namely the galaxies detected with only the Hα emission line (Hα-single-emitters), the galaxies detected with only the [OIII] emission line ([OIII]-single-emitters), and the "dual emitters" which are detected with both the Hα and [OIII] lines. The numbers of galaxies in each sample is summarized

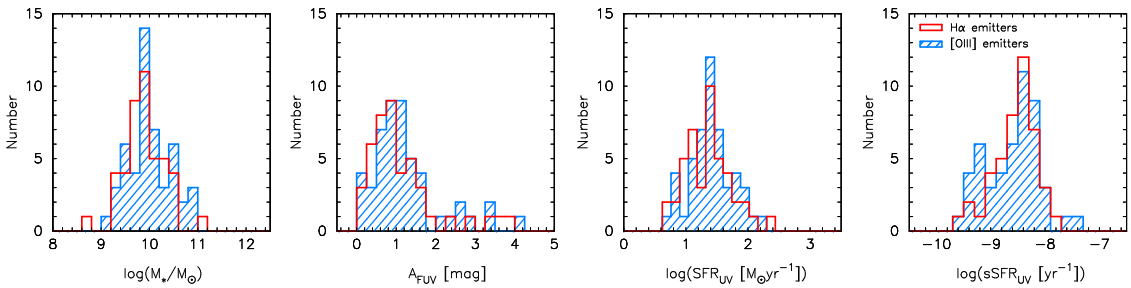

Figure 3.4: Number distributions of a stellar mass, dust extinction ($A_{\rm FUV}$), $\rm SFR_{UV}$, $\rm sSFR_{UV}$ from left to right. The open and hatched histograms represent Hα emitters and [OIII] emitters, respectively.

Table 3.3: The p-values from the KS test of comparisons of physical quantity distributions between the Hα emitters and [OIII] emitters as shown in Figure 3.4.

	$\rm M_*$	$A_{\rm FUV}$	$\rm SFR_{UV}$	$\rm sSFR_{UV}$
Hα emitters versus [OIII] emitters	0.76	0.69	0.56	0.77

in Table 3.2.

Figure 3.5 shows the number distribution of the same quantities as in Figure 3.4 but now for the three subsamples. We perform a KS test, and the resulting p-values are listed in Table 3.4. For almost all of them, except for only two particular cases, the p-values are greater than 0.05, and we can statistically consider that all the emitter samples are drawn from intrinsically similar distributions.

The two exceptions are the comparison of $\rm sSFR_{UV}$ between the Hα-single-emitters and the dual emitters, and between the [OIII]-single-emitters and the dual emitters. Figure 3.5 shows that the dual emitters tend to have higher $\rm sSFR_{UV}$ as compared to the other two subsamples.

Considering the comparison between the Hα-single-emitters and the dual emitters, this result indicates that the star-forming galaxies with relatively stronger [OIII] emission lines tend to have higher star-forming activity with respect to their stellar masses. This can be understood by the following arguments. Since high $\rm sSFR_{UV}$ produces more UV flux per volume, it leads to more extreme ISM condition characterized by the higher ionization parameter and thus showing the strong [OIII] emission line with respect to Hα (Kewley et

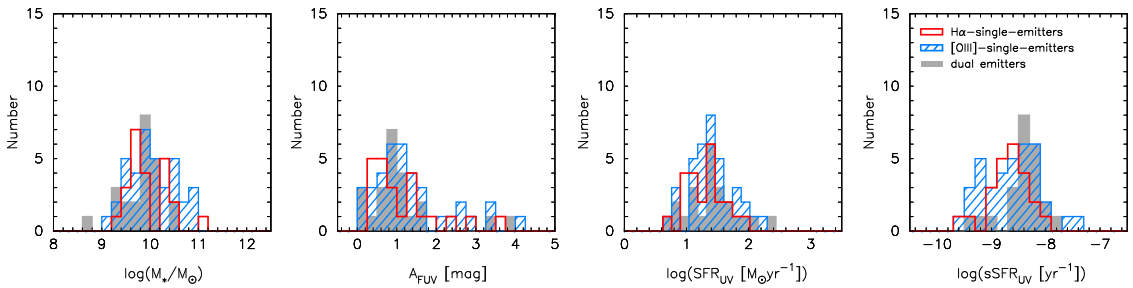

Figure 3.5: Number distributions of a stellar mass, dust extinction ($A_{\rm FUV}$), $\rm SFR_{UV}$, $\rm sSFR_{UV}$ from left to right. The emitter samples are divided into three subsamples, Hα-single-emitters (open histograms), [OIII]-single-emitters (hatched histograms), and dual emitters (filled histograms).

al., 2015). Therefore, the dual emitters, which tend to have the stronger [OIII] emission lines than the Hα-single-emitters, are likely to show higher $\rm sSFR_{UV}$.

On the other hand, a possible difference between the [OIII]-single-emitters and the dual emitters is not straightforward to interpret because the [OIII]-single-emitters should also have the stronger [OIII] emission line with respect to the Hα emission line. At lower $\rm sSFR_{UV}$ regime ($\log(\rm sSFR_{UV}[yr^{-1}]) \lesssim -9.0$), the [OIII]-single-emitters show a larger fraction of galaxies as compared to the dual emitters. This may be caused by a contribution of faint AGN, but in order to investigate the presence of faint AGN in our sample, deep spectroscopy and line diagnostic analysis would be necessary. We here also note that there is a contamination of the [OIII]λ4959 and Hβ emitters in our [OIII]-only-selected galaxies as mentioned in Section 3.1.4. These emitters would be misclassified as the [OIII]-single-emitters even if they actually have the strong Hα emission line. In such a case, the stellar masses might be overestimated because of the contribution of Hα (and [NII]) fluxes to the K-band fluxes, and the [OIII]λ4959 and Hβ emitters could contribute to the lower sSFRs seen in the [OIII]-single-emitters.

At this point, we are not able to further investigate the cause of such difference, and we leave it for future investigation. However, it should be stressed that except for the two particular cases, the physical properties of the three emitter subsamples are not statistically different.

Table 3.4: The p-values from the KS test of comparisons of physical quantity distributions among the three subsamples as shown in Figure 3.5.

	M_*	A_{FUV}	SFR_{UV}	$sSFR_{UV}$
Hα-single-emitters versus [OIII]-single-emitters	0.85	0.63	0.56	0.57
Hα-single-emitters versus dual emitters	0.36	0.84	0.59	0.006
[OIII]-single-emitters versus dual emitters	0.12	0.36	0.97	0.04

3.2.4 Biases due to NB selection

Finally, we discuss possible biases introduced by the NB selection, which are based on the flux and EW of emission lines.

As shown in Shimakawa et al. (2015) and Holden et al. (2016), the [OIII]/Hβ (or [OIII]/Hα) ratio is correlated with sSFR of star-forming galaxies in the sense that the galaxies with higher sSFRs tend to show the larger [OIII]/Hα ratios. Given the fact that the EW of Hα is directly proportional to sSFR (e.g. Leitherer et al. 1999), the flux- and EW-limited sample might be biased towards the galaxies with the larger [OIII]/Hβ ratios. In such a case, the Hα emitters and [OIII] emitters might show similar properties because the Hα emitters tend to consist of the galaxies with relatively strong [OIII] emission line.

Sobral et al. (2014) investigated the relation between the rest-frame EW(Hα+[NII]) and stellar mass of the Hα emitters at z = 0.4, 0.8, 1.5, and 2.2 obtained by HiZELS. They found that the Hα emitters at $z \sim$ 1–2.2 distribute well above the EW(Hα+[NII]) cut of 25 Å up to a stellar mass of $\log(M_*/M_\odot) \sim 11.5$ (fig3 in Sobral et al. (2014)). The relation between the rest-frame EW and stellar mass was also investigated for the [OIII]+Hβ emitters by Khostovan et al. (2016). Their results show that the [OIII]+Hβ emitters at $z > 1$ have much higher EW than the limit. It is expected that our samples are not strongly affected by the EW cut.

3.3 Summary of this chapter

In this chapter, we use the catalog of NB-selected galaxies at $z = 2.23$ obtained by HiZELS, and construct the two galaxy samples of Hα emitters and [OIII] emitters by applying the same flux limit. We derive the physical quantities, such as a stellar mass, dust extinction

($A_{\rm FUV}$), $\rm SFR_{UV}$, and $\rm sSFR_{UV}$, and compare the number distributions of these quantities between the two samples. From the KS-test, we find that the Hα emitters and [OIII] emitters are drawn from the same parent population. The two galaxy populations are not statistically different at $z = 2.23$.

We also divide the whole sample into three subsamples according to the detections of the Hα and [OIII] emission lines. Among the three subsamples, again, the number distributions of the physical quantities are not statistically different, except for the dual emitters, which tend to show higher $\rm sSFR_{UV}$ as compared to the other two subsamples. It is indicated that the strong [OIII] emission lines are likely to be related to high star formation activity (and thus high ionization parameter) of star-forming galaxies at $z \sim 2$. Note, however, that [OIII] emitters and Hα emitters used in this study could harbor low-luminosity AGN, especially the [OIII]-single-emitters with lower sSFR as discussed in Section 3.2.3, and spectroscopic observations are necessary to confirm the presence of AGN.

In summary, the [OIII] emitters cover almost the same ranges of the physical quantities as the Hα emitters at $z = 2.23$, and therefore we argue that the [OIII] emission line can be useful as a tracer of star-forming galaxies at high redshifts. Our results support the importance and effectiveness of the [OIII] emitter surveys at $z > 3$, where the Hα emission line is no longer accessible from the ground.

4 Probing the star-forming activity of galaxies before the peak epoch with [OIII] emitters

In Chapter 2, we have shown the usefulness of the [OIII] emission line as a tracer of star-forming galaxies at high redshifts. Now we investigate the star-forming activity of galaxies at $z > 3$ using the [OIII]-selected galaxies obtained by Mahalo-Subaru ($z = 3.2,\ 3.6$) and HiZELS ($z = 3.24$) projects. The samples from both surveys are obtained in the general field, the SXDF and COSMOS, respectively. In this chapter, we compare the star-forming activity of the [OIII] emitters at $z > 3$ with the NB-selected star-forming galaxies at $z \sim 2$ in order to discuss the difference between the two epochs. For the [OIII] emitters in the SXDF, the high angular resolution images from *HST*/WFC3 are also available, and we investigate their sizes as a function of their stellar masses.

4.1 [OIII] emitters in the SXDF

4.1.1 Data and sample selection

The NB imaging observation at the SXDF-UDS-CANDELS field was performed as a part of Mahalo-Subaru project. The details of the observations and the data reduction are described in Tadaki et al. (2013).

The two NB filters, namely NB2095 and NB2315, are used in this filed. The NB2095 and NB2315 filters can probe the Hα emission line at $z = 2.188 \pm 0.020$ and $z = 2.530 \pm 0.020$, and also the [OIII] emission line at $z = 3.179 \pm 0.026$ and $z = 3.626 \pm 0.026$,

*The parts about the [OIII] emitters in the SXDF obtained by Mahalo-Subaru are based on Suzuki et al. (2015).

respectively. The total observed areas were 91 arcmin^2 and 93 arcmin^2 for NB2095 and NB2315, respectively. The exposure times were 140–186 minutes, and the seeing sizes were $0''.5$–$0''.7$ (FWHM). The 5σ limiting magnitudes with $1''.6$ diameter aperture were 23.6 and 22.88 mag in NB2095 and NB2315. The observed data were reduced with the MOIRCS imaging pipeline software (`MCSRED`[1]; Tanaka et al. 2011), The point-spread function (PSF) were smoothed to $0''.7$ when combining all the images.

First of all, we select NB excess sources using the color–magnitude diagram as shown in Figure 2.2. Our selection criteria of NB excess sources are $\Sigma > 3$, $HK - \mathrm{NB} > 0.4$ mag, and $m_{\mathrm{NB}} > m_{\mathrm{NB},5\sigma}$ as mentioned in Section 2.2. As a result, we obtain 101 and 58 NB excess sources in NB2095 and NB2315, respectively (Tadaki et al., 2013). In order to separate the redshifts of NB emitters, Tadaki et al. (2013) used an $(i' - J)$ versus $(J - K)$ diagram for NB2095 emitters and $(i' - H)$ versus $(H - K)$ diagram for NB2315 emitters. They have shown that [OIII] emitters at $z > 3$ and Hα emitters at $z < 3$ can be well separated by the dividing lines as shown in Figure 4.1. We follow their selection methods, and here the contribution from the emission line is subtracted from the K-band magnitude. Some of these NB emitters may be Paα emitters at low redshifts ($z = 0.1$–0.2). Since the Paα emitters should appear in the same regions as the Hα emitters on these diagrams, they should not be major contaminants for our [OIII] emitters. We have thus finally obtained strong candidates for [OIII] emitters: 27 at $z = 3.18$ and 7 at $z = 3.62$.

Figure 4.2 shows the relation between stellar masses and dust-extinction-uncorrected SFRs measured from [OIII] line luminosities for the [OIII] emitters in order to verify our sample selection. We will explain our method of measuring a stellar mass and SFR in Section 4.1.3. Our criteria of determining NB excesses, namely $\Sigma > 3$ and $HK - \mathrm{NB} = 0.4$ mag, correspond to the limits of $\mathrm{SFR}_{[\mathrm{OIII}]} > 4.5$ $\mathrm{M}_\odot \mathrm{yr}^{-1}$ and $\mathrm{EW}_{\mathrm{rest}} > 30$ Å, respectively. We draw a line corresponding to the EW cut on the M_*–SFR diagram by establishing a relation between stellar mass and SFR along the threshold of $HK - \mathrm{NB2095} = 0.4$. As proxies of the $H - K$ and $J - K$ colors along this boundary line, we use the averaged colors of the three objects that are located nearest to the boundary of $HK - \mathrm{NB2095} = 0.4$. Then, for a given NB magnitude, we assign a K-band magnitude using $HK - \mathrm{NB2095} = 0.4$ and the above $H - K$ color. A stellar mass is then estimated from the K-band magnitude and the above $J - K$ color. $J - K$ color is used to correct for the mass-to-light ratio

[1] http://www.naoj.org/staff/ichi/MCSRED/mcsred.html

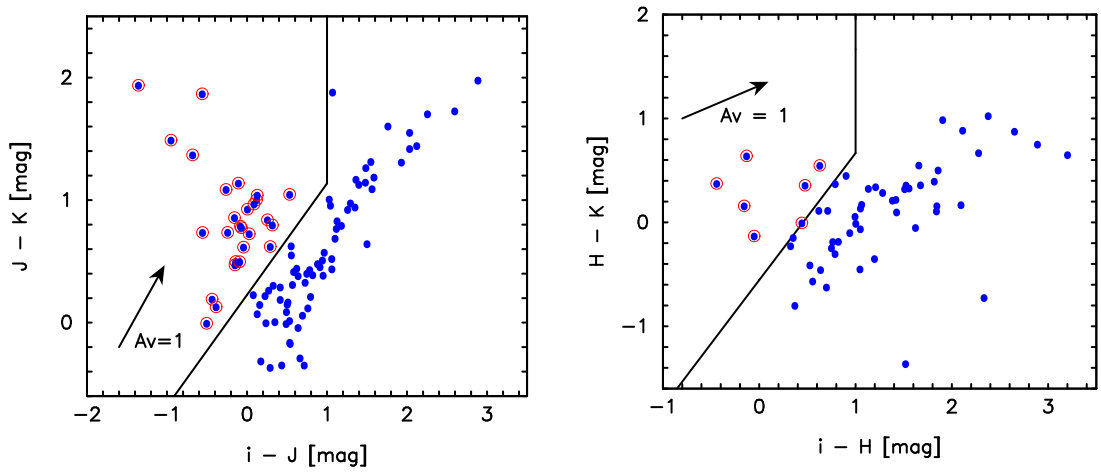

Figure 4.1: Color–color diagrams for NB2095 (left) and NB2315 (right). Blue filled circles represent the NB emitters selected based on the color–magnitude diagrams, and red circles show the [OIII] emitters at $z = 3.18$ (left) and $z = 3.63$ (right), which satisfy the criteria shown by the dividing solid lines. The arrow represents the reddening vector of $A_V = 1$ mag.

based on the stellar population synthesis model of Kodama et al. (1998, 1999). Also, a dust-extinction-uncorrected $SFR_{[OIII]}$ is calculated from each NB magnitude. Figure 4.2 shows that our EW cut is located well below the actual observed data points, and our galaxy sample is not biased to any particular galaxies in the stellar mass–SFR diagram.

4.1.2 AGN contribution

In the first place, we verify the presence of AGN candidates in our sample of [OIII] emitters. We use the `EAZY` code to obtain the rest-frame U, V, and J-band magnitudes for our sample. Note that the derived photometric redshifts are mostly consistent with the expected redshifts, $z = 3.18$ and 3.63. The rest-frame $(U - V)$ and $(V - J)$ colors allow us to distinguish between two galaxy populations, namely, old quiescent galaxies and young, dusty star-forming galaxies, by capturing the Balmer/4000 Å breaks between U and V bands (e.g. Wuyts et al. 2007; Williams et al. 2009; Whitaker et al. 2011). Figure 4.3 shows the rest-frame UVJ color–color diagram of our [OIII] emitters. We find that one object is marginally classified as a quiescent galaxy, indicating that its [OIII] emission is likely to be dominated by the AGN activity rather than the star formation. For all

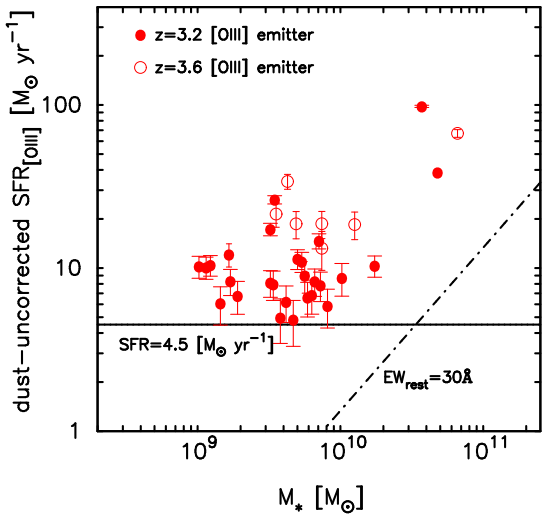

Figure 4.2: Stellar mass versus SFR diagram of the [OIII] emitters *before dust extinction correction is applied* to discuss any possible selection bias. The filled and open circles represent the [OIII] emitters at $z = 3.2$ (NB2095) and $z = 3.6$ (NB2315), respectively. SFRs are derived from [OIII] line luminosities without dust extinction correction here on purpose. The horizontal solid line and the dot-dashed line correspond to our selection criteria of the NB emitters, namely, $\Sigma > 3$ and $HK - \mathrm{NB} = 0.4$, respectively. These numbers correspond to our detection limits of $\mathrm{SFR}_{[\mathrm{OIII}]} = 4.5\ \mathrm{M}_{\odot}\mathrm{yr}^{-1}$ and $\mathrm{EW}_{\mathrm{rest}} = 30$ Å, respectively.

the other emitters classified as star-forming galaxies, we cannot discriminate between the contribution from AGNs and that from star-forming regions.

For further investigation, we inspect the X-ray image from *XMM-Newton* (Ueda et al., 2008). None of our [OIII] emitters are detected in X-ray, and thus our sample does not seem to contain any bright obvious AGNs. We also look into *Spitzer*/MIPS 24μm catalog and find that three sources are detected with MIPS. A fraction of them might be obscured AGNs with warm dust components that emit strong IR emission.

Spectroscopic observations are necessary to confirm the presence of AGNs in our sample, and we do not exclude these sources in the following analysis.

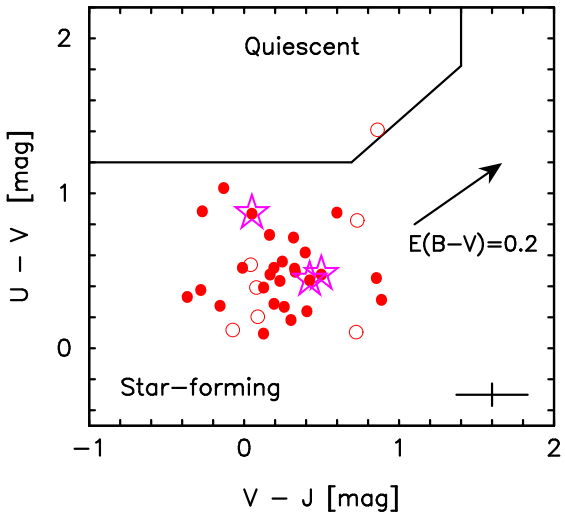

Figure 4.3: Rest-frame UVJ diagram of our [OIII] emitters (filled circles for $z = 3.2$ and open circles for $z = 3.6$). Star symbols indicate the MIPS-detected sources. The arrow shows a reddening vector of $E(B-V) = 0.2$. The typical errors of the $(U-V)$ and $(V-J)$ colors are shown at the bottom right corner of the figure. We make 1000 pseudo-photometric catalogs for each object by randomly generating fluxes in each band from a Gaussian distribution with the standard deviation determined by each flux error. These generated SEDs are fitted by the `EAZY`, and the dispersions of the two colors are estimated for each object. We show those dispersions as the typical error of each color.

4.1.3 Estimation of physical quantities

We perform the SED fitting for our [OIII] emitters using the `FAST` code. In the SXDF-UDS-CANDELS field, the photometric catalog is publicly available at the Rainbow Database[2] (Galametz et al., 2013). We use 18 photometric band data, u, B, V, R_c, i', z', $F606W$, $F814W$, $F125W$, $F160W$, Y, J, H, K_s, 3.6, 4.5, 5.8, and 8.0 μm. For the NB2095-selected [OIII] emitters, emission line fluxes are subtracted from the Ks-band fluxes before the SED fitting is performed, while no correction is required for the NB2315-selected ones as the NB2315 has little overlap with the Ks-band in wavelength. The redshifts of the NB2095- and NB2315-selected [OIII] emitters are fixed to $z = 3.18$ and 3.63, respectively, for the

[2]https://arcoiris.ucolick.org/Rainbow_navigator_public/

SED fitting. We use the population synthesis model of Bruzual & Charlot (2003), the Salpeter IMF (Salpeter, 1955), and the dust extinction law of Calzetti et al. (2000). We assume the exponentially declining SFH with $\log(\tau/\mathrm{yr}) = 7.0$–$10.0$ in steps of 0.5, and the solar metallicity. We assume the cosmological parameters of $\Omega_\mathrm{m} = 0.27$, $\Omega_\Lambda = 0.73$, and $H_0 = 71$ [km s^{-1} Mpc^{-1}] here. In the following analyses, we use the stellar masses and dust extinctions (A_V) estimated by the SED fitting.

We estimate SFRs of the [OIII] emitters with two different indicators, the UV continuum luminosities (tracing hot and young stars) and the [OIII] emission line luminosities (tracing regions ionized by hot, young and massive stars). In the former case, we estimate $\mathrm{SFR_{UV}}$ in the same manner as described in Section 3.1.5 The UV luminosity is derived from R_c-band magnitude ($\lambda_\mathrm{c} = 6498.1$ Å), and the dust extinction at 1600 Å is estimated by converting A_V to $A(1600\ \text{Å})$ assuming the Calzetti extinction law (Calzetti et al., 2000).

In Maschietto et al. (2008), they derived an SFR from an [OIII] emission line strength by assuming an [OIII]/Hα ratio of 2.4, which is the maximum value for local star-forming galaxies (Moustakas et al., 2006). Considering the fact that star-forming galaxies at high redshifts tend to show higher [OIII]/Hβ ratios (e.g. Steidel et al. 2014; Shimakawa et al. 2015; Holden et al. 2016), this assumption seems to be reasonable, although the [OIII]/Hα ratio has a large dispersion among different galaxies (Moustakas et al., 2006; Shimakawa et al., 2015). We adopt this maximum ratio to the relation between the SFR and Hα luminosity (Eq. 3.4; Kennicutt 1998b). Then, the lower limit of $\mathrm{SFR_{[OIII]}}$ is obtained by:

$$\mathrm{SFR_{[OIII]}}(\mathrm{M_\odot yr^{-1}}) > 0.33 \times 10^{-41} \frac{L_\mathrm{[OIII]}}{\mathrm{erg\ s^{-1}}}. \tag{4.1}$$

The dust extinction at 5007 Å is estimated in the same manner as used for the dust extinction at 1600 Å based on the SED fitting. We assume that there is no extra extinction for the nebula emission compared to the stellar extinction as mentioned in Section 3.1.5.

In Figure 4.4, we compare SFRs derived from the two different indicators. The ratios of $\mathrm{SFR_{[OIII]}/SFR_{UV}}$ range from 0.25 to 3 for most of the sources. On the other hand, the source classified as a quiescent galaxy on the UVJ diagram (Figure 4.3) shows a higher ratio of $\mathrm{SFR_{[OIII]}/SFR_{UV}} \sim 5.3$. It suggests that this source has an extra contribution from an AGN to its [OIII] emission, as expected in Section 4.1.2.

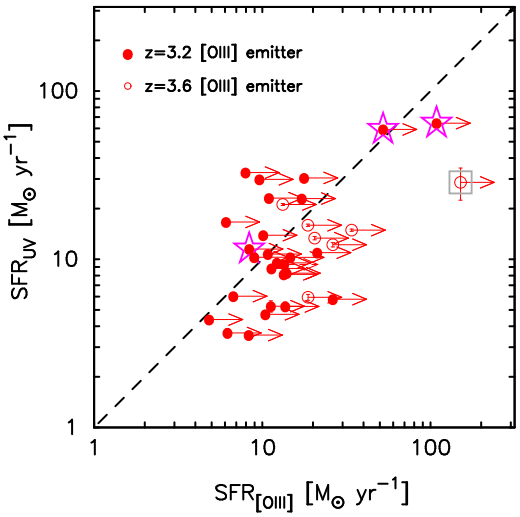

Figure 4.4: Comparison between the dust-extinction-corrected $\mathrm{SFR}_{[\mathrm{OIII}]}$ and $\mathrm{SFR}_{\mathrm{UV}}$ (filled circles for $z = 3.2$ and open circles for $z = 3.6$). Arrows represent that $\mathrm{SFR}_{[\mathrm{OIII}]}$ is shown as the lower limit. Star symbols show the MIPS-detected sources, and a square indicates a source classified as a quiescent galaxy based on the rest-frame UVJ diagram (Figure 4.3). The dashed line represents the case where two measurements are identical.

4.2 Extended sample of [OIII] emitters at $z > 3$

In order to obtain a larger sample of [OIII] emitters at $z > 3$, here we introduce another sample of [OIII] emitters at $z = 3.24$ (NB_K) in the COSMOS field obtained by HiZELS (Sobral et al., 2013). We also introduce [OIII] emitters at $z = 2.23$ (NB_H) from HiZELS as a sample for comparison (Section 4.3 and 4.4).

We match the original catalog of NB_K and NB_H emitters of Sobral et al. (2013) with the latest public photometric catalog in the COSMOS field (COSMOS2015; Laigle et al. 2016) with a searching radius of $0''.6$. We use only the emitters with a counterpart in the COSMOS2015 catalog. The selection criteria of the NB emitters are $\Sigma > 3$ and $\mathrm{EW}_{\mathrm{rest}} = 25$Å, same as shown in Section 3.1.1. We select [OIII] emitter candidates at $z = 3.24$ and 2.23 using the photometric redshifts given in the COSMOS2015, and the applied ranges are $2.8 < z_{\mathrm{photo}} < 4.0$ for the $z = 3.24$ [OIII] emitters and $1.7 < z_{\mathrm{photo}} < 2.8$ for the $z = 2.23$ [OIII] emitters. For the emitters which do not have the photometric redshifts, we apply the color–color selections as shown in Khostovan et al. (2015). As a

result, we obtain 174 [OIII] emitters at $z = 3.24$ and 117 [OIII] emitters at $z = 2.23$.

The stellar masses of the [OIII] emitters are estimated by the SED fitting as done in Section 4.1.3. We use 14 photometric bands data; u, B, V, r, i', z'', Y, J, H, K_s, 3.6, 4.5, 5.8, and 8.0 μm from the COSMOS2015 catalog. The emission line fluxes are subtracted from the K_s-band and/or H-band fluxes before the SED fitting. We use the `EAZY` and the `FAST` codes for the SED fitting. The redshifts are fixed to $z = 3.24$ and 2.23. We use the population synthesis model of Bruzual & Charlot (2003) with the Chabrier IMF [3] (Chabrier, 2003), and the dust extinction law of Calzetti et al. (2000). We assume the exponentially declining SFH with $\log(\tau/\mathrm{yr}) = 8.5$–$11.0$ in steps of 0.1, and the metallicities of $Z = 0.004, 0.008$, and 0.02 (solar) for $z = 3.24$ emitters and $Z = 0.004, 0.008, 0.02$ and 0.04 for $z = 2.23$ emitters. We note that the setting of the SED fitting is slightly different between the two samples of the Mahalo-Subaru and HiZELS. Although the different settings of the SED fitting (except for the IMF) are unlikely to affect the stellar mass estimation of the targets, we do not compare the two sample directly in the following analyses.

We estimate SFRs of the HiZELS [OIII] emitters from the UV continuum luminosities. $\mathrm{SFR_{UV}}$ is estimated from the r-band ($\lambda_\mathrm{c} = 6288.7$ Å) magnitude and V-band ($\lambda_\mathrm{c} = 5477.8$ Å) magnitude using the Eq. 3.3 for $z = 3.24$ and 2.23 emitters, respectively. The dust extinction A_FUV is estimated from the UV slope β with Eq. 3.1. The UV slope β is derived by fitting a linear function to the four broad-band photometries at the rest-frame wavelength of 1600–2800 Å, i.e. r, i', z'', and Y-band and V, r, i', and z''-band for $z = 3.24$ and 2.23 emitters, respectively.

When we compare the [OIII] emitters at $z = 3.24$ and 2.23 in the following sections, we consider the different depth of NB data between NB_H and NB_K, i.e. the different luminosity limit of the [OIII] emission line. We take into account the redshift evolution of L_* of the luminosity function of [OIII] emitters from Khostovan et al. (2015), and then we set the $L_{[\mathrm{OIII}]}$ limit for the [OIII] emitters at $z = 2.23$. The comparisons between the [OIII] emitters at $z = 3.24$ and 2.23 are fair in terms of the $L_{[\mathrm{OIII}]}$, although our results are not largely changed even when we do not apply such a luminosity cut.

[3] Stellar masses and SFRs estimated assuming the Chabrier IMF are scaled to the values for the Salpeter IMF by multiplying a factor of 1.7 (Pozzetti et al., 2007).

4.3 Mass–SFR relation

We investigate the relation between stellar masses and SFRs (the "main sequence" of star-forming galaxies) of the two samples of [OIII] emitters at $z > 3$ separately.

Figure 4.5 shows the M_*–SFR relation of the [OIII] emitters at $z = 3.2,\ 3.6$, together with that of the Hα emitters at $z = 2.2,\ 2.5$ in the same field (Tadaki et al., 2013). We re-estimate stellar masses and $\mathrm{SFR_{UV}}$ of the Hα emitters in the same manner as described in Section 4.1.3. Figure 4.6 also shows the M_*–SFR relation of the HiZELS [OIII] emitters at $z = 3.24$ together with that of the [OIII] emitters at $z = 2.23$ in the same field.

We find that stellar masses and SFRs of the [OIII] emitters show a clear correlation, as seen in other studies of star-forming galaxies across a wide redshift range (e.g. Daddi et al. 2007; Whitaker et al. 2012; Kashino et al. 2013; Koyama et al. 2013; Tasca et al. 2015; Tomczak et al. 2016). The normalization of the M_*–SFR relation of the [OIII] emitters at $z > 3$ is almost identical to that of the star-forming galaxies at $z \sim 2.2,\ 2.5$. With the emitter samples from Mahalo-Subaru, we confirm that the best fit-line to the [OIII] emitters is consistent with the fit to the Hα emitters within 1σ errors in both the slopes and the intercepts. Importantly, however, the distributions of galaxies along the main sequence are systematically different in the sense that the stellar masses of the [OIII] emitters at $z > 3$ tend to be lower than those of the star-forming galaxies at $z \sim 2.2,\ 2.5$. The lack of the massive galaxies of $\log(\mathrm{M_*/M_\odot}) \gtrsim 10.0$ at $z > 3$ is clearly seen in the both figures. We can simply interpret that the offset of the stellar mass between the star-forming galaxies at $z > 3$ and those at $z \sim 2$ is due to the evolution of galaxies since $z > 3$ towards $z \sim 2$. We will discuss this more in Chapter 6.

4.4 Specific SFR and dust extinction as a function of stellar mass

We also investigate the specific SFR ($\mathrm{sSFR_{UV}}$) and dust extinction A_{FUV} as a function of stellar masses for the [OIII] emitters at $z = 3.24$ and 2.23 obtained by HiZELS.

Figure 4.7 shows the M_*–$\mathrm{sSFR_{UV}}$ relation of the two samples at different redshifts. The $\mathrm{sSFR_{UV}}$ shows the anti-correlation with respect to the stellar mass as indicated from the sub-linear star-forming main sequence. Although the [OIII] emitters at $z = 3.24$ and

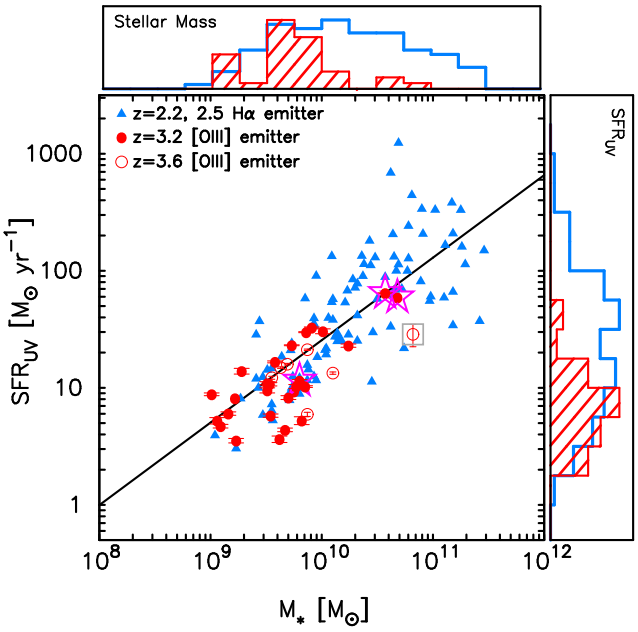

Figure 4.5: Stellar mass and SFR relation of the [OIII] emitters from Mahalo-Subaru (filled circles for $z = 3.2$ and open circles for $z = 3.6$). The Hα emitters at $z = 2.2$ and 2.5 from Tadaki et al. (2013) are also shown with the filled triangles. SFRs are derived from UV luminosities and corrected for dust extinction. Errors in SFRs for the [OIII] emitters are estimated from 1σ photometric errors of the R_c-band magnitudes. The solid line represents the best-fit line to the Hα emitters: $\mathrm{SFR_{UV}} = 120 M_{11}^{0.705}$ ($M_{11} = M_*/10^{11} M_\odot$). The histograms in the top and right panels show the stellar mass and SFR distributions of the [OIII] emitters at $z = 3.2$, 3.6 (red hatched histograms) and those of the Hα emitters at $z = 2.2$, 2.5 (blue open histograms) with an arbitrary scale.

those at $z = 2.23$ again share the same relation, their distributions along the relation are offset in the sense that the former tend to have lower stellar masses and thus higher $\mathrm{sSFR_{UV}}$ than the latter.

Figure 4.8 shows the M_*–A_{FUV} relation of the [OIII] emitters at different redshifts. Although the scatter is relatively large, the stellar mass and the dust extinction show a positive correlation, i.e. more massive galaxies are dustier (Garn & Best, 2010). Such relation is consistent between the [OIII] emitters at $z = 3.24$ and those at $z = 2.23$ for low mass objects. For massive galaxies with $\log(\mathrm{M}*/\mathrm{M}_\odot) \gtrsim 10.0$, we may see an offset in A_{FUV} between the two samples, which we will discuss more below.

Since the specific SFR and dust extinction are correlated with the stellar mass, we

compare the number distributions of $\mathrm{sSFR_{UV}}$ and A_{FUV} between the [OIII] emitters at $z = 3.24$ and those at $z = 2.23$ by dividing them into stellar mass bins in order to compare the $\mathrm{sSFR_{UV}}$ and A_{FUV} distributions among the galaxies with similar stellar masses at different redshifts. We divide the samples into the three bins of $\log(\mathrm{M_*/M_\odot}) < 9.65$, $9.65 \leq \log(\mathrm{M_*/M_\odot}) < 10.3$, and $\log(\mathrm{M_*/M_\odot}) \geq 10.3$, so that the three subsamples at $z = 2.2$ have a similar number of galaxies. Figure 4.9 shows the histograms of $\mathrm{sSFR_{UV}}$ and A_{FUV} of the [OIII] emitters at different redshifts.

In Figure 4.9, comparing the [OIII] emitters at $z = 3.24$ with those at $z = 2.23$ at the fixed stellar mass range, the difference of the distribution of $\mathrm{sSFR_{UV}}$ or A_{FUV} is seen in the highest stellar mass bin ($\log(\mathrm{M_*/M_\odot}) \geq 10.3$). The fraction of the massive galaxies with high $\mathrm{sSFR_{UV}}$ or high A_{FUV} is significantly higher at $z = 2.23$ than $z = 3.24$. This is also seen from a comparison of the median values of $\mathrm{sSFR_{UV}}$ and A_{FUV} as shown by the arrows in Figure 4.9. This is not the case for the two lower stellar mass bins of $\log(\mathrm{M_*/M_\odot}) < 9.65$ and $9.65 \leq \log(\mathrm{M_*/M_\odot}) < 10.3$, where the two samples have more or less the same distributions. This indicates that the massive star-forming galaxies ($\log(\mathrm{M_*/M_\odot}) \geq 10.3$) become more active and dusty since $z > 3$ towards $z \sim 2$, while the less massive galaxies have similar modes of star formation and dust contents between the two epochs.

4.5 Size of the [OIII] emitters

NB imaging survey areas at the SXDF are covered by the *HST* CANDELS field, and high spatial resolution images in the rest-frame UV–optical wavebands (Advanced Camera for Surveys (ACS) and WFC3) are available for the Mahalo-Subaru [OIII] emitters at $z = 3.2, 3.6$. We use the structural parameters measured by van der Wel et al. (2012) on the H_{F160W}-band-selected sources in CANDELS. We briefly summarize below their methods to obtain the structural parameters.

They performed a Sérsic model fit to the H_{F160W}-band-selected sources using the `GALAPAGOS` (Barden et al., 2012) and `GALFIT` (Peng et al., 2010). The parameters that were used for the fit are the total magnitude, half-light radius measured along the major axis, Sérsic index, axial ratio, position angle, and central position. The initial guess of these parameters are given by `SExtractor`. The best-fit `GALFIT` parameters for all the objects

are publicly available in the Rainbow Database (Galametz et al., 2013). A flag number between 0 and 3 is assigned for each source. We reject sources with flag ≥ 2 because the fitting result with a Sérsic model becomes increasingly unreliable. They note that resultant structural parameters have systematic and random uncertainties and that such uncertainties depend on the brightness of objects and become larger for fainter sources. At $H_{F160W} = 25$ mag, systematic and random uncertainties of the half-right radius (r_e in arcsec) are $0''.04$ and $0''.18$, respectively, when r_e is less than $0''.3$, while they are $-0''.09$ and $0''.33$ when r_e is greater than $0''.3$. At $H_{F160W} = 26$ mag, those uncertainties become as large as $0''.12/0''.42$ ($r_e < 0''.3$) and $-0''.11/0''.63$ ($r_e > 0''.3$), respectively.

Using the `GALFIT` parameters from van der Wel et al. (2012), we estimate the effective radius r_e [kpc] in the rest-frame U-band for the [OIII] emitters. We use only the bright sources ($H_{F160W} < 25$ mag) with flag values of 0 or 1. Based on the magnitude cut and the flag values, 10 and 9 sources, respectively, are excluded from our sample.

4.5.1 Mass–size relation

Figure 4.10 shows the relation between stellar masses and sizes of the [OIII] emitters at $z = 3.2, 3.6$. The Hα emitters at $z = 2.2, 2.5$ are also shown. Their sizes are estimated in the *HST* J_{F125W}-band images so that they can be directly compared to those of our [OIII] emitters at the same rest-frame wavelength. The size measurements are also limited to the bright objects ($J_{F125W} < 25$ mag) with flag = 0 or 1. In Figure 4.10, the solid and dashed lines represent the mass–size relations of late- and early-type galaxies at $2.5 < z_{\rm photo} < 3.0$, respectively, derived from the 3D-*HST*/CANDELS data (van der Wel et al., 2014). We find that the size distribution of the [OIII] emitters with respect to the stellar mass is similar to that of the Hα emitters, and that they follow the mass–size relation of late-type galaxies at $z \sim 2.75$ from van der Wel et al. (2014). In van der Wel et al. (2014), galaxy sizes are estimated at a rest-frame wavelength of 5000 Å, slightly longer than in the rest-frame U-band, where our galaxy sizes are measured. To verify a possible effect due to wavelength mismatch, we also apply their correction method to our sample, and we confirm that there is no systematic difference between the two measurements at different wavelengths.

While most of the [OIII] emitters have sizes consistent with the mass–size relation of late-type galaxies at $z \sim 2.75$, there is a massive [OIII] emitter for its size ($M_* \sim 3{\times}10^{10}{\rm M}_\odot$

and $r_e \sim 1$ kpc). Massive and compact star-forming galaxies are expected to evolve to massive and compact quiescent galaxies when their star formation is quenched (e.g. Barro et al. 2013; Tadaki et al. 2014). We confirm the presence of such massive and compact star-forming galaxies at $z = 3.2$.

4.6 Summary of this chapter

In this chapter, we use the two sets of samples of the [OIII] emitters at $z > 3$; one from Mahalo-Subaru project and the other from HiZELS survey. In the SXDF-UDS-CANDELS field, we obtain 27 and 7 [OIII] emitters at $z = 3.2$ and 3.6 by Mahalo-Subaru. Although we find that some sources in the sample might be contaminated by AGNs, we do not exclude these objects here because the spectroscopic observation is necessary to confirm the presence of AGNs. In the COSMOS field, there are 174 [OIII] emitters at $z = 3.24$ obtained by HiZELS. We investigate the star-forming activity and the sizes of the [OIII] emitters at $z > 3$, and compare them with the star-forming galaxies at $z \sim 2$ (either Hα or [OIII] emission line galaxies). We have found the following things:

- The stellar mass and the dust-extinction-corrected $\mathrm{SFR_{UV}}$ of the [OIII] emitters show a clear correlation, as seen in other previous studies over a wide redshift range. Comparing the [OIII] emitters at $z = 3.2,\ 3.6$ with the star-forming galaxies at $z = 2.2,\ 2.5$, we find that the normalization of the M_*–SFR relation of $z > 3$ star-forming galaxies is almost the same that of the $z \sim 2$ star-forming galaxies. This is confirmed for both the samples of the [OIII] emitters at $z > 3$ obtained by Mahalo-Subaru and HiZELS, and the location of the M_*–SFR relation of the two samples ($z > 3$) is consistent with each other.

- Although the location of the M_*–SFR relation is almost the same between the star-forming galaxies at $z > 3$ and those at $z \sim 2$, the distributions of galaxies along the relation are different in the sense that the [OIII] emitters at $z > 3$ tend to have lower stellar masses as compared to star-forming galaxies at $z \sim 2$.

- For the samples obtained by HiZELS, we investigate the relations between the stellar mass and the $\mathrm{sSFR_{UV}}$, and between the stellar mass and the A_{FUV}. The $\mathrm{sSFR_{UV}}$ decreases with the stellar mass, as expected from the sub-linear slope of the star-

forming main sequence. Although the scatter is slightly large, the stellar mass and the dust extinction show a positive correlation, i.e. the massive galaxies are dustier. When we compare the number distribution of $\mathrm{sSFR_{UV}}$ and A_{FUV} between the [OIII] emitters at $z = 3.24$ and those at $z = 2.23$ in three stellar mass ranges, the difference in the number distribution is seen at the highest stellar mass bin of $\log(\mathrm{M_*/M_\odot}) \geq 10.3$. It is suggested that the star-forming galaxies with higher sSFR and stronger dust extinction are more common at $z \sim 2$.

- For the samples obtained by Mahalo-Subaru, the *HST*/WFC3 images are available (van der Wel et al., 2012), and we investigate the sizes of the [OIII] emitters at $z = 3.2$, 3.6. The size distribution of the [OIII] emitters at $z = 3.2, 3.6$ with respect to the stellar mass is similar to that of the Hα emitters at $z = 2.2, 2.5$ and to that of the late-type galaxies at $z \sim 2.75$ from van der Wel et al. (2014). The size evolution of the star-forming galaxies is not so strong from $z > 3$ towards $z \sim 2$. While most of the [OIII] emitters have consistent sizes with those expected from the mass–size relation of star-forming galaxies, one [OIII] emitter at $z = 3.2$ is massive and compact, which is comparable to what is called the "blue nugget" (Barro et al., 2013).

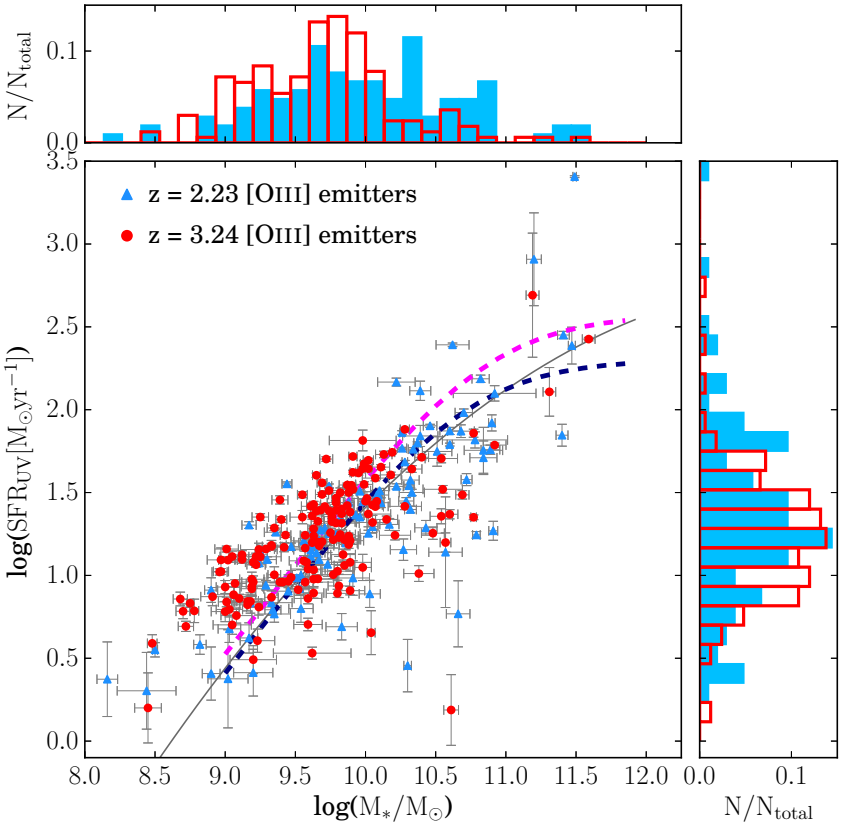

Figure 4.6: Stellar mass and SFR (SFR_{UV}) relation of the [OIII] emitters at $z = 3.24$ from HiZELS (red circles) compared to those of the [OIII] emitters at $z = 2.23$ in the same field (blue triangles). SFRs are derived from UV luminosities and corrected for dust extinction. The thick dashed lines show the stellar mass–SFR relation at $z = 3.2$ (magenta line) and $z = 2.2$ (navy line) from Tomczak et al. (2016). The solid lines shows the stellar mass–SFR relation at $z \sim 2.5$ from Whitaker et al. (2012). The histograms on the top and right panels show the stellar mass and SFR_{UV} distributions, respectively, of the [OIII] emitters at $z = 3.24$ (red open histograms) and 2.23 (blue filled histograms). In this plot, we apply the Chabrier IMF.

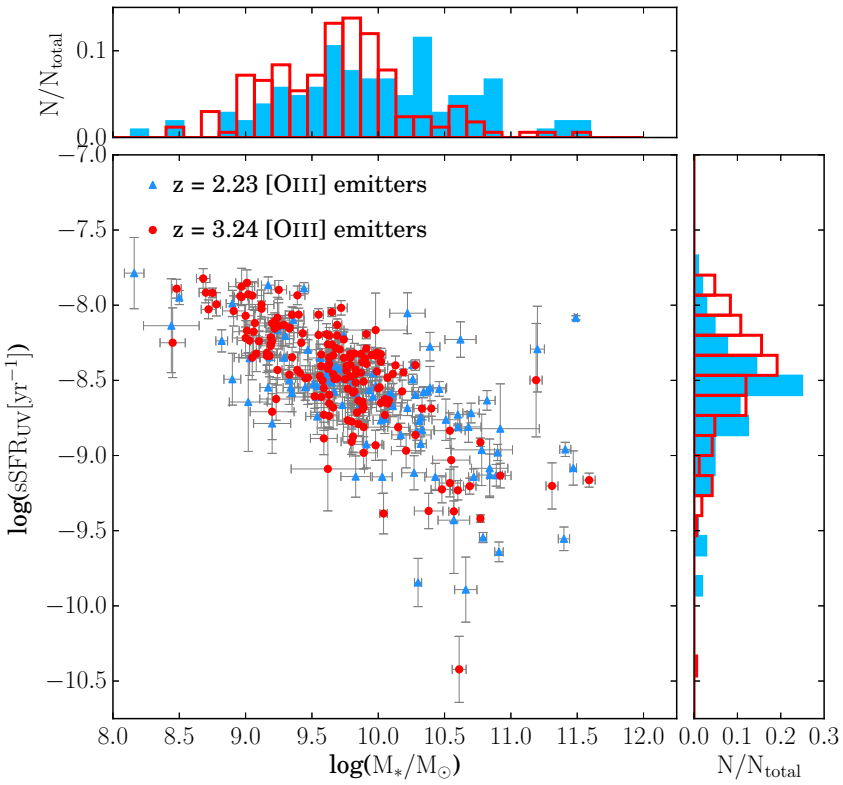

Figure 4.7: Stellar mass and specific SFR ($sSFR_{UV}$) relation of the [OIII] emitters at $z = 3.24$ from HiZELS (red circles) together with that of the [OIII] emitters at $z = 2.23$ in the same field (blue triangles). The histograms in the top and right panels show the stellar mass and sSFR distributions of the [OIII] emitters at $z = 3.24$ (red open histogram) and 2.23 (blue filled histograms). In this plot, we apply the Chabrier IMF.

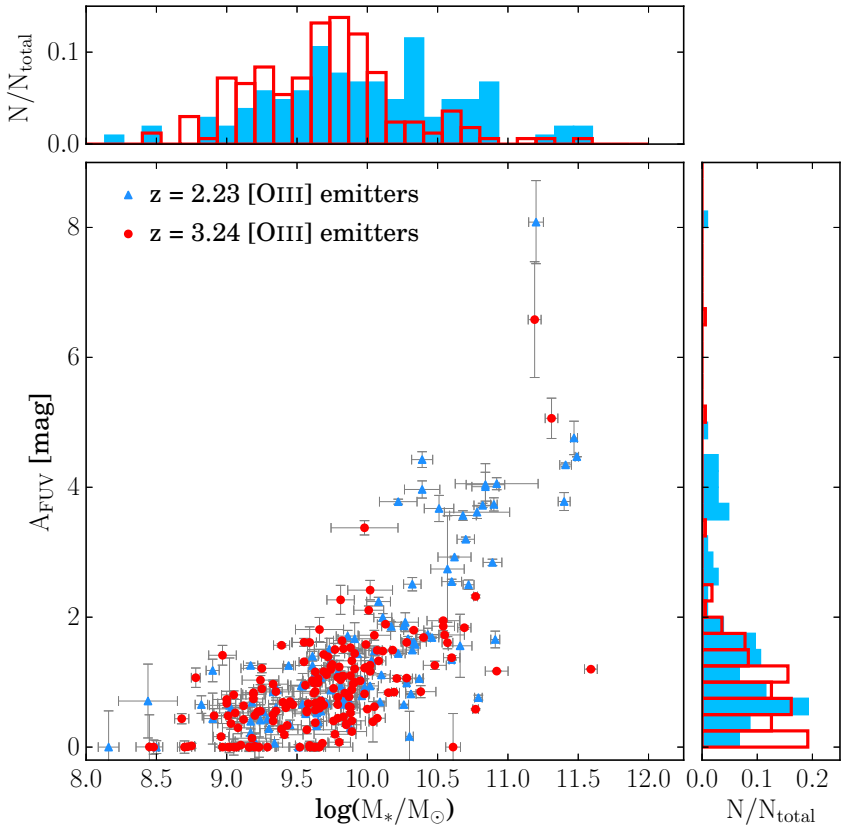

Figure 4.8: The relation between stellar mass and the amount of dust extinction, $A_{\rm FUV}$, of the [OIII] emitters at $z = 3.24$ from HiZELS (red circles) compared to that of the [OIII] emitters at $z = 2.23$ in the same field (blue triangles). The histograms in the top and right panels show the stellar mass and $A_{\rm FUV}$ distributions of the [OIII] emitters at $z = 3.24$ (red open histogram) and 2.23 (blue filled histograms). In this plot, we apply the Chabrier IMF.

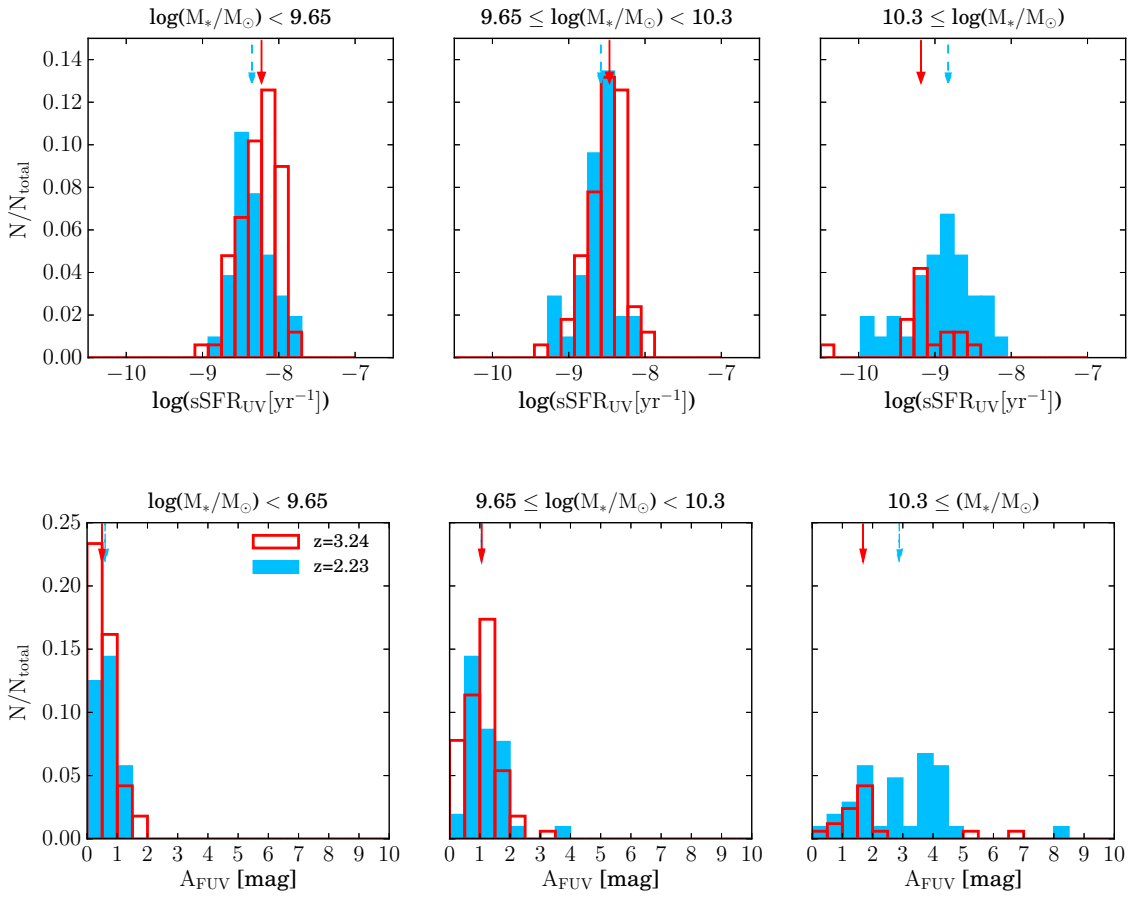

Figure 4.9: Comparison of the number distribution of $\mathrm{sSFR_{UV}}$ (top three panels) and A_{FUV} (bottom three panels) between the [OIII] emitters at $z = 3.24$ (red open histograms) and those at $z = 2.23$ (blue filled histograms). The sources are divided into three subsamples according to their stellar masses, namely, $\log(\mathrm{M_*/M_\odot}) < 9.65$, $9.65 \leq \log(\mathrm{M_*/M_\odot}) < 10.3$, and $10.3 \leq \log(\mathrm{M_*/M_\odot})$. The solid and dashed arrows in each panel represent the median values of $\mathrm{sSFR_{UV}}$ or A_{FUV} of the [OIII] emitters at $z = 3.24$ and 2.23, respectively.

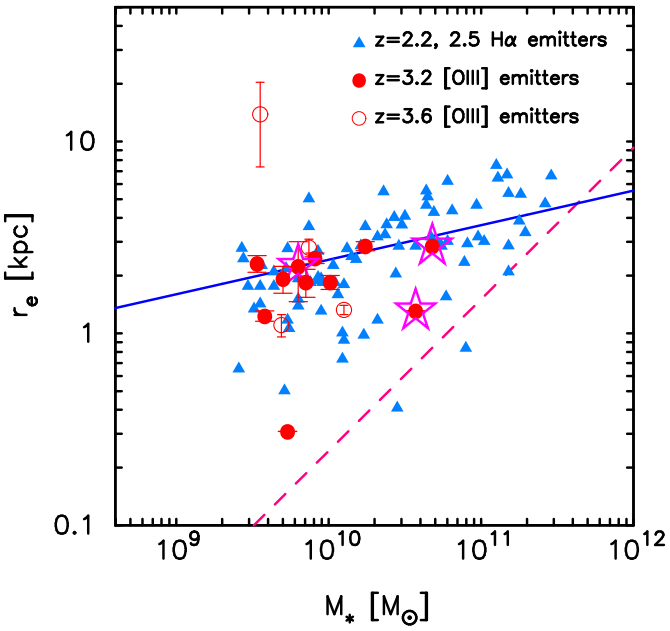

Figure 4.10: Stellar mass and size relation of the Mahalo-Subaru [OIII] emitters (filled circles for $z = 3.2$ and open circles for $z = 3.6$) with $H_{F160W} < 25$ mag. The Hα emitters at $z = 2.2, 2.5$ (Tadaki et al., 2013) with $J_{F125W} < 25$ mag are also shown with the filled triangles. The solid and dashed lines represent the mass–size relations of $z \sim 2.75$ late-type and early-type galaxies, respectively (van der Wel et al., 2014). Note that the galaxy sizes in van der Wel et al. (2014) are estimated at a rest-frame wavelength of 5000 Å, slightly longer than in the rest-frame U-band, where our galaxy sizes are measured.

5 Spectroscopic view of [Oiii] emitters at $z > 3$

In this chapter, we present some results obtained from the spectroscopic observation of the [Oiii] emitters at $z = 3.24$ in the COSMOS field. We carried out a NIR spectroscopy of the [Oiii] emitters with Keck/MOSFIRE. With the obtained spectra in H and K-bands, we discuss the physical conditions of the [Oiii] emitters at $z > 3$ such as their ionization states and gaseous metallicities.

5.1 Targets, observation and data analyses

Our spectroscopic targets are selected from the NB_K emitter catalog in the COSMOS field from HiZELS (see Section 4.2 for more details). We were awarded a half night on the Keck-I telescope with the Multi-Object Spectrometer For Infra-Red Exploration (MOSFIRE; McLean et al. 2010, 2012) as a Subaru-Keck time exchange program (S16A-058; Suzuki, T. et al.). The observation was carried out on 27th March 2016. Our primary targets are ten [Oiii] emitters (candidates) at $z = 3.24$. We also include bright photo-z sources at $3.0 < z_{\rm photo} < 3.5$ as the secondary targets in the same mask. We obtained their spectra in K and H-bands in order to detect the major emission lines, such as [Oiii]$\lambda\lambda$5007,4959, Hβ, and [Oii]$\lambda\lambda$3726,3729. The total integration time was 120 min and 90 min for K and H-band, respectively. The seeing size (FWHM) was $0''.7$–$1''.0$.

The obtained raw spectra were reduced using the MOSFIRE Data Reduction Pipeline[1] (`MosfireDRP`), which is described in more detail in Steidel et al. (2014). The pipeline follows the standard data reduction procedures: flat-fielding, wavelength calibration, sky subtraction, rectification, and combining the individual frames. Finally we obtain the rectified two-dimensional (2D) spectra. One-dimensional (1D) spectra are extracted from

[1] `https://keck-datareductionpipelines.github.io/MosfireDRP/`

the 2D spectra with $1''.3$–$1''.8$ diameter aperture in order to maximize the signal-to-noise (S/N) ratio. The telluric correction and flux calibration were carried out by using a standard A0V star, HIP43018, which were taken at the same night.

All of the ten [OIII] emitter candidates clearly show the [OIII] doublet lines in the K-band, and are identified as the [OIII] emitters at $z \sim 3.24$. The Hβ and [OII] emission lines are also visually identified in the 1D spectra in the K- and H-band, respectively, for all of the [OIII] emitters. In order to measure the emission line fluxes, we perform the Gaussian fitting for the emission lines using the `SPECFIT` [2] (Kriss, 1994) in `STSDAS` of the `IRAF` environment. At first, we fit the [OIII] doublet and Hβ with a Gaussian by assuming a common velocity dispersion. The [OIII] doublet lines are fitted by assuming the line ratio [OIII]λ5007/[OIII]λ4959 of 3.0 (Storey & Zeippen, 2000). The redshifts of the [OIII] emitters are determined using the [OIII]λ5007 line using the vacuum wavelength (5008.24 Å). The redshift distribution of the [OIII] emitters are shown in Figure 5.1. Then, the [OII] doublet lines are fitted assuming the determined redshifts and velocity dispersions. We also fit the relatively weak lines, such as HeIIλ4686 and [NeIII]λ3868, by assuming the determined redshifts and velocity dispersions.

We included a monitoring star in our mask so that we can use it for the flux calibration between the H and K-band. By comparing the observed fluxes of the star with the 2MASS magnitudes, we determine the correction factors for H and K-band. Here we do not care much about the slit loss problem, but we consider that we have already roughly corrected for the slit loss by the flux calibration using the standard star. Note that this is accurate only if the sources are well approximated by the point sources.

In Figure 5.2, we show the reduced spectra in H and K-bands for the ten [OIII] emitters. The high spectral resolution of MOSFIRE, $R \sim 3600$, allows us to separate the emission lines clearly from the series of OH skylines. For all of the [OIII] emitters, the [OIII]λ5007 lines are detected with very high S/N ratios, S/N > 20.0. The Hβ line is also detected for all the emitters at mote than 3σ significance levels. Although there are some cases of the [OII] doublet lines are affected by the OH skylines, the summed flux of the doublet lines is detected at more than 3σ levels for all the emitters. As for the [NeIII] emission line, it is detected from the six emitters at more than 3σ significance levels. HeII line is not detected at S/N > 3 for any of the [OIII] emitters.

[2] `http://stsdas.stsci.edu/cgi-bin/gethelp.cgi?specfit`

The velocity dispersions obtained by the emission line fitting for each object have the values of 140–300 kms^{-1}. From the fact that there is no Hβ emission line with very wide line width, such as more than 1000 kms^{-1}, there is no obvious AGN in the observed [OIII] emitters. We also note that none of our sample is detected at X-ray with *Chandra* (Civano et al., 2016).

The redshift distribution of the [OIII] emitters is shown in Figure 5.1. We find that three emitters are located at slightly higher redshifts than the redshift range expected for the [OIII]λ5007 line with the NB$_K$ filter. In Figure 5.1, we show the transmission curves of the NB$_K$ filter as a function of redshift in the two cases; one for the [OIII]λ5007 line (vacuum wavelength: 5008.24 Å) and the other for the [OIII]λ4959 line (vacuum wavelength: 4960.30 Å). The three [OIII] emitters at slightly higher redshifts turn out to be detected by their strong [OIII]λ4959 with the NB$_K$ filter actually. The fraction of the [OIII]λ4959 emitters is $\sim$ 30 %, and this is consistent with our estimation from the luminosity function in Section 3.1.4 and the result of the spectroscopy of [OIII]+Hβ emitters at $z = 1.47$ of Sobral et al. (2015). The Hβ emitters are not included in the observed emitters.

The redshifts and the fluxes of the major emission lines are summarized in Table 5.1. In the following analyses, we use the Hβ fluxes corrected for the stellar absorption. We assume the typical EW of the absorption line of 2 Å (Nakamura et al., 2004), and use the continua estimated from the Ks-band magnitudes after subtracting the contributions from emission lines. The correction factors for the Hβ stellar absorption are $\sim$1.06–1.10.

5.1.1 Stacking analysis

In order to investigate the averaged properties of the [OIII] emitters at $z \sim 3.24$, we carry out the stacking analysis of the obtained spectra by dividing the ten [OIII] emitters into two stellar mass bins, i.e. $\log(M_*/M_\odot) \geq 9.5$ and $\log(M_*/M_\odot) < 9.5$.

We convert the individual spectra to the rest-frame wavelength based on the derived redshifts, and normalize them with the total [OIII]λ5007 flux. The wavelength interval of the obtained spectrum in K and H-band is 2.1719 Å/pix and 1.6289 Å/pix, respectively. When converting them to the rest-frame spectra, we fix the wavelength interval to 0.25Å, and interpolate the spectra linearly. Noise spectra of the individual galaxies are also normalized with the total [OIII]λ5007 flux, and are converted to the rest-frame wavelength

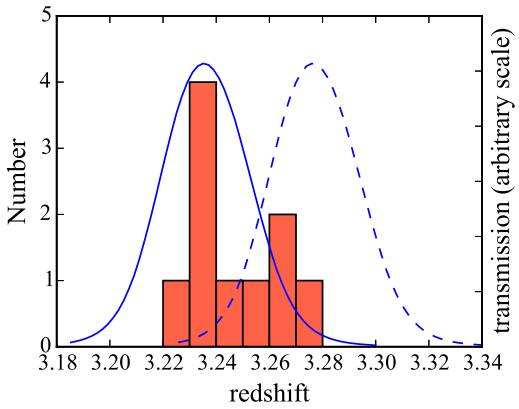

Figure 5.1: The redshift distribution of the [OIII] emitters that are confirmed with the MOSFIRE spectroscopy (filled histogram). The transmission curves of the HiZELS NB_K filter are also shown. The wavelength range of the NB_K filter is converted to the redshift ranges for the [OIII]λ5007 emission line (the solid curve) and the [OIII]λ4959 emission line (the dashed curve), respectively. It turns out that for three [OIII] emitters we actually captured their strong [OIII]λ4959 lines in the NB_K filter.

with a wavelength interval of 0.25Å. Then, the stacking of the individual spectra is carried out with the following equation:

$$f_{\rm stack} = \sum_i^N \frac{f_i(\lambda)}{\sigma_i(\lambda)^2} / \sum_i^N \frac{1}{\sigma_i(\lambda)^2}, \tag{5.1}$$

where $f_i(\lambda)$ is a flux density of the individual spectra and $\sigma_i(\lambda)$ is a sky noise as a function of the wavelength (Shimakawa et al., 2015). The noise spectrum for the stacked spectrum is calculated by an error propagation from the individual noise spectra.

The stacked spectra in the two stellar mass bins and the spectral fitting results using the `SPECFIT` are shown in Figure 5.3.

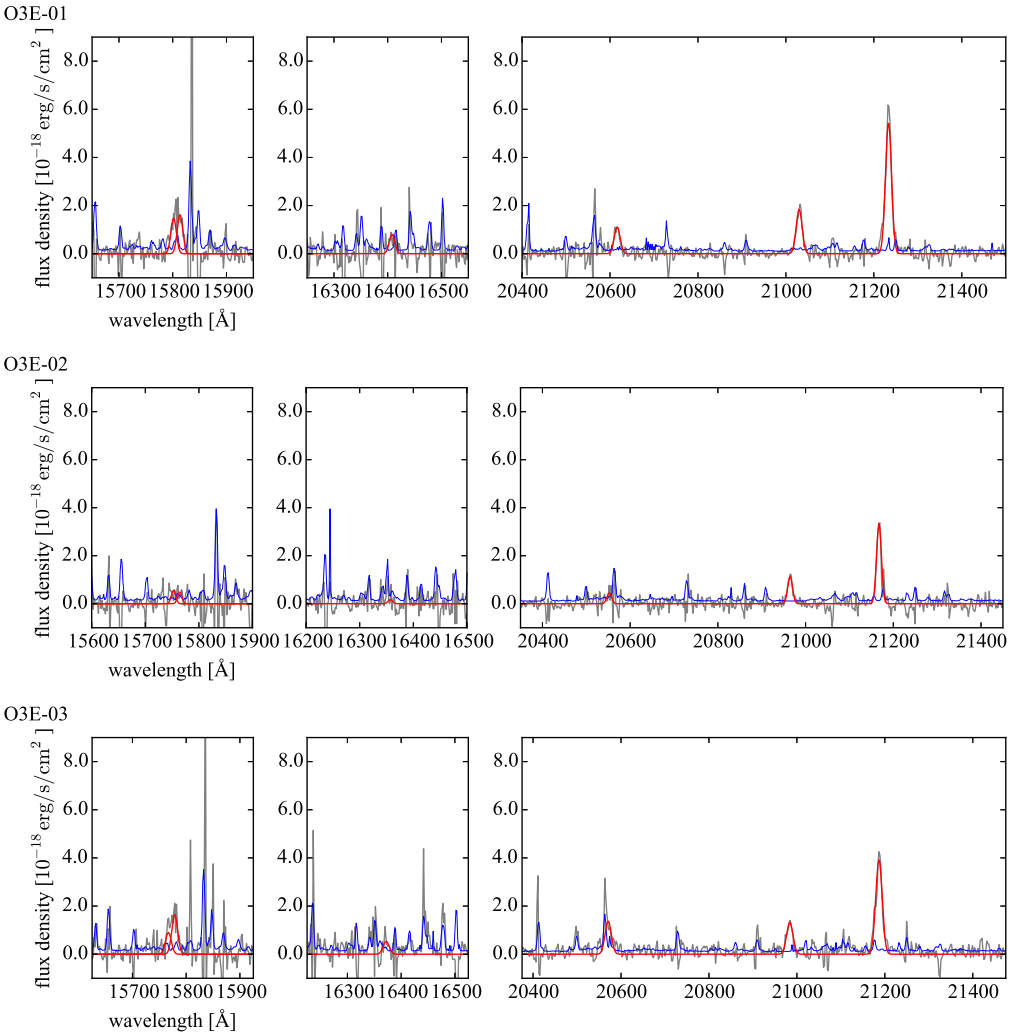

Figure 5.2: The obtained H and K-band spectra and the emission line fitting results of the ten [OIII] emitters. The reduced spectra are shown with the gray curves. The blue curves represent the 1σ sky noise. The emission line fitting result with a Gaussian component is shown with the red curves for each source. Three panels show the emission lines, [OII]λ3726, [OII]λ3729 (left panel), [NeIII]λ3868 (middle panel), and Hβ, [OIII]λ4959, and [OIII]λ5007 (right panel), respectively.

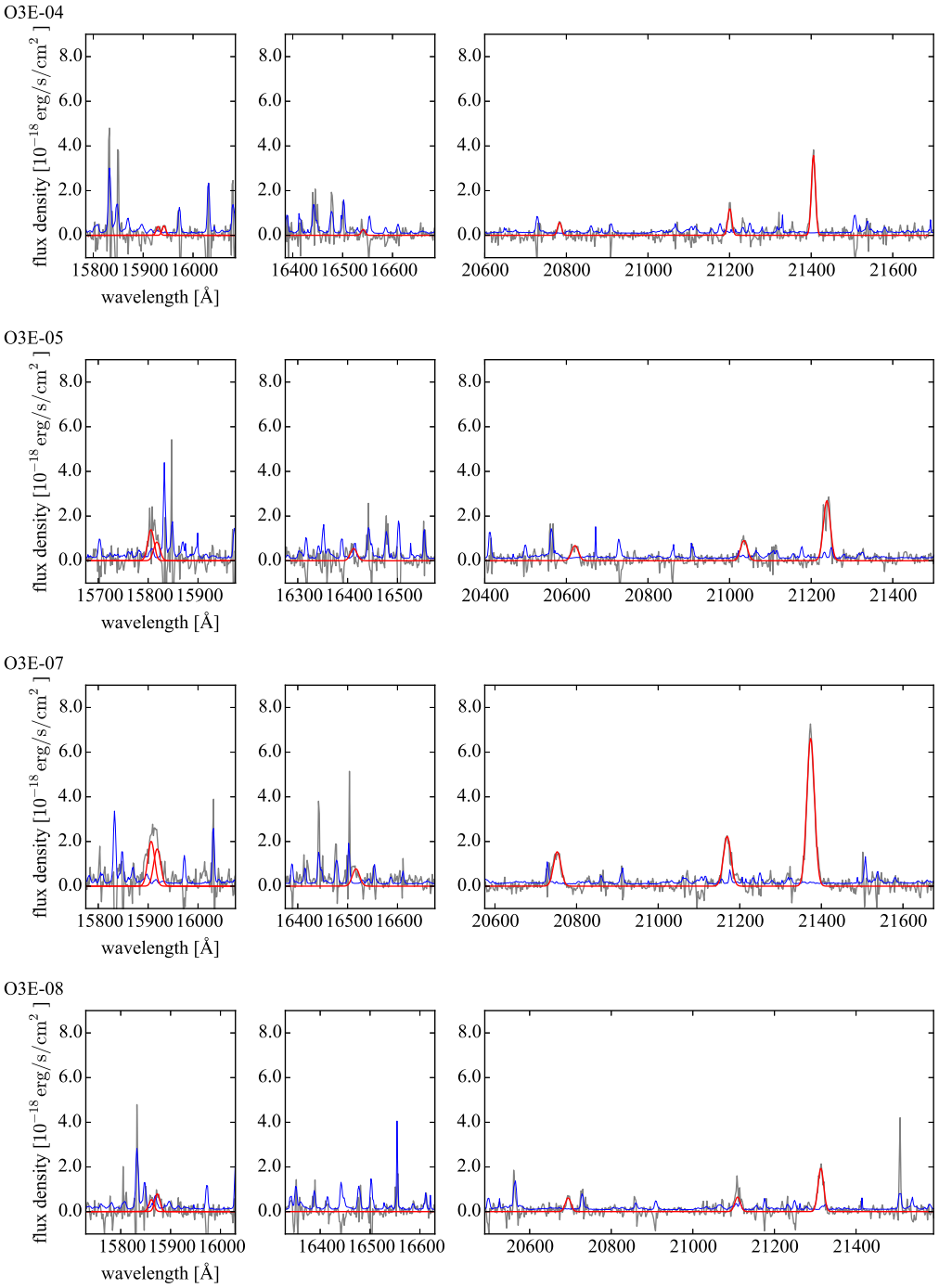

Figure 5.2: *continued*

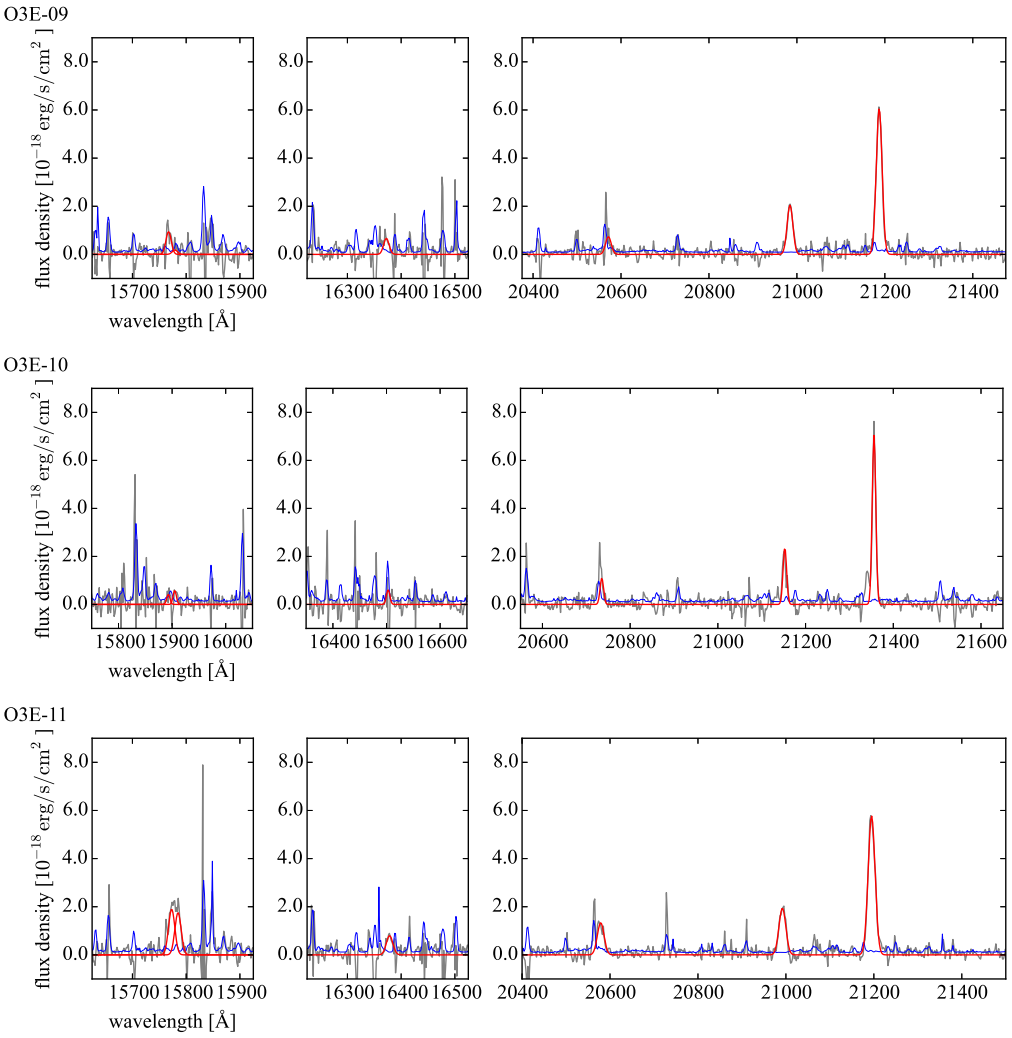

Figure 5.2: *continued*

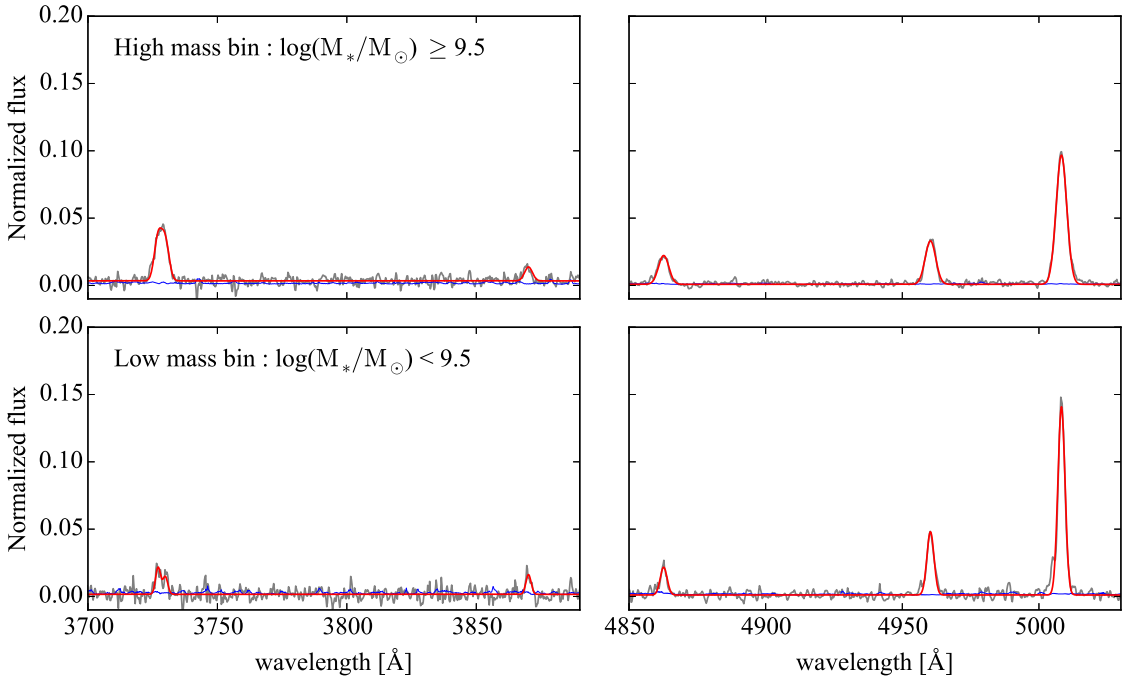

Figure 5.3: Stacked spectra of the [OIII] emitters constructed by dividing the samples into two stellar mass bins of $\log(M_*/M_\odot) \geq 9.5$ and $\log(M_*/M_\odot) < 9.5$. The stacked spectra are shown by the gray curves. The blue curves represent the 1σ sky noise. The emission line fitting results are shown in the red curves. We show the [OII] doublet and the [NeIII] in the left panel, and the Hβ and the [OIII] doublet in the right panel, respectively.

Table 5.1: Summary of the emission line properties of the confirmed [OIII] emitters with Keck/MOSFIRE.

ID	COSMOS2015	R.A.	DEC.	$z_{\rm spec}$	FWHM	$F_{\rm [OIII]\lambda5007}$	$F_{\rm H\beta}$	$F_{\rm [OII]}$	$F_{\rm [NeIII]}$
(1)	(2)				[km s^{-1}]	(3)	(4)	(5)	(6)
1	269781	149.9485	1.69460	3.2397	227.367 ± 6.425	9.378 ± 0.173	1.854 ± 0.159	3.967 ± 0.347	1.063 ± 0.167
2	269719	149.9777	1.69505	3.2265	183.865 ± 9.385	4.634 ± 0.194	0.609 ± 0.202	1.078 ± 0.252	$<$ 0.867
3	269241	149.9751	1.69375	3.2303	243.537 ± 11.126	7.187 ± 0.273	2.449 ± 0.446	3.464 ± 0.390	0.748 ± 0.189
4	264007	149.9418	1.68607	3.2740	162.528 ± 4.748	4.425 ± 0.105	0.699 ± 0.075	0.757 ± 0.163	$<$ 0.375
5	260873	149.9557	1.68044	3.2407	284.822 ± 9.979	5.778 ± 0.215	1.420 ± 0.137	3.578 ± 0.367	0.909 ± 0.210
7	293950	149.9887	1.73326	3.2677	308.506 ± 5.063	15.505 ± 0.205	3.511 ± 0.165	6.422 ± 0.346	1.411 ± 0.169
8	293774	149.9680	1.73321	3.2557	231.943 ± 12.564	3.419 ± 0.186	1.059 ± 0.114	1.752 ± 0.270	$<$ 0.318
9	289770	150.0213	1.72713	3.2304	221.664 ± 5.163	10.110 ± 0.196	1.190 ± 0.280	1.396 ± 0.261	0.857 ± 0.111
10	278714	149.9417	1.70949	3.2642	136.310 ± 3.900	7.282 ± 0.182	1.101 ± 0.241	0.768 ± 0.229	$<$ 0.942
11	274195	149.9889	1.70175	3.2320	261.732 ± 4.939	11.365 ± 0.177	2.553 ± 0.258	5.353 ± 0.257	1.215 ± 0.128

(1) IDs of the spectroscopically identified [OIII] emitters

(2) IDs in the COSMOS2015 catalog (Laigle et al., 2016).

(3)(4)(5)(6) Fluxes are shown in the unit of 10^{-17}[erg s^{-1}cm^{-2}], and not corrected for the dust extinction.

(4) The stellar absorption is not corrected for.

(5) [OII]λ3726 + [OII]λ3729 fluxes

(6) The fluxes with S/N $<$ 3.0 are replaced with the 3σ limit values.

5.2 Estimation of physical quantities

The observed [OIII] emitters are subsamples of the [OIII] emitters at $z = 3.24$ in the COSMOS field (Section 4.2). We re-perform the SED fitting for the ten [OIII] emitters by fixing their redshifts to those measured from the spectroscopy. We use the photometric catalog of the COSMOS2015, and follow the same procedure as described in Section 4.2. Before carrying out the SED fitting, we subtract the contributions of the emission lines, the [OIII] doublet and Hβ, and [OII] doublet, from the Ks and H-band magnitudes. In the following analyses, we use the stellar masses estimated from the SED fitting. The amount of dust extinction ($A_{\rm FUV}$) and SFRs (SFR$_{\rm UV}$) of the [OIII] emitters are also estimated in the same manner in Section 4.2 by fixing the redshifts to those determined from this spectroscopy. Stellar masses, SFR$_{\rm UV}$ and $A_{\rm FUV}$ of the [OIII] emitters are summarized in Table 5.2.

Figure 5.4 shows the stellar mass–SFR$_{\rm UV}$ diagram of the [OIII] emitters at $z = 3.24$. The [OIII] emitters which are spectroscopically confirmed by this spectroscopy are shown with the red stars. Figure 5.4 shows that our spectroscopic targets are not biased on the M_*–SFR plane with respect to our parent sample of [OIII] emitters at $z = 3.24$ in the same field (the gray dots), and also to other UV-selected galaxies at $3 \lesssim z \lesssim 3.7$ from Onodera et al. (2016) (the blue triangles).

Figure 5.5 shows the comparison of the two SFRs derived from UV and Hβ luminosities. We estimate SFR$_{\rm H\beta}$ as follows: We convert the dust-extinction-corrected Hβ luminosity to the Hα luminosity using the intrinsic Hα/Hβ ratio of 2.86 under the assumption of Case B recombination with a gas temperature $T_e = 10^4$ K and an electron density $n_e = 10^2$ cm^{-3} (Osterbrock & Ferland, 2006). Then we estimate SFRs using Eq. 3.4 (Kennicutt, 1998b), while SFRs are converted to the values when the Chabrier IMF is assumed (Chabrier, 2003) by dividing them by a factor of 1.7 (Pozzetti et al., 2007). The dust extinction is corrected for using the UV slope β (Heinis et al., 2013), and we assume $E(B-V)_{\rm nebular} = E(B-V)_{\rm stellar}$ here. We find that the two SFRs derived from the UV luminosities and from Hβ luminosities are broadly consistent with each other within a factor of 2. We can estimate their SFRs reasonably well from the UV luminosities with dust correction based on the UV slope even at $z > 3$ (cf. Figure 3.2).

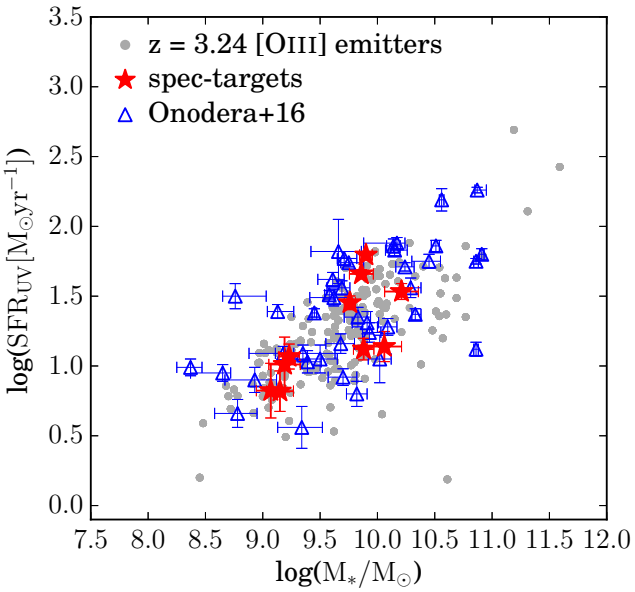

Figure 5.4: Stellar mass and SFR_{UV} relation of $z > 3$ star-forming galaxies. The gray dots represent the [OIII] emitters at $z = 3.24$ in the COSMOS field, same as the sample introduced in Section 4.2. The red stars show the [OIII] emitters which are spectroscopically confirmed with MOSFIRE. The open triangles are the UV-selected galaxies at $z = 3$–3.7 from Onodera et al. (2016).

5.3 ISM conditions of the [OIII] emitters

5.3.1 Mass–Excitation diagram

In Figure 5.6, we show the [OIII]λ5007/Hβ ratio as a function of the stellar mass (Mass-Excitation diagram; Juneau et al. 2011) in order to investigate the excitation states of the [OIII] emitters. In Juneau et al. (2011), they discussed the classification of the star-forming galaxies and AGNs on the Mass–Excitation diagram. As shown in Figure 1.5, star-forming galaxies and AGNs at $z \sim 0$ are distributed in different regions on this diagram, i.e. AGNs show strong [OIII] emission for their stellar masses. On the other hand, at higher redshifts, it has been found that star-forming galaxies, even relatively massive galaxies, show higher [OIII]/Hβ ratios (Shimakawa et al., 2015; Holden et al., 2016).

In Figure 5.6, we also show the local galaxies from the Galaxy And Mass Assembly (GAMA) survey DR2 data (Liske et al., 2015) and the UV-selected galaxies at $3 \lesssim z \lesssim 3.7$ from Onodera et al. (2016) for comparison. The [OIII] emitters at $z \sim 3.24$ show clearly

Table 5.2: Summary of the estimated physical quantities of the [OIII] emitters

ID	$\log(M_*)$	SFR_{UV}	A_{FUV}
	$[M_\odot]$	$[M_\odot yr^{-1}]$	[mag]
1	9.76 ± 0.05	28.33 ± 3.20	0.76 ± 0.10
2	9.15 ± 0.12	6.60 ± 2.20	0.00 ± 0.35
3	10.21 ± 0.15	34.12 ± 4.49	1.36 ± 0.12
4	9.19 ± 0.14	10.25 ± 4.63	0.95 ± 0.48
5	10.06 ± 0.15	13.78 ± 3.43	0.80 ± 0.26
7	9.9 ± 0.06	62.31 ± 2.99	1.18 ± 0.03
8	9.88 ± 0.09	13.21 ± 2.35	0.50 ± 0.178
9	9.07 ± 0.13	6.66 ± 3.00	0.47 ± 0.48
10	9.23 ± 0.09	11.68 ± 2.41	0.48 ± 0.21
11	9.86 ± 0.10	45.62 ± 3.16	1.13 ± 0.05

high [OIII]/Hβ ratios as compared to the local star-forming galaxies at a fixed stellar mass. This indicates that the ionization states of star-forming galaxies at $z > 3$ are much higher than the local counterparts.

Also, if we compare our [OIII] emitters at $z \sim 3.24$ to the UV-selected galaxies at the similar epoch from Onodera et al. (2016), there is no clear difference between the two samples. This indicates that the [OIII] emitters are not systematically biased towards higher [OIII]/Hβ ratios even though they are selected based on their strong [OIII] emission lines.

5.3.2 R_{23}-index versus [OIII]/[OII] ratio

In order to discuss the physical conditions of the [OIII] emitters further, we investigate the relation between the two line ratios. One is the ratio of $([OIII]\lambda\lambda5007, 4959 + [OII])/H\beta$ (R_{23}-index). The other is the ratio of $[OIII]\lambda5007/[OII]$. Although the R_{23}-index and the [OIII]/[OII] ratio depend on both the metallicity and the ionization parameter, the R_{23}-index is more sensitive to the metallicity and the [OIII]/[OII] ratio is more sensitive to the ionization parameter (e.g. Kewley & Dopita 2002). With these two emission lines, we can discuss the metallicity and ionization parameter simultaneously (Nakajima & Ouchi,

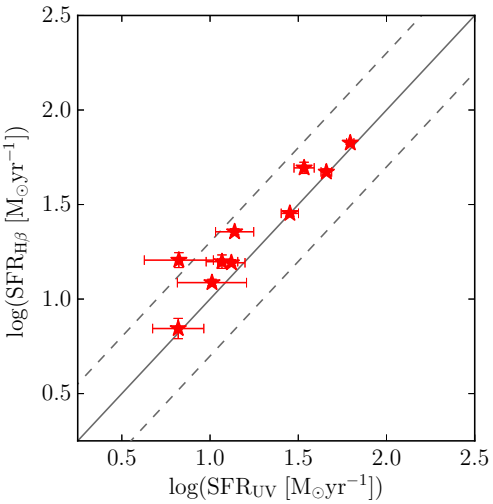

Figure 5.5: Comparison of SFRs derived from the UV luminosities and Hβ luminosities of the spectroscopically confirmed [OIII] emitters. Here we do not consider the extra extinction to the nebular emission, i.e. we assume $E(B-V)_{\rm nebular} = E(B-V)_{\rm stellar}$. Dust extinction is corrected for by using the UV slope β (Eq.3.1). The solid line represents the case where the two SFRs are identical, and the dashed lines represent the cases where the difference between the two is a factor of 2.

2014).

In Figure 5.7, we show our [OIII] emitters on the R_{23}–[OIII]/[OII] diagram together with the star-forming galaxies at the same epoch from the literature, namely, the UV-selected galaxies from Onodera et al. (2016) and the Lyα emitters (LAEs) from Nakajima et al. (2016).

We also show the model predictions on this diagram. The theoretical line ratios in the HII regions are estimated using the photoionization code `MAPPINGS V` [3] (`MAPPINGS`; Sutherland & Dopita 1993). In the `MAPPIGNS`, we assume a HII region with a constant pressure of $P/k = 10^{5.5}$cm^{-3} K, where k is the Boltzmann constant. A temperature of an HII region is set to be $\sim 10^4$ K, and then the density becomes $\sim$ 10–30 cm^{-3}, which is the typical value for a giant extragalactic HII regions (Kewley et al., 2013). We change the metallicity and ionization parameter independently as follows: $Z = 0.05,\ 0.2,\ 0.4,\ 1.0,$ and $2.0\ Z_\odot$, and $\log(q\ [\rm cms^{-1}]) = 8.35,\ 8.00,\ 7.75,\ 7.50,\ 7.25,$ and 7.00.

Comparing the [OIII] emitters with the UV-selected galaxies and LAEs at the same

[3] `https://miocene.anu.edu.au/mappings/`

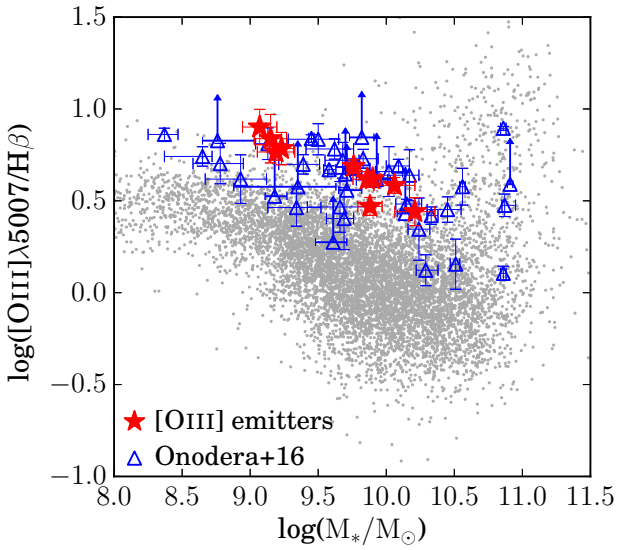

Figure 5.6: Stellar mass versus [OIII]λ5007/Hβ ratio (Mass-Excitation diagram; Juneau et al. 2011). The red stars represent the [OIII] emitters at $z \sim 3.24$, and the blue triangles show the UV-selected galaxies at the same epoch (Onodera et al., 2016). Some sources of Onodera et al. (2016) which are not detected with Hβ are shown with the 3σ lower limit values. The gray dots show the local galaxies from GAMA DR2 (Liske et al., 2015). For the local galaxies, both star-forming galaxies and AGNs are shown here. The Hβ fluxes are corrected for the stellar absorption.

epoch, the [OIII] emitters show a similar distribution on this diagram to the UV-selected galaxies rather than the LAEs, indicating that the ISM conditions of the [OIII] emitters are not so extreme like the LAEs on average.

5.3.3 Metallicity measurements

The gaseous metallicity of galaxies is an important physical quantity because it reflects the relative contributions of star-forming activities, inflows, and outflows of the individual galaxies. In order to measure the gaseous metallicities (i.e. the gaseous oxygen abundance; 12+log(O/H)) of galaxies, the line ratios of strong emission lines are often used (Section 1.4.3). The metallicity calibration methods using the strong emission lines have been established empirically (e.g. Pettini & Pagel 2004; Maiolino et al. 2008; Curti et al. 2016) or using the photoionization models (e.g. Kobulnicky & Kewley 2004; Kewley & Dopita 2002). It is well known that the different methods (different line ratios) give systematically different metallicities (Kewley & Ellison, 2008). In the following, we derive

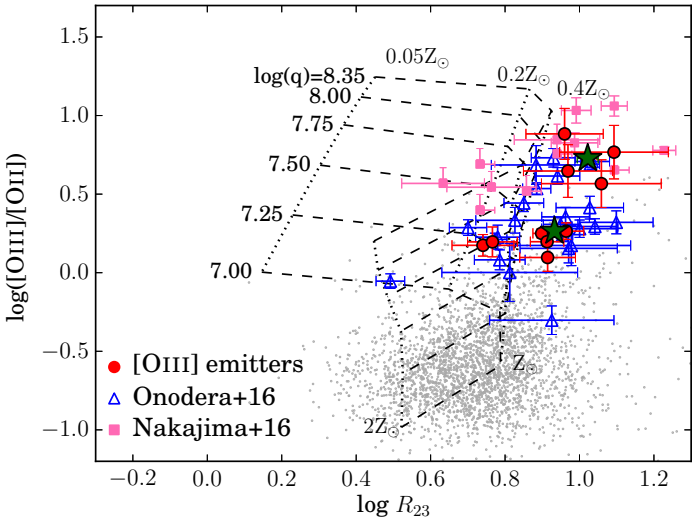

Figure 5.7: R_{23}-index versus [OIII]/[OII] ratio for different galaxy populations at $z > 3$. The filled circles show the [OIII] emitters at $z \sim 3.24$, the open triangles are the UV-selected galaxies at $z =$ 3–3.7 from Onodera et al. (2016), and the filled squares represent the LAEs at $z \sim 3$ from Nakajima et al. (2016). The gray dots are the local galaxies from GAMA DR2 (Liske et al., 2015). The star symbols represent the staking results of the [OIII] emitters (high-mass-bin and low-mass-bin). We also show the model prediction of the R_{23}-index and the [OIII]/[OII] ratio calculated using the photoionization code `MAPPINGS V`. The dashed lines represent the constant ionization parameters of $\log(q\ [\mathrm{cms}^{-1}]) = 8.35,\ 8.00,\ 7.75,\ 7.50,\ 7.25$, and 7.00. The dotted lines represent the constant metallicity of $Z = 0.05,\ 0.2,\ 0.4,\ 1.0$, and $2.0\ Z_\odot$.

the metallicities of the [OIII] emitters with the three different methods.

In Maiolino et al. (2008), they established the semi-empirical relations to measure gaseous metallicities using the five line ratios consisting of [OIII], Hβ, [NeIII], and [OII]. They parameterized the relations between the line ratios and 12+log(O/H) of the local star-forming galaxies by estimating the metallicities with the direct method (Section 1.4.3) at the low metallicity regime ($12 + \log(\mathrm{O/H}) \lesssim 8.4$), and by determining the metallicities based on the photoionization models at the high metallicity regime ($12 + \log(\mathrm{O/H}) \gtrsim 8.4$).

We also use the fully empirical relation of Curti et al. (2016). In Curti et al. (2016), based on the SDSS spectra, they measured the metallicities with the direct method. For the lower metallicity regime, they used the individual spectra, while at the higher metallicity regime, they used the stacked spectra to increase the S/N ratio of the weak auroral

lines. Then, they correlated six line ratios (combinations among four emission lines, [OIII], Hβ [OII], and [NII]) with the metallicity and established the metallicity calibration for each line ratio. With this method, they can extend the empirical metallicity calibration to the higher metallicity regime than Maiolino et al. (2008). In reality, we use four line ratios among the six with [OIII], Hβ, and [OII] lines here (Figure 5.9).

Based on the above two empirical relations (Maiolino et al. 2008; Curti et al. 2016), we fit the five or four line ratios simultaneously, and determine the best-fit metallicity that can minimize the χ^2 value. Here the χ^2 is defined as follows:

$$\chi^2 = \sum_{i=1}^{N} \frac{(\log\ R_{i,\mathrm{obs}} - \log\ R_{i,\mathrm{fit}})^2}{\sigma_{i,\mathrm{obs}}^2 + \sigma_{i,\mathrm{int}}^2}, \tag{5.2}$$

where $\log\ R_{i,\mathrm{obs}}$ and $\log\ R_{i,\mathrm{fit}}$ are the i-th line ratio obtained from the observed spectra and one obtained from the relation of Maiolino et al. (2008) or Curti et al. (2016) at a given metallicity (Onodera et al., 2016). $\sigma_{i,\mathrm{obs}}$ is the error of each line ratio from the observed spectra, and $\sigma_{i,\mathrm{int}}$ is the intrinsic scatter of a line ratio at a given metallicity, respectively. We use $\sigma_{i,\mathrm{int}}$ obtained in Jones et al. (2015) for the Maiolino et al. (2008) calibration (Onodera et al., 2016). For the Curti et al. (2016) calibration, as the intrinsic scatter, we apply the root-mean-square estimated for each relation (table2 in Curti et al. (2016)). In Figure 5.8 and 5.9, we show the relations between the metallicity, which are determined with the two different calibration methods, and the line ratios. The errors in the metallicities are determined by searching for the metallicities where $\Delta\chi^2 = 1$.

We also estimate ionization parameter from the derived metallicity using the equation of Kobulnicky & Kewley (2004):

$$\begin{aligned}\log\ q = &\{32.81 - 1.153y^2 + [12 + \log(\mathrm{O/H})](-3.396 - 0.025y + 0.1444y^2)\} \\ &\times \{4.603 - 0.3119y - 0.163y^2 + [12 + \log(\mathrm{O/H})](-0.48 + 0.0271y + 0.02037y^2)\}^{-1},\end{aligned} \tag{5.3}$$

where $y = \log\ [\mathrm{OIII}]\lambda\lambda 5007, 4959/[\mathrm{OII}]$.

We summarize metallicities and ionization parameters of the [OIII] emitters in Table 5.3. Note that these calibrations are established using the star-forming galaxies at $z = 0$. We here assume that the star-forming galaxies at $z > 3$ have similar ionization parameters as the local star-forming galaxies at a given metallicity. It is still under debate whether

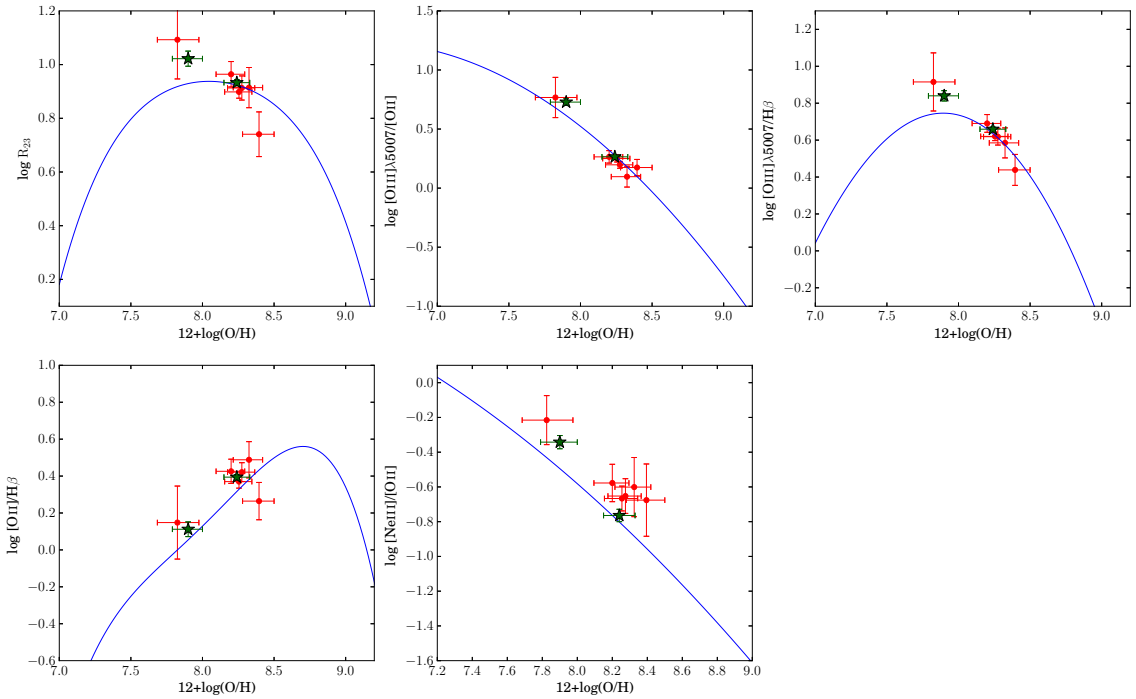

Figure 5.8: Relations between five line ratios and metallicities calibrated with Maiolino et al. (2008). The filled circles show the [OIII] emitters whose [NeIII] lines are detected at more than 3σ significance levels. The star symbols show the stacked spectra (high-mass-bin and low-mass-bin). The solid curve in each panel shows the relation derived in Maiolino et al. (2008).

the high redshift star-forming galaxies have higher ionization parameter than the local star-forming galaxies with the same gaseous metallicity or the star-forming galaxies have a similar ISM conditions both at low and high redshifts at the same metallicity (e.g. Nakajima & Ouchi 2014; Kewley et al. 2015; Sanders et al. 2016b).

We also apply other metallicity calibration based on the photoionization model, `MAPPINGS`, which is introduced by Kewley & Dopita (2002) and Kobulnicky & Kewley (2004). In their calibration, the R_{23}-index and [OIII]$\lambda\lambda$5007,4959/[OII] ratio are used to estimate the metallicity and the ionization parameter simultaneously. The relation between $\log(q)$ and [OIII]$\lambda\lambda$5007,4959/[OII] is given as Eq.(5.3). The relation between the metallicity and the R_{23}-index is parametrized as shown below. As seen in Figure 5.7, the R_{23}-index show a bimodality with respect to the metallicity. Therefore the parameterization of the relation between the R_{23}-index and the metallicity changes depending on the metallicity range. At the lower branch of 12+log(O/H) < 8.4,

Table 5.3: Summary of metallicities and ionization parameters of the [OIII] emitters estimated from the empirical relation of Maiolino et al. (2008) and Curti et al. (2016).

ID	log(q) [cm s^{-1}] (1)	12+log(O/H) (1)	log(q) [cm s^{-1}] (2)	12+log(O/H) (2)
1	$7.726^{+0.046}_{-0.049}$	$8.200^{+0.095}_{-0.105}$	$7.753^{+0.038}_{-0.039}$	$8.274^{+0.050}_{-0.054}$
2	–	–	$7.939^{+0.105}_{-0.107}$	$8.125^{+0.096}_{-0.112}$
3	$7.731^{+0.064}_{-0.067}$	$8.395^{+0.105}_{-0.115}$	$7.730^{+0.049}_{-0.050}$	$8.392^{+0.050}_{-0.057}$
4	–	–	$7.982^{+0.117}_{-0.120}$	$8.063^{+0.112}_{-0.138}$
5	$7.642^{+0.064}_{-0.067}$	$8.325^{+0.095}_{-0.110}$	$7.653^{+0.057}_{-0.058}$	$8.355^{+0.048}_{-0.054}$
7	$7.734^{+0.038}_{-0.041}$	$8.255^{+0.090}_{-0.100}$	$7.753^{+0.026}_{-0.027}$	$8.304^{+0.045}_{-0.050}$
8	–	–	$7.744^{+0.064}_{-0.066}$	$8.384^{+0.048}_{-0.057}$
9	$8.004^{+0.117}_{-0.116}$	$7.825^{+0.150}_{-0.140}$	$8.067^{+0.120}_{-0.122}$	$8.022^{+0.107}_{-0.124}$
10	–	–	$8.116^{+0.117}_{-0.118}$	$7.876^{+0.133}_{-0.144}$
11	$7.700^{+0.038}_{-0.041}$	$8.275^{+0.090}_{-0.100}$	$7.717^{+0.025}_{-0.027}$	$8.319^{+0.045}_{-0.051}$

(1) With the metallicity calibration of Maiolino et al. (2008). Metallicities and ionization parameters are estimated only for the emitters whose [NeIII] is detected at more than 3σ levels.

(2) With the metallicity calibration of Curti et al. (2016).

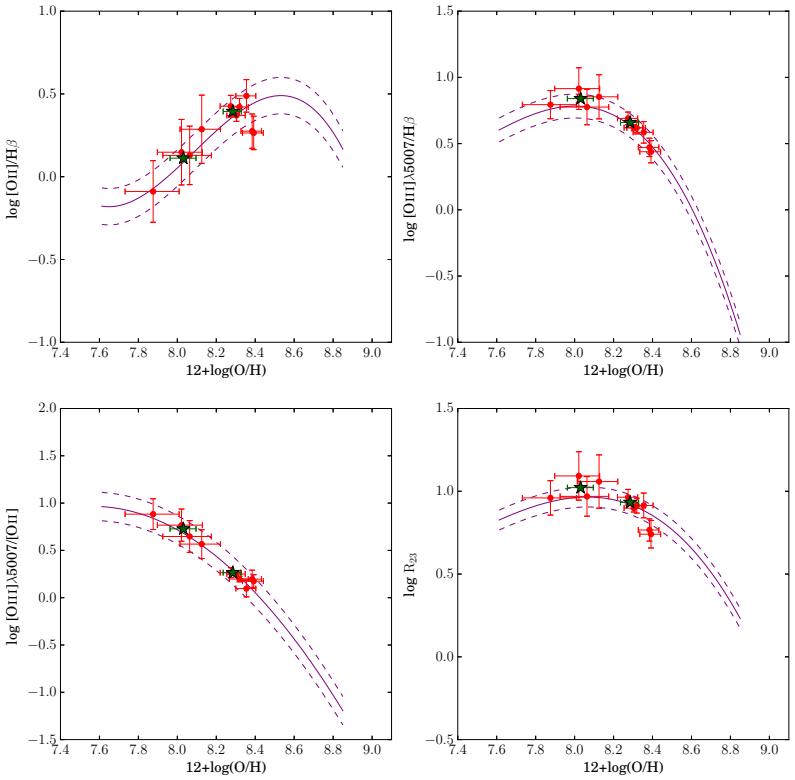

Figure 5.9: Relations between four line ratios and metallicities calibrated with Curti et al. (2016) method. The filled circles show the [OIII] emitters, and the star symbols represent the stacked spectra (high-mass-bin and low-mass-bin). The solid curve in each panel represents the relation derived in Curti et al. (2016). The dashed curves represent the root-mean-square of their fit.

$$12 + \log(\mathrm{O/H})_{\mathrm{lower}} = 9.40 + 4.65x - 3.17x^2 - \log(q)(0.272 + 0.547x - 0.513x^2), \quad (5.4)$$

and at the upper branch of 12+log(O/H) $\geq$ 8.4,

$$\begin{aligned} 12 + \log(\mathrm{O/H})_{\mathrm{upper}} &= 9.72 - 0.777x - 0.951x^2 - 0.072x^3 - 0.811x^4 \\ &\quad - \log(q)(0.0737 - 0.0713x - 0.141x^2 + 0.0373x^3 - 0.058x^4), \end{aligned} \quad (5.5)$$

where $x = \log R_{23}$. The [OIII]$\lambda\lambda$5007,4959/[OII] ratio and the R_{23}-index depend on both the metallicity and the ionization parameter. A consistent metallicity and ionization parameter are determined in an iterative manner using Eq.(5.3) and (5.4) or (5.5) according to the value of 12+log(O/H) (Kobulnicky & Kewley, 2004).

In order to determine the metallicity branch at a given R_{23}-index, an additional line ratio, such as [NII]/[OII], is required (Kobulnicky & Kewley, 2004). Since we cannot

Table 5.4: Summary of metallicities and ionization parameters of the [OIII] emitters estimated from the calibration method based on the photoionization models (Kobulnicky & Kewley, 2004). We show the two sets of solutions of the metallicity and ionization parameter corresponding to lower and upper metallicity branches, respectively. For the emitters of ID= 2, 9, their metallicities and ionization parameters do not converge.

ID	$\log(q)_{\rm lower}$ [cm s^{-1}]	$12+\log({\rm O/H})_{\rm lower}$	$\log(q)_{\rm upper}$ [cm s^{-1}]	$12+\log({\rm O/H})_{\rm upper}$
1	7.826 ± 0.055	8.439 ± 0.087	7.826 ± 0.071	8.439 ± 0.091
2	–	–	–	–
3	7.623 ± 0.055	8.088 ± 0.123	8.029 ± 0.131	8.821 ± 0.103
4	8.102 ± 0.143	8.334 ± 0.178	8.192 ± 0.255	8.481 ± 0.185
5	7.660 ± 0.068	8.372 ± 0.111	7.734 ± 0.108	8.531 ± 0.113
7	7.755 ± 0.029	8.309 ± 0.050	7.896 ± 0.041	8.581 ± 0.047
8	7.648 ± 0.067	8.119 ± 0.097	8.019 ± 0.130	8.791 ± 0.085
9	–	–	–	–
10	8.28 ± 0.147	8.258 ± 0.152	8.469 ± 0.244	8.539 ± 0.151
11	7.73 ± 0.040	8.346 ± 0.081	7.827 ± 0.056	8.546 ± 0.078

observe [NII]λ6583 lines for $z > 3$ galaxies from the ground, it is difficult to determine the metallicity branch for each object. In the following, we show the two sets of solutions of metallicity and ionization parameter (Table 5.4). The metallicity and ionization parameter for some [OIII] emitters do not converge after more than 10 times iterations, indicating that their line ratios cannot be explained with the photoionization models considered here. This might be partly due to the observational uncertainties or partly because the stellar populations of star-forming galaxies at high redshifts are different from those assumed in the photoionization models (e.g. Steidel et al. 2016; Strom et al. 2016).

5.3.4 Mass–Metallicity relation

In Figure 5.10, we show the relation between the stellar mass and the gaseous metallicity of the [OIII] emitters at $z \sim 3.24$. The metallicities in this figure are estimated from the empirical relations established by Maiolino et al. (2008) and Curti et al. (2016). As already

shown in a number of previous studies, the stellar mass and the metallicity of the [OIII] emitters show a correlation such that more massive galaxies have higher metallicities (e.g. Tremonti et al. 2004; Erb et al. 2006a; Maiolino et al. 2008; Troncoso et al. 2014). The estimated metallicities with the two calibration methods are not systematically different from each other. This might be because the two calibration methods use similar line ratios. We also show the UV-selected galaxies at the same epoch from the Onodera et al. (2016). They use the Maiolino et al. (2008) calibration to estimate metallicities. We find no clear difference between the [OIII] emitters and the UV-selected galaxies at the fixed stellar mass, indicating that they have similar metallicities with each other.

In Figure 5.11, we show the two solutions of metallicities obtained by the relations derived from the photoionization model. Given the mass–metallicity relation, it might be reasonable to select the metallicity at the upper metallicity branch at least for the [OIII] emitters with higher stellar masses, while it is not clear for the [OIII] emitters with lower stellar masses. In both cases, the metallicities of the [OIII] emitters are well below those of local star-forming galaxies at the fixed stellar mass.

5.3.5 Fundamental metallicity relation (FMR)

The mass–metallicity relation of star-forming galaxies has a large scatter in metallicities at a fixed stellar mass. It has been found that the deviations from the mass–metallicity relation are correlated with SFRs of galaxies. Such a correlation among stellar masses, metallicities, and SFRs is called the "fundamental metallicity relation" (FMR; e.g. Mannucci et al. 2010). As already mentioned in Section 1.4.3, it is said that the star-forming galaxies at least up to $z \sim 2.5$ follow the same relation (Mannucci et al., 2010; Troncoso et al., 2014), while there are also some studies showing that no correlation between gaseous metallicities and SFRs for the star-forming galaxies at $z \sim 1$–2.5 (e.g. Wuyts et al. 2014; Steidel et al. 2014; Sanders et al. 2015). The presence of the FMR especially at high redshifts is still under debate.

We check the distribution of our [OIII] emitters on the FMR. Figure 5.12 shows a relation of the [OIII] emitters between gaseous metallicities and $\mu_{0.32}$, which is defined as $\mu_{0.32} \equiv \log(\mathrm{M}_*/\mathrm{M}_\odot) - 0.32 \times \log(\mathrm{SFR})$ (Section 1.4.3).

Here we show the two gaseous metallicities estimated from Maiolino et al. (2008) and Curti et al. (2016) calibrations. The [OIII] emitters at $z \sim 3.24$ distribute clearly below

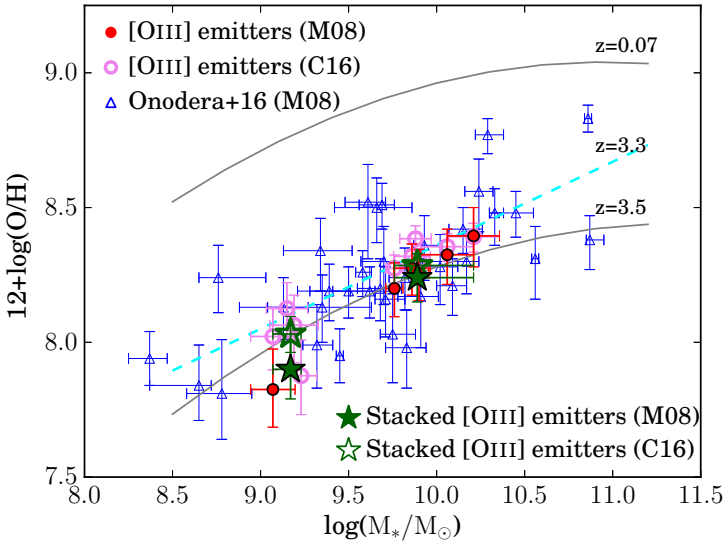

Figure 5.10: Relation between stellar masses and gaseous metallicities of $z > 3$ star-forming galaxies, namely the [OIII] emitters at $z \sim 3.24$ (circles: individual galaxies, stars: stacked spectra) and the UV-selected galaxies at $z \sim 3$–3.7 from Onodera et al. (2016). For the [OIII] emitters, metallicities are calibrated using the relations of Maiolino et al. (2008) (M08; the filled symbols) or Curti et al. (2016) (C16; the open symbols). Each solid curve represents the mass–metallicity relation at $z = 0.07$ (Maiolino et al., 2008) and 3.5 (Troncoso et al., 2014). The dashed curve represents the best-fitted mass–metallicity relation at $z \sim 3.3$ from Onodera et al. (2016).

the FMR shown with the solid curve in Figure 5.12. It has been suggested that the $z > 3$ star-forming galaxies do not follow the FMR and that SFRs of galaxies are not closely related to their metallicities at $z > 3$ (e.g. Mannucci et al. 2010; Troncoso et al. 2014; Onodera et al. 2016). At $z > 3$, the gas inflow towards galaxies is much more dominant than that in the present Universe, and it might cause little dependence of metallicity on SFR.

5.4 Summary of this chapter

In this chapter, we investigate the spectroscopic properties and physical conditions of ISM in the [OIII] emitters at $z \sim 3.24$ based on the NIR spectra (H and K bands) obtained with Keck/MOSFIRE. Our main targets are ten [OIII] emitter candidates at $z \sim 3.24$ in the COSMOS field obtained by HiZELS. All of the [OIII] emitters are spectroscopically identified as the real [OIII] emitters at $z = 3.22$–3.28. Three of them turn out to be

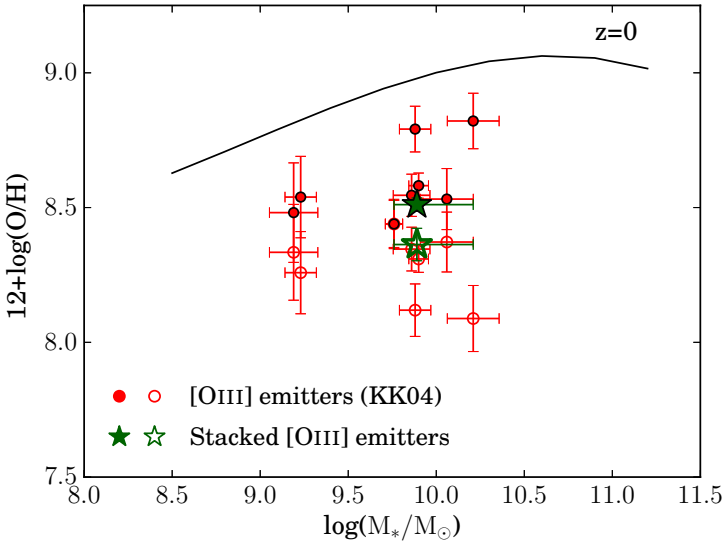

Figure 5.11: Relation between stellar masses and gaseous metallicities of the [OIII] emitters at $z \sim 3.24$ (circles: individual galaxies, stars: stacking results). In this figure, metallicities are calibrated using the relations of parameterized with the photoionization models by Kobulnicky & Kewley (2004). The filled symbols represent the metallicities in the upper branch, and the open symbols represent those in the lower branch. The solid curve shows the fitted mass–metallicity relation at $z \sim 0$ with the Kobulnicky & Kewley (2004) calibration (Kewley & Ellison, 2008).

[OIII]λ4959 emitters at slightly higher redshifts.

The [OIII] doublet, Hβ, and [OII] lines are detected at more than 3σ significance levels for all the [OIII] emitters. We investigate the stellar mass versus [OIII]/Hβ ratio (Mass–Excitation diagram) and the R_{23}-index versus [OIII]/[OII] ratio diagram of the [OIII] emitters. We find that they have higher excitation/ionization conditions as compared to the local star-forming galaxies.

On the other hand, comparing with the UV-selected galaxies at $z \sim 3.2$ from Onodera et al. (2016), there seems to be no difference between the two samples. The [OIII] emitters are not systematically biased towards galaxies with too extreme ISM conditions even though they are selected based on their strong [OIII] emission lines. This indicates that strong [OIII] emission is common among the *normal* star-forming galaxies at high redshifts.

We measure the gaseous metallicities of the [OIII] emitters with the three calibration methods using the strong emission lines. In all the cases, the derived metallicities of the [OIII] emitters are lower than those of star-forming galaxies at $z = 0$ at a given stellar mass. When we use the metallicities derived from the empirical calibrations, the [OIII]

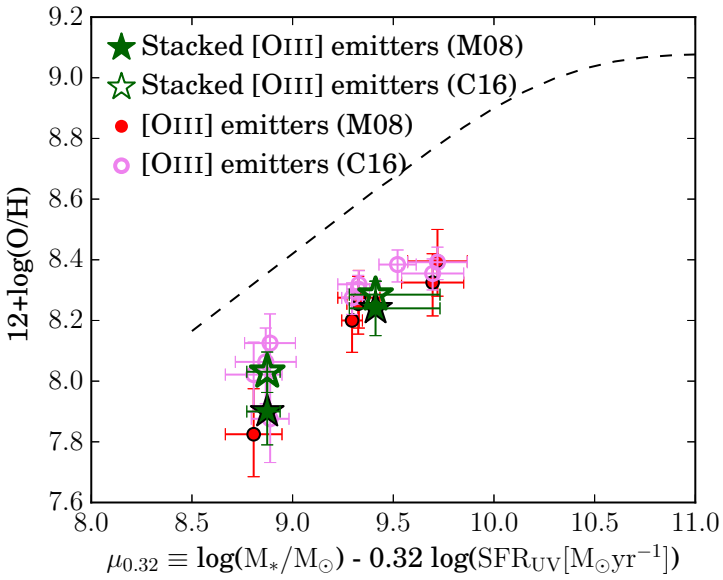

Figure 5.12: Relation between the gaseous metallicity and $\mu_{0.32}$ of the [OIII] emitters at $z \sim 3.24$. We show the two metallicities obtained from the Maiolino et al. (2008) and Curti et al. (2016) calibration for the individual galaxies (circles) and the stacked spectra (stars). The dashed curve represents the FMR presented in Mannucci et al. (2010, 2011).

emitters do not follow the fundamental metallicity relation. This indicates that the SFRs of the [OIII] emitters are not strongly correlated with the gaseous metallicities probably due to the vigorous gas inflow towards galaxies from outside.

6 Discussions

6.1 Mass growth from $z = 3.2$ to $z = 2.2$

In Chapter 4, we show the stellar mass–SFR relation of the [OIII] emitters at $z = 3.2, 3.6$ using the two different samples obtained by Mahalo-Subaru and HiZELS (Figure 4.5 and 4.6). Comparing it with that of the star-forming galaxies at $z = 2.2, 2.5$, we find that there is no significant change in the location of the main sequence for the star-forming galaxies between $z \sim 3.2$ and $z \sim 2.2$, but the distributions of the galaxies on the sequence are different between the two epochs. The [OIII] emitters at $z > 3$ show an offset towards the lower stellar masses with respect to the galaxies at $z \sim 2$.

Here we assume that the difference in galaxy distributions on the M_*–SFR plane between the emitters at $z \sim 3.2$ and 2.2 is simply due to the evolution of star-forming galaxies between the two epochs, and we discuss the stellar mass growth from $z \sim 3.2$ to $z \sim 2.2$. From our results that the location of the main sequence is unchanged during this time interval (1 Gyr), we can put some constraints on the history of star formation and thus that of the stellar mass growth. We here adopt the main sequence of star-forming galaxies defined with the Hα emitters at $z = 2.2, 2.5$ obtained by Mahalo-Subaru in the SXDF (Figure 4.5), i.e. SFR $= 120 M_{11}^{0.705}$ ($M_{11} = M_*/10^{11} M_\odot$). In order to stay on the same main sequence with time, the simplest evolutionary path would be that the individual star-forming galaxies evolve *along* the main sequence. This assumption should be valid if the galaxies keep forming stars at the rates above our threshold of the Hα NB imaging, i.e. SFR > 4 M$_\odot$yr^{-1} (dust-extinction-uncorrected) and EW$_{\rm rest} > 40$ Å.

The stellar mass growth between $z = 3.2$ and $z = 2.2$ can be then approximately tracked by the following derivative equation:

*Section 6.1 is mostly based on Suzuki et al.(2015)

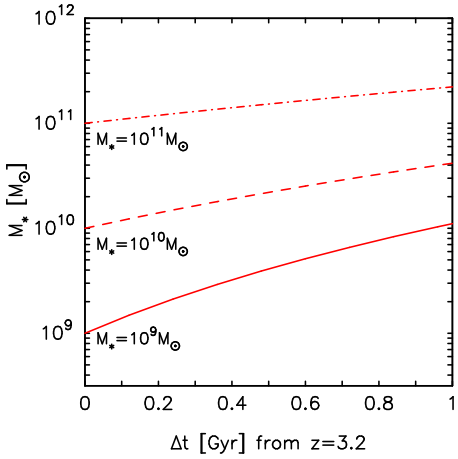

Figure 6.1: The predicted stellar mass growth of star-forming galaxies along the constant main sequence from $z = 3.2$ to $z = 2.2$. We calculate the mass growth assuming the three initial masses of 10^9, 10^{10}, and $10^{11} M_\odot$. A galaxy with $M_* = 10^9 M_\odot$ at $z = 3.2$ significantly increases its stellar mass by a factor of 10 during just one Gyr, while the mass increase of a galaxy with $M_* = 10^{11} M_\odot$ is a factor of 2.

$$\begin{aligned} \mathrm{d}M_*/\mathrm{d}t &= (1-R) \times \mathrm{SFR} \\ &= (1-R) \times 129\ M_{11}^{0.705}, \end{aligned} \tag{6.1}$$

where the return mass fraction R is 0.3 for the Salpeter IMF. Using this equation, a galaxy with $M_* = 10^9 M_\odot$ at $z = 3.2$ can increase its stellar mass by a factor of 10 to $\sim 1.1 \times 10^{10} M_\odot$ by $z = 2.2$, while a galaxy with $M_* = 10^{11} M_\odot$ can grow in mass by a factor of 2 as shown in Figure 6.1. Therefore, from more than 50% up to 90% of the stellar mass of the star-forming galaxies at $z = 2.2$ can be formed during the 1 Gyr time interval between $z = 3.2$ and 2.2. The majority of the galaxies with $M_* > 10^9 M_\odot$ that we see at $z = 3.2$ would grow to massive galaxies of $M_* > 10^{10} M_\odot$ at $z = 2.2$, if they stay on the main sequence and keep their high star-forming activities.

Note also that, in this simple model, galaxies *climb up* the main sequence, i.e. SFR increases a lot from $z = 3.2$ to $z = 2.2$ as the stellar mass grows (as $\mathrm{M}_*^{0.7}$). This indicates that the star-forming activities of galaxies at $z > 3$ are accelerated towards the peak epoch of galaxy formation at $z \sim 2$. In this respect, $z > 3$ is the *pre-peak epoch* of galaxy

formation. In order to achieve such a rapidly increasing star-forming activity, an increasing rate of gas infall from outside is required, since otherwise the quick gas consumption would lower the SFR as time progresses. In order to verify the presence of such continuous gas infall more quantitatively, we estimate the gas mass of the [OIII] emitters from their SFR surface densities by assuming the Schmidt–Kennicutt relation (Kennicutt, 1998a). SFR surface densities ($\Sigma_{\rm SFR} = {\rm SFR}/\pi r_e^2$) are estimated by using SFRs derived from UV luminosities in Section 4.1.3 and the effective radius r_e in Section 4.5. We then calculate gas depletion timescale of $t_{\rm dep} = M_{\rm gas}/{\rm SFR}$. The depletion timescale of the [OIII] emitters is estimated to be $\sim$ 0.3 Gyr, and is shorter than 1 Gyr. This means that the [OIII] emitters at $z = 3.2$ would consume all the remaining gas and terminate the star formation before $z = 2.2$ if there is no gas supply from the outside of galaxies.

We have to mention that we have assumed the exponentially *declining* SFH in the form of SFR $\sim \exp(-t/\tau)$ in the SED fitting, while we now claim that the SFR *increases* with time from $z = 3.2$ to $z = 2.2$. In order to verify the impact of assumed form of SFHs on the resulting physical quantities in the SED fitting, we re-estimate the stellar masses and SFRs of the [OIII] emitters by assuming the exponentially *increasing* SFH. In the case of the increasing SFH, the estimated stellar masses vary only by a factor of 0.9–1.3 for most of our sample, while the SFRs derived with $A_{\rm V}$ values from the SED fitting can increase by a factor of $\sim$ 1.4. However, such a modest offset would be systematic and would apply to both of the samples at $z = 3.2$ and $z = 2.2$. Therefore, it should not change our results significantly.

In reality, some galaxies would stop their star formation and evolve to quiescent galaxies by $z = 2.2$. Such quenching process should happen on a relatively short timescale so that galaxies do not significantly appear on the lower side of the main sequence and break the tight sequence with a substantial amount of scatter. Also, we have ignored the effect of galaxy–galaxy mergers, which can also increase the stellar mass of galaxies. Moreover, some galaxies would pop out all of a sudden on the main sequence with $M_* > 10^{10} M_\odot$ sometime between $z = 3.2$ and $z = 2.2$, which were below $M_* \leq 10^9 M_\odot$ at $z = 3.2$ or somewhat off the main sequence. Those galaxies should form stars at even higher rates such as in a starburst mode, and the fraction of stars that are formed between the two epochs can be even larger than 90%.

The amount of those missing galaxies that are not considered in the simple toy model

above can be estimated by the comparison of number densities of the [OIII] emitters at $z = 3.2$ and the Hα emitters at $z = 2.2$. The number density of the [OIII] emitters at $z = 3.2$ with $M_* \geq 10^9\ M_\odot$ is $(1.7 \pm 0.3) \times 10^{-3}$ Mpc^{-3}, while that of the Hα emitters at $z = 2.2$ with $M_* \geq 10^{10}\ M_\odot$ is $(2.7 \pm 0.5) \times 10^{-3}$ Mpc^{-3}. Here we have taken into account the mass growth predicted by the above model. The latter number is ~ 1.6 times larger at more than 4σ significance level with respect to errors. This suggests that galaxies may actually appear (more that those disappear) on to the main sequence suddenly between $z = 3.2$ and 2.2.

In any case, it is likely that star-forming galaxies grow at an accelerated pace during this time interval, assuring that this epoch is critically important for galaxy formation.

We also investigate the size growth of galaxies from $z = 3.2$ to $z = 2.2$ by assuming that the mass–size relation is unchanged between $z = 3.2$ and 2.2, as suggested in Section 4.5.1. Using the mass–size relation of late-type galaxies at $z \sim 2.75$ from van der Wel et al. (2014), the effective radius of a galaxy with $M_* = 10^9 M_\odot$ at $z = 3.2$ would grow in size by a factor of ~ 1.5 by $z = 2.2$, and the size growth ratio does not depend much on the initial stellar mass of galaxies at $z = 3.2$. The size growth is not so strong from $z = 3.2$ to 2.2 as compared to the mass growth that we just discussed above. Considering the growth of the stellar mass and size of galaxies from $z = 3.2$ to $z = 2.2$ together, we can also estimate the evolution in stellar mass surface density. It is predicted to grow by a factor of 5 for a galaxy with $M_* = 10^9 M_\odot$ at $z = 3.2$.

6.2 Appearance of the massive, dusty, and actively star-forming galaxies between $z > 3$ and $z \sim 2$

In Section 4.4, we investigate the relation between the stellar mass and $\mathrm{sSFR_{UV}}$, and the one between the stellar mass and A_{FUV} of the [OIII] emitters at $z = 3.24$ and $z = 2.23$ in the COSMOS field obtained by HiZELS. We compare the number distributions of $\mathrm{sSFR_{UV}}$ and A_{FUV} between the two samples after dividing them into three stellar mass bins, namely $\log(\mathrm{M_*/M_\odot}) < 9.65$, $9.65 \leq \log(\mathrm{M_*/M_\odot}) < 10.3$, and $\log(\mathrm{M_*/M_\odot}) \geq 10.3$. We find that the numbers of galaxies are clearly different at the highest stellar mass bin between the two epochs. The number of the massive [OIII] emitters is significantly smaller at $z = 3.24$ than at $z = 2.23$. In particular, the massive galaxies with higher $\mathrm{sSFR_{UV}}$ and/or higher A_{FUV}

are almost absent at $z \sim 3.24$ (Figure 4.9). Since we are comparing the [OIII] emitters at different redshifts in the same field, the selection bias should not be an issue for this comparison.

At the peak epoch, dusty and massive star-forming galaxies are more common than at $z > 3$. Such galaxies at $z \sim 2.2$ tend to have high sSFRs, and to be above the M_*–SFR relation at that epoch. Star-forming activity of some massive galaxies might be boosted and become dustier between $z \sim 3.2$ and 2.2. This suggests the some *characteristic* physical mechanisms exist behind this phase transition between the two epochs.

As the next step, we are motivated to investigate the internal/external physical processes in action of the galaxies both on and off the main sequence. For this purpose, high resolution observations by the AO-assisted imaging and the Atacama Large Millimeter/submillimeter Array (ALMA) are required. This is exactly the major part of our future directions that we have come up with motivated by this *Thesis* (see Chapter 8 for more details).

6.3 ISM conditions of star-forming galaxies at high redshifts

In Chapter 5, we show spectroscopic results of the HiZELS [OIII] emitters obtained by Keck/MOSFIRE observations. We compare our [OIII]-selected galaxies with the UV-selected galaxies at $z = 3$–3.7 from Onodera et al. (2016) on the Mass–Excitation diagram (Figure 5.6), R_{23}-index versus [OIII]/[OII] ratio diagram (Figure 5.7), and mass–metallicity relation (Figure 5.10). We find that there is no clear difference between the two samples on any of the figures, indicating that the [OIII]-selected galaxies have similar metallicities and ionization parameters to those of the UV-selected galaxies at $z \sim 3$–3.7. In the local Universe, strong [OIII] emission is often regarded as an evidence for the presence of AGNs. In the high redshift Universe, because of the high excitation levels of normal star-forming galaxies due to their higher sSFRs and lower metallicities, [OIII] emission is generally strong and thus can be a tracer of *normal* star-forming galaxies. This again strongly assures the usefulness of the [OIII] emitters to identify star-forming galaxies at $z > 3$ (where Hα is no longer available).

We compare the star-forming galaxies at $z \sim 3.2$ and $z \sim 2.2$ in terms of ISM conditions in Figure 6.2 and 6.3. We here introduce a sample of star-forming galaxies at $z \sim 2.2$ taken

from Cullen et al. (2014) for comparison. Their spectra were obtained by the 3D-*HST* survey, which is a NIR grism spectroscopy survey with the *HST* (Brammer et al., 2012). They divided 93 galaxies into six subsamples according to stellar masses, and stacked individual spectra for each subsample. They measured metallicities based on Maiolino et al. (2008) method without using the [NeIII]/[OII] ratio for calibration. Although this sample is not selected based on the same selection criteria as the [OIII] emitters, this is primarily spectroscopically confirmed to be at $z \sim 2.2$ using the [OIII] emission lines. We consider that these galaxies have relatively higher EWs of [OIII] emission lines similar to our [OIII] emitters.

Figure 6.2 and 6.3 show the R_{23}-index versus [OIII]/[OII] ratio diagram and the stellar mass–metallicity diagram of our [OIII] emitters together with Cullen et al. (2014) sample at $z \sim 2.2$ (stacking results). We find that the redshift evolution of the ionization and excitation properties of the ISM are not so strong between the two epochs (Figure 6.2). Also, considering that the difference between the metallicity calibration methods of Curti et al. (2016) and Maiolino et al. (2008) is small (Section 5.3.4), there is no significant offset of the mass–metallicity relation between the two samples at different epochs. In other words, Figure 6.3 suggests that the mass–metallicity relation does not strongly evolve from $z \sim 3.2$ to 2.2, although the sample size is very limited. When comparing the two samples on the $\mu_{0.32}$ versus metallicity plane (Figure 6.4; FMR), they show similar distributions on this diagram, indicating that the relations between stellar masses, SFRs, and metallicities of star-forming galaxies do not largely change between $z \sim 3.2$ and 2.2. As galaxies increase their stellar masses by star formation, their metallicities would increase along the mass–metallicity relation at least for the galaxies in a stellar mass range covered by our spectroscopy.

We note, however, that the redshift evolution of the mass–metallicity relation and the correlation between SFRs and gaseous metallicities are still under debate because of the discrepancy between the metallicity calibration methods and the limited sample size of high redshift galaxies. It is required to obtain a more systematic large sample covering a wide stellar mass range of star-forming galaxies at $z > 3$.

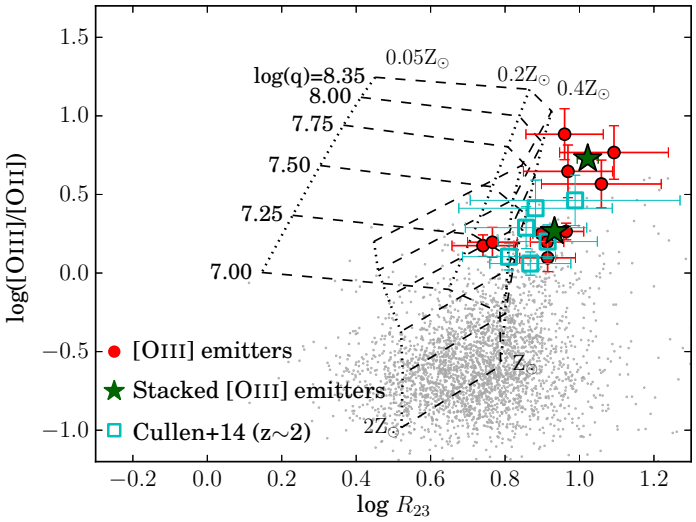

Figure 6.2: Comparison with the star-forming galaxies at $z \sim 2.2$ on the R_{23}-index–[OIII]/[OII] ratio diagram. The filled circles show the individual [OIII] emitters at $z \sim 3.24$. The star symbols show the stacking results of the [OIII] emitters. The open squares represent the stacking results of the star-forming galaxies at $z \sim 2.2$ from Cullen et al. (2014). The model grids are the same as in Figure 5.7.

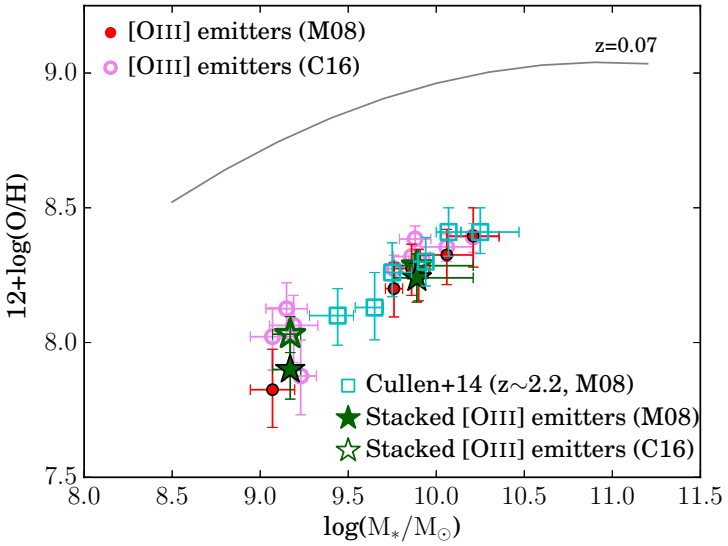

Figure 6.3: Mass–metallicity relation of our [OIII] emitters at $z \sim 3.4$ (circles: individual galaxies, stars: stacked spectra) and star-forming galaxies at $z = 2$–2.3 from the 3D-*HST* (the open squares; Cullen et al. 2014). The two metallicity calibration methods are applied, namely, the Maiolino et al. (2008) calibration (M08) and the Curti et al. (2016) calibration (C16).

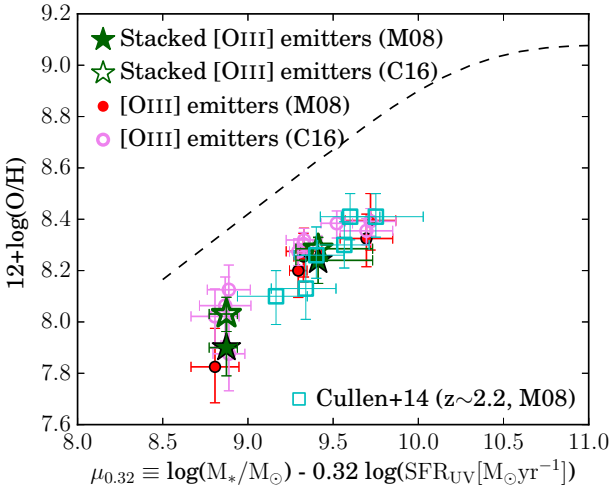

Figure 6.4: Fundamental metallicity relation of our [OIII] emitters $z \sim 3.24$ (circles: individual galaxies, stars: stacked spectra) and star-forming galaxies at $z = 2$–2.3 (Cullen et al., 2014). The dashed curve represents the fundamental metallicity relation presented in Mannucci et al. (2010, 2011).

7 Summary and Conclusion

Galaxy formation activity is known to be peaked at $z \sim 2$. In this *Thesis*, we aim to go further back in time to $z > 3$ in order to understand how the activity is increased towards the peak epoch. For this purpose, investigating the galaxy properties at the rest-frame optical is essential where the dust extinction is relatively free and nearly stellar mass or SFR-selected galaxies can be constructed.

We construct samples of [OIII] emitters through two NB imaging surveys, namely Mahalo-Subaru and HiZELS. The advantage of the NB selection is that we can construct a nearly SFR limited sample of galaxies within a narrow redshift slice. Moreover, since we can know a priori line fluxes and redshifts of the individual galaxies precisely, the NB-selected samples provide us with the unique and ideal samples of star-forming galaxies at high redshifts for follow-up observations, such as line diagnostic spectroscopy, integral field unit (IFU) observations, ALMA line observations, and so on.

First of all, in Chapter 3, we compare the Hα emitters and [OIII] emitters at $z = 2.23$ in the COSMOS field in order to investigate the usefulness of the [OIII] emission line as a tracer of star-forming galaxies at high redshifts. We have found that there is no clear difference between the galaxy populations traced by Hα and [OIII] at $z = 2.23$. The [OIII]-selected galaxies are not strongly biased to any particular galaxy population with respect to the Hα-selected galaxies which are representing the star-forming galaxies at all redshifts (e.g. Oteo et al., 2015, for $z \sim 2$). These results strongly support the importance and effectiveness of the [OIII] emitter surveys at $z > 3$, where the Hα emission line is no longer accessible from the ground. It opens up a new window to probe the star formation history before the peak epoch of galaxy formation. This is one of the important conclusions of this *Thesis*.

In Chapter 4, we investigate the star-forming activity of the [OIII] emitters at $z > 3$ and compare them with those of the NB-selected star-forming galaxies at $z \sim 2$. Here we

have introduced the two different samples of the [OIII] emitters at $z > 3$, namely the [OIII] emitters at $z = 3.18, 3.63$ obtained by Mahalo-Subaru project and the [OIII] emitters at $z = 3.24$ obtained by HiZELS survey. We discuss the two samples separately. The [OIII] emitters at $z > 3$ show a clear correlation on the stellar mass–SFR ($\mathrm{SFR_{UV}}$) diagram, as is known as the star-forming main sequence in many previous works. When comparing them with the Hα or [OIII] emitters at $z = 2.2$, 2.5 which are obtained in the same NB imaging observations, the [OIII] emitters at $z > 3$ show a clear offset towards the lower stellar masses on the M_*–SFR plane while the normalization of the main sequence is almost unchanged between the two epochs. This indicates a strong evolution of galaxies along the main sequence since the pre-peak epoch of cosmic star formation at $z > 3$ towards the peak epoch at $z \sim 2$. We also compare the $\mathrm{sSFR_{UV}}$ and A_{FUV} of the [OIII] emitters at $z = 3.24$ and 2.23. By dividing samples into three stellar mass bins, we find that a population of massive galaxies ($\log(\mathrm{M_*/M_\odot}) \geq 10.3$) with high A_{FUV} and high $\mathrm{sSFR_{UV}}$ seems to emerge between $z \sim 3.2$ and 2.2.

In order to investigate more detailed physical conditions of the [OIII] emitters, we carried out a NIR spectroscopic observation with Keck/MOSFIRE. We obtained the H and K-band spectra of the ten [OIII] emitters at $z = 3.24$ in the COSMOS field. We study the correlations between [OIII]/Hβ ratios and stellar masses, and the relation between the R_{23}-index and [OIII]/[OII] ratios of our [OIII] emitters in order to investigate their ionization/excitation states. We compare our [OIII] emitters with other galaxy populations at similar redshifts, namely the UV-selected galaxies (Onodera et al., 2016) and the LAEs (Nakajima et al., 2016) on these diagrams. We find that the [OIII] emitters show similar ISM conditions to those of the UV-selected galaxies, which are different from those of the LAEs.

We measure their gaseous metallicities using three different methods. On the mass–metallicity diagram, the [OIII] emitters at $z \sim 3.24$ show significantly lower metallicities than the star-forming galaxies at $z = 0$ at the fixed stellar mass. We also compare them to the Onodera et al. (2016) sample, and find that the two samples are similarly distributed on this diagram. We conclude that the selection of star-forming galaxies based on the strength of the [OIII]λ5007 emission line does not introduce a bias towards galaxies with low metallicities. This is because the star-forming galaxies at $z \sim 3$ generally have strong [OIII] emission lines probably due to higher ionization states excited by much higher sSFR.

We also find that our [OIII] emitters do not follow the fundamental metallicity relation that is seen for the local star-forming galaxies. This is probably due to the metal dilution by vigorous gas inflows that are feeding the galaxies at $z > 3$ (Mannucci et al., 2010; Troncoso et al., 2014; Onodera et al., 2016).

In Chapter 6, we use a simple toy model to estimate the stellar mass growth of star-forming galaxies from $z = 3.2$ to $z = 2.2$ (1 Gyr). We assume that the galaxies evolve along the constant star-forming main sequence between the two epochs, and estimate how their stellar masses and SFRs evolve with time. Under such a simple assumption, a galaxy with $M_* = 10^9 M_\odot$ should increase its mass by a factor of 10 during just 1 Gyr, while a galaxy with $M_* = 10^{11} M_\odot$ can grow in mass by a factor of 2. SFRs also increase with time, and therefore massive gas infall from the outside of galaxies is required in order to achieve such dramatic increase in mass and SFR.

We see a larger fraction of massive galaxies with high $A_{\rm FUV}$ and high $\rm sSFR_{UV}$ at $z \sim 2.2$ compared to $z \sim 3.2$. This suggests that the mode of star formation in some massive galaxies is changed from a normal and secular evolutionary phase to a more bursty and dusty phase from $z \sim 3.2$ to $z \sim 2.2$.

From a spectroscopic view, we find that there is no strong evolution of ionization and excitation properties of star-forming galaxies from $z = 3.2$ to 2.2, and also that the metallicities at the fixed stellar mass are almost consistent between our [OIII] emitters at $z = 3.24$ and star-forming galaxies at $z \sim 2.2$ (Cullen et al., 2014).

When we fix the stellar mass range, the star-forming activity and the ISM conditions do not significantly change between the two epochs. As galaxies increase their stellar masses by star formation, their SFRs and gaseous metallicities would evolve along the scaling relations, such as the star-forming main sequence and the mass–metallicity relation. For the less massive galaxies, their mode of star formation does not change, and they grow rapidly in stellar masses between the two epochs. As for the massive galaxies, some change their mode of star formation and form stars more efficiently in a dusty phase from $z > 3$ to $z \sim 2$.

Although we now have a better understanding of the global properties of star-forming galaxies at $z > 3$, the current data and the analyses do not tell us why the galaxy activity are accelerated and the mode of star formation are changed in some massive galaxies between the two epochs. In order to understand the physical processes involved in such

a drastic evolution since $z > 3$ towards the peak epoch, we will need to investigate their internal structures and kinematics, as well as to study galaxies in different environments. Also, studying the molecular gas components of star-forming galaxies with ALMA will be the key to investigate further the physical origins of the accelerated galaxy growth from $z > 3$.

8 Future prospects

As mentioned in the last part of Chapter 7, in order to investigate physical processes involved in an accelerated star-forming activity since $z > 3$, it is required to carry out further observations and to obtain more detailed information about the individual galaxies. In the following, we describe our future prospects for extending the studies targeting the [OIII] emitters at $z \sim 3$–3.6.

Resolving stellar components and star-forming regions within individual galaxies

In order to understand what physical processes are actually occurring within the [OIII] emitters, we need to resolve the internal structures and to investigate morphologies of individual galaxies. This requires observations with much higher angular resolutions for high redshift galaxies. Our team has been conducting the AO-assisted BB+NB imaging with Subaru/IRCS for $z \sim 2$ Hα emitters across various environments (Ganba-Subaru; co-PIs; Y. Minowa and Y. Koyama). With the AO-assisted imaging observations, we can routinely achieve $\sim$ 0.1–0.2 arcsec angular resolution which corresponds to $\sim$ 1 kpc at $z \sim 2$. Therefore it enables us to resolve galaxies into a typical clump scale ($\sim$ 1 kpc) at high redshifts (e.g. Genzel et al. 2008; Förster Schreiber et al. 2009). Moreover, by combining the AO and NB imaging, we can directly trace the star-forming regions within a galaxy, and thus investigate how the star-forming activity is propergated.

We plan to expand such observations towards the [OIII] emitters at $z > 3$. At $z > 3$, K-band imaging with high angular resolution is critical in order to investigate the morphology of stellar components of galaxies. This wavelength range is not accessible with the current NIR camera on the *HST*, and this will be a very unique science with the ground-based telescopes (at least until the *JWST* era). Combining the K-band and [OIII] images with

~ 1 kpc scale resolution, we will investigate the sizes of star-forming regions with respect to stellar components (a compactness of a star-forming region), and also make a map of the EW, which is well corresponding to sSFRs, within a galaxy. Through such observations, we can understand how the star-forming activity is proceeded and stellar components are built up within individual galaxies.

Kinematics of ionized gas of $z > 3$ galaxies

We also plan to carry out observations with the integral field spectroscopy, such as SINFONI and KMOS on the VLT, for the [OIII] emitters in order to explore their kinematics. The kinematics of galaxies give us important information about the physical processes occurring within galaxies. When galaxies experience violent processes, such as major mergers, their ionized gas kinematics would be strongly disturbed. We can discriminate between the galaxies which evolve secularly and those in major mergers. By investigating the relation between the star-forming activity and gas kinematics, we will be able to understand what physical processes are involved in their vigorous star-forming activities.

Molecular gas components and dusty star-forming regions of $z > 3$ galaxies

Through a gas inflow or major merger, the molecular gas falls into the central part of a galaxy, and then the active star formation is induced in the central compact region. Due to the accompanied formation of dust at the center and its compact geometry, the strong dust extinction in the optical spectra or strong dust emission in the FIR would be observed at the central part of the galaxy. Therefore the resolved molecular gas components and dust emission within individual galaxies will enable us to investigate the presence of dissipative processes in galaxies.

With ALMA, we can obtain the high angular resolution images (~ 0.1 arcsec or even higher) of the molecular gas (traced by CO emission) and dust emission within individual galaxies even at $z > 3$. By combining the data taken with the IFU observations, we will be able to distinguish the two processes, namely, gas inflow and major mergers, inducing active and dusty star formation in the central regions of galaxies.

In addition to the resolved CO maps, it is also important to obtain information about global molecular gas components by observing galaxies with lower angular resolutions. This enables us to observe a diffuse molecular gas within a galaxy, i.e. its total molecular

gas mass. By combining with spectroscopic data shown in Chapter 5, we will be able to constrain the inflow/outflow rates of the [OIII] emitters (e.g. Seko et al., 2016).

Star-forming galaxies in high density environments before the peak epoch

In this *Thesis*, we only study the [OIII] emitters in the general fields, namely the SXDF and COSMOS. The surrounding environments play an important role on galaxy formation and evolution, as indicated from the galaxy segregation observed in the local Universe (e.g. Dressler 1980). We aim to investigate [OIII] emitters in high density environments, such as proto-clusters, at $z > 3$. However, the number of proto-clusters identified at $z > 3$ is still small, and we need to search for those proto-clusters at $z > 3$ in the first place. So far, we have performed a NB-imaging observation in a proto-cluster field at $z = 3.1$, MRC0316-375 (Venemans et al., 2007). We plan to carry out a systematic proto-cluster search with Subaru/MOIRCS and its NB filters by using radio galaxies at $z \sim 3 - 3.6$ as a probe of high density regions (e.g. Venemans et al. 2007; Maschietto et al. 2008) and by targeting proto-cluster candidates that will be found by the proto-cluster search with the Hyper Suprime-Cam (HSC)/SSP data.

Also, by performing the high resolution observations described above for [OIII] emitters both in the fields and proto-clusters, we can investigate the environmental impacts on the internal structures and kinematics of star-forming galaxies before the peak epoch.

With future instruments

The Simultaneous-color Wide-field Infrared Multi-object Spectrograph (SWIMS; e.g. Motohara et al. 2016) will be mounted on the Tokyo Atacama Observatory (TAO; Yoshii et al. 2010) 6.5m telescope in Chile in 2019. SWIMS has a unique set of NB filters in the NIR and wide field-of-view of ϕ 9.6 arcmin. We plan to carry out the NB imaging survey with SWIMS, and to construct a larger sample of [OIII] emitters at $z \sim 3$–3.6.

Moreover, Subaru has a future plan to build the next generation NIR facility/instrument called ULTIMATE-Subaru (Ultra-wide Laser Tomographic Imager and MOS with AO for Transcendent Exploration). ULTIMATE is the ground-layer AO (GLAO) system, which aims to achieve ~ 0.2 arcsec angular resolution across 15 arcmin field-of-view. With ULTIMATE, we will be able to extend the observations that we plan to do with IRCS+AO188 more systematically and to construct a much larger sample of [OIII] emitters at $z \sim 3$–3.6,

which are resolved down to ~ 0.2 arcsec.

In summary, we plan to construct a large systematic sample of the [OIII] emitters at $z = 3$–3.6 across various environments, and to investigate the internal structures of individual galaxies based on the AO-assisted imaging and IFU observations, as well as high resolution ALMA observations. We note that the NB-selected galaxies can be excellent targets for such follow-up observations, because we know their line fluxes and redshifts accurately, and the success rate of the observations can be maximized unlike other galaxy samples such as photometric redshifts selected galaxies and dropout technique selected galaxies. Through these observations, we will eventually reveal the physical processes involved in the environmental variations and the accelerated growth of star-forming galaxies since $z > 3$ towards the peak epoch.

References

Allen R. J., Kacprzak G. G., Glazebrook K., Tran K.-V. H., Spitler L. R., Straatman C. M. S., Cowley M., Nanayakkara T., 2016a, ApJ, 826, 60

Allen R. J. et al., 2016, ApJ, preprint(arXiv:1612.05262)

Andrew B. H., Martini P., 2013, ApJ, 765, 140

Atek H. et al., 2010, ApJ, 723, 104

Barden M., Häußler B., Peng C. Y., McIntosh D. H., Guo Y. 2012, MNRAS, 422, 449

Baldwin J. A., Phillips M. M., Terlevich R., 1981, PASP, 93, 5

Barro G. et al., 2013, ApJ, 765, 104

Barro G. et al., 2016, ApJL, 827, L32

Bertin E., Arnouts S., 1996, A&AS, 117, 393

Best P. et al., 2013, Astrophys. Space Sci. Proc., 37, 235

Brammer G., van Dokkum P. G., Coppi P., 2008, ApJ, 686, 1503

Brammer G. et al., 2012, ApJS, 200, 13

Brinchmann J., Charlot S., White S. D. M., Tremonti C., Kauffmann G., Heckman T., Brinkmann J., MNRAS, 351, 1151

Bruzual G., Charlot S., 2003, MNRAS, 344, 1000

Bunker A. J., Warren S. J., Hewett P. C., Clements D. L., 1995, MNRAS, 273, 513

Calzetti D., Armus L., Bohlin R. C., Kinney A. L., Koornneef J., Storchi-Bergmann T., 2000, ApJ, 533, 682

Casali M. et al., 2007, A&A, 467, 777

Cullen F., Cirasuolo M., McLure R. J., Dunlop J. S., Bowler R. A. A., MNRAS, 2014, 440, 2300

Curti M., Cresci G., Mannucci F., Marconi A., Maiolino R., Esposito S., 2016, MNRAS, in press (arXiv: 1610.06939)

Chabrier G., 2003, PASP, 115, 763

Civano F. et al., 2016, ApJ, 816, 62

Colbert J. W. et al., 2013, ApJ, 779, 34

Cowie L. L., Barger A. J., Hu E. M., 2011, ApJ, 738, 136

Daddi E. et al., 2005, ApJ, 626, 680

Daddi E. et al., 2007, ApJ, 670, 156

Damjanov I. et al., 2009, ApJ, 695, 101

Dekel A. et al., 2009, Nature, 457, 451

Dickey C. M. et al., 2016, ApJL, 828, L11

Donley J. L., Rieke G. H., Pérez-González P. G., Barro G., 2008, ApJ, 687, 111

Donley J. L. et al., 2012, ApJ, 748, 142

Dopita M. A., Kewley L. J., Sutherland R. S., Nicholls D. C., 2016, A&SS, 361, 61

Dressler A., 1980, ApJ, 236, 351

Elbaz D. et al., 2007, A&A, 468, 33

Erb D. K., Shapley A. E., Pettini M., Steidel C. C., Reddy N. A., Adelberger K. L., 2006a, ApJ, 644, 813

Erb D. K., Steidel C. C., Shapley A. E., Pettini M., Reddy N. A., Adelberger K. L., 2006b, ApJ, 647, 128

Fan X. et al. 2004, AJ, 128, 515

Föster Schreiber N. M. et al., 2009, ApJ, 706, 1364

Furusawa H. et al. 2008, ApJS, 176, 1

Galametz A. et al., 2013, ApJS, 206,10

Garn T., Best P. N., 2010, MNRAS, 409, 421

Geach J. E., Smail I., Best P. N., Kurk J., Casali M., Ivison R. J., Coppin K., 2008, MNRAS, 388, 1473

Genzel R. et al., 2008, ApJ, 687, 59

Genzel R. et al. 2014, ApJ, 796, 7

Grogin N. A. et al., 2011, ApJS, 197, 35

Hagen A. et al., 2015, ApJ, 817, 79

Hayashi M., Kodama T., Koyama Y., Tadaki K.-i., Tanaka I., 2011, MNRAS, 415, 2670

Hayashi M., Kodama T., Tadaki K.-i., Koyama Y., Tanaka I., 2012, ApJ, 757, 15

Heinis S. et al., 2013, MNRAS, 429, 1113

Holden B. P. et al. 2016, ApJ, 820, 73

Hopkins A. M., Beacom J. F., 2006, ApJ, 651, 142

Hopkins A. M. et al., 2003, ApJ, 599, 971

Ilbert O. et al., 2009, ApJ, 690, 1236

Izotov Y. I., Stasińska G., Meynet G., Guseva N. G., Thuan T. X., 2006. A&A, 448, 955

Jones T., Martin C., Cooper M. C., 2015, ApJ, 813, 126

Juneau S., Dickinson M., Alexander D. M., Salim S., 2011, ApJ, 736, 104

Juneau S. et al., 2014, ApJ, 788, 88

Kashino D. et al., 2013, ApJL, 777, L8

Kashino D. et al., 2016, ApJ, in press(arXiv:1604.06802)

Kennicutt R. C. Jr., 1998a, ApJ, 498, 541

Kennicutt R. C. Jr., 1998b, ARA&A, 36, 189

Kennicutt R. C., Evans N. J., 2012, ARA&A, 50, 531

Kereš D., Katz N., Weinberg D. H., Davé R., 2005, MNRAS, 363, 2

Kereš D., Katz N., Fardal M., Davé R., Weinberg D. H., 2009, MNRAS, 365, 160

Kewley L. J., Dopita M. A., 2002, ApJS, 142, 35

Kewley L. J., Ellison S. L., 2008, ApJ, 681, 1183

Kewley L. J., Dopita M. A., Leitherer C., Davé R., Yuan, T.-T., Allen M., Groves B., Sutherland R., 2013, ApJ, 774, 100

Kewley L. J., Zahid H. J., Geller M. J., Dopita M. A., Hwang H. S., Fabricant D., 2015, ApJ, 812, L20

Khostovan A. A., Sobral D., Mobasher B., Best P. N., Smail I., Stott J. P., Hemmati S., Nayyeri S., 2015. MNRAS, 452, 3948

Khostovan A. A., Sobral D., Mobasher B., Smail I., Darvish B., Nayyeri H., Hemmati S., Stott J. P., 2016, MNRAS, 463, 2363

Kojima T., Ouchi M., Nakajima K., Shibuya T., Harikane Y., Ono Y., ApJ, in press(arXiv:1605.03436)

Kobulnicky H. A., Kewley L. J., 2004, ApJ, 617, 240

Koekemoer A. M. et al., 2011, ApJS, 197, 36

Kodama T., Arimoto N., Barger A. J., Aragón-Salamanca A., 1998, A&A, 334, 99

Kodama T., Bell E. F., Bower R. G., 1999, MNRAS, 302, 152

Kodama T., Hayashi M., Koyama Y., Tadaki K.-i., Tanaka I., Shimakawa R., 2013, in Thomas D., Pasquali A., Ferreras I. eds., Proc. IAU Symp. 295, The Intriguing Life of Massive Galaxies, Cambridge Univ. Press), Cambridge, p.74

Koyama Y. et al., 2013, MNRAS, 434, 423

Kriek M., van Dokkum P. G., Franx M., Illingworth G. D., Magee D. K., 2009a, ApJL, 705, L71

Kriek M., van Dokkum P. G., Labbé I., Franx M., Illingworth G. D., Marchesini D., Quadri R. F., 2009b, ApJ, 700, 221

Kriek M. et al., 2015, ApJS, 218, 15

Kriss G., 1994, in Crabtree D. R., Hanisch R. J., Barnes J., eds, ASP Conf. Ser., Vol61, Astronomical Data Analysis Software and Systems III. Astron. Soc. Pac., San Fracisco, p.437

Lacy M., Petric A. O., Sajina A., Canalizo G., Storrie-Lombardi L. J., Armus L., Fadda D., Marleau F. R., AJ, 133, 186

Laigle C. et al., 2016, ApJS, 224, 24

Lawrence A. et al., 2007, MNRAS, 379, 1599

Leitherer C. et al., 1999, ApJS, 123, 3

Liske J. et al., 2015, MNRAS, 452, 2087

Madau P., Dickinson M., 2014, ARA&A, 52, 415

Madau P., Pozzetti L., Dickinson M., 1998, ApJ, 498, 106

Maiolino R. et al., 2008, A&A, 488, 463

Malkan M. A., Teplitz H., McLean I. S., 1996, ApJ, 468, L9

Mannucci F., Cresci G., Maiolino R., Marconi A., Gnerucci A., 2010, MNRAS, 408, 2115

Mannucci F., Salvaterra R., Campisi M. A., 2011, MNRAS, 414, 1263

Maschietto F. et al., 2008, MNRAS, 389, 1223

Masters D. et al., 2014, ApJ, 785, 15

McLean I. S. et al., 2012, in McLean I. S., Ramsay S. K., Takami H., eds, Proc. SPIE Conf. Ser. Vol. 7735, Ground-based and Airborne Instrumentation of Astoronomy III. SPIE, Bellingham, 77351E

McLean I. S. et al., 2012, in McLean I. S., Ramsay S. K., Takami H., eds, Proc. SPIE Conf. Ser. Vol. 8446, Ground-based and Airborne Instrumentation of Astoronomy IV. SPIE, Bellingham, 84460J

Mehta V. et al., 2015, ApJ, 811, 141

Meurer G. R., Heckman T. M., Calzetti D., 1999, ApJ, 521, 64

Miyazaki S. et al., 2002, PASJ, 54, 833

Moorwood A. F. M., van der Werf P. P., Cuby J. G., Oliva E., 2000, A&A, 362, 9

Mosleh M. et al., 2012, ApJL, 756, L12

Motohara K. et al., 2016, Proc. SPIE, 9908, 99083U

Moustakas J., Kennicutt R. C. Jr., Terminate C. A., 2006, ApJ, 642, 775

Nakajima K., Ouchi M., 2014, MNRAS, 442, 900

Nakajima K., Ellis R. S., Iwata I., Inoue A. K., Kusakabe H., Ouchi M., Robertson B. E., 2016, ApJL, preprint (arXiv:1608.08222)

Nakamura O., Fukugita M., Brinkmann J., Schneider D. P., 2004, AJ, 127, 2511

Noeske K. G. et al., 2007, ApJ, 660, L43

Oke J. B., Gunn J. E., 1983, ApJ, 266, 713

Onodera M. et al., 2016, ApJ, 822, 42

Osterbrock D. E., Ferland G. J., 2006, Astrophysics of Gaseous Nebulae and Active Galactic Nuclei. University Science Books, Mill Valley, CA

Oteo I., Sobral D., Ivison R. J., Smail I., Best P. N., Cepa J., Pérez-García A. M., 2015, MNRAS, 452, 2018

Peng C. Y. et al., 2010, AJ, 139, 2097

Pettini M., Pagel B. E. J., 2004, MNRAS, 348, L59

Pozzetti L. et al., 2007, A&A, 474, 443

Reddy N. A., Erb D. K., Pettini M., Steidel C. C., Shapley A. E., 2010, ApJ, 712, 1070

Reddy N. A., Pettini M., Steidel C. C., Shapley A. E., Erb D. K., Law D. R., 2012, ApJ, 754, 25

Reddy N. A. et al. 2015, ApJ, 806, 259

Rodighiero G. et al., 2011, ApJL, 739, L40

Salpeter E. E., 1955, ApJ, 121, 161

Sanders R. L. et al. 2015, ApJ, 799, 138

Sanders R. L. et al., 2016a, ApJ, 816, 23

Sanders R. L. et al., 2016b, ApJL, 825, L23

Schinnerer E., Groves B., Sargent M. T., Oesch P. A., Magnelli B., LeFevre O., 2016, ApJ, preprint (arXiv:1610.03656)

Scoville N. et al., 2007, ApJS, 172, 1

Seko A., Ohta K., Yabe K., Hatsukade B., Akiyama M., Yamura N., Iwamuro F., Dalton G., 2016, ApJ, 833, 53

Shapley A. E. et al., 2015, ApJ, 801, 88

Shen S., Mo H. J., White S. D. M., Blanton M. R., Kauffmann G., Voges W., Brinkmann J., Csabai I., 2003, MNRAS, 343, 978

Shibuya T., Ouchi M., Harikane Y., 2015, ApJ, 219, 15

Shimakawa R., Kodama T., Tadaki K.-i., Hayashi M., Koyama Y., Tanaka, I., 2015, MNRAS, 448, 666

Silverman J. D. et al., 2015, ApJS, 220, 12

Sobral D., Smail I., Best P. N., Geach J. E., Matsuda Y., Stott J. P., Cirasuolo M., Kurk J., 2013, MNRAS, 428, 1128

Sobral D., Best P. N., Smail I., Mobasher B., Stott, J., Nisbet D., 2014, MNRAS, 437, 3516

Sobral D. et al., 2015, MNRAS, 451, 2303

Sobral D., Kohn S. A., Best P. N., Smail I., Harrison C. M., Stott J., Calhau J., Matthee J., 2016, MNRAS, 457, 1739

Speagle J. S., Steinhardt C. L., Capak P. L., Silverman J. D., 2014, ApJS, 214, 15

Stark D. P., Schenker M. A., Ellis R., Robertson B., McLure R., Dunlop J., 2013, ApJ, 763, 129

Steidel C. C., Hamilton D., 1997, AJ, 105, 2017

Steidel C. C. et al., 2014, ApJ, 795, 165

Steidel C. C., Strom A. L., Pettini M., Rudie G. C., Reddy N. A., Trainor R. F., 2016, ApJ, 826, 159

Stern D. et al., 2005, ApJ, 631, 163

Storey P. J., Zeippen C. J., 2000, MNRAS, 312, 813

Straatman C. M. S. et al., 2016, ApJ, 830, 51

Strom A. L., Steidel C. C., Rudie G. C., Trainor R. F., Pettini M., Reddy N. A., ApJ, preprint(arXiv: 1608.02587)

Sutherland R. S., Dopita M. A., 1997, ApJS, 88, 253

Suzuki R. et al. 2008, PASJ, 60, 1347

Suzuki T. L. et al., 2015, ApJ, 806, 208

Suzuki T. L. et al., 2016, MNRAS, 462, 181

Tacconi L. J. et al., 2010, Nature, 463, 781

Tacconi L. J. et al., 2013, ApJ, 768, 74

Tadaki K.-i., Kodama T., Tanaka I., Hayashi M., Koyama Y., Shimakawa R., 2013, ApJ, 778, 114

Tadaki K.-i., Kodama T., Tanaka I., Hayashi M., Koyama Y., Shimakawa R., 2014, ApJ, 780, 77

Tadaki K.-i. et al., 2016, ApJ, preprint (arXiv:1608.05412)

Tanaka I. et al., 2011, PASJ, 63, 415

Tasca L. A. M. et al., 2015, A&A, 581, 54

Tomczak A. R. et al., 2016, ApJ, 817, 118

Tremonti C. A. et al., 2004, ApJ, 613, 898

Troncoso P. et al., 2014, A&A, 563, 58

Ueda Y. et al., 2008, ApJS, 179, 124

van der Wel A. et al., 2012, ApJS, 203, 24

van der Wel A. et al., 2014, ApJ, 788, 28

van Dokkum P. G. et al., 2008, ApJL, 677, L5

van Dokkum P. G. et al., 2010, ApJ, 709, 1018

Venemans B. P. et al., 2007, A&A, 461, 823

Whitaker K. E. et al., 2011, ApJ, 735, 86

Whitaker K. E., van Dokkum P. G., Brammer G., Franx M. 2012, ApJL, 754, L29

Williams R. J., Quadri R. F., Franx M., van Dokkum P., Labbé I., 2009, ApJ, 691, 1879

Wuyts E. et al., 2014, ApJL, 789, L40

Wuyts S. et al., 2007, ApJ, 655, 51

Wuyts S. et al., 2011, ApJ, 738, 106

Yoshii Y. et al., 2010, Proc. SPIE, 7733, 773308

Zahid H. J. et al., 2014, ApJ, 792, 75

Zakamska N. L., Strauss M. A., Heckman, T. M., Ivezić Z., Krolik J. H., AJ, 2004, 128, 1002